Development of a Monte Carlo simulation method for the evaluation of dose distribution calculations of radiotherapy treatment planning systems

BY

FREDERIK CARL PHILIPPUS DU PLESSIS

Thesis submitted to comply with the requirements for the M.Med.Sc degree in the Faculty of Health Sciences, Medical Physics Department, at the University of the Orange Free State

November 1999

Promotor : Dr. CA Willemse

Co-promotor : Prof. Dr. M.G. Lötter

Table of contents

CHAPTER 1

Introduction

1.1 Cancer treatment modalities

In a radiation oncology department patients are treated for cancer. A typical sequence of events after a patient first becomes aware of the symptoms of disease could be as follows: The patient first consults a physician who will refer the patient for specialized investigations to confirm a diagnosis. When cancer is suspected the patient is referred to a radiation oncologist. A radiation oncologist specializes in the diagnosis and treatment of cancer. The patient is then examined for possible malignancies. If a malignant tumor is suspected biopsies will be performed to obtain tissue samples. These tissue samples are analyzed by a pathologist to detect the presence of cancer and to identify the type of cancer. If the biopsy confirms that the patient has a tumor, its location and extent must be determined precisely. This is done with the aid of various devices such as CT scanners, scintillation cameras and radiation teletherapy simulators. This process is called tumor staging. Depending on the outcome of the staging process, a treatment protocol, which is a standard set of treatment procedures, is then selected.

The treatment of the patient can be a combination of surgery, radiation therapy and chemotherapy. Radiation therapy can be performed with teletherapy or brachytherapy and in some radiation treatment protocols both these techniques are used. In the case of brachytherapy the source of radiation is applied inside or in close proximity to the tumor volume. It may consist of radiation sources fed through a catheter or applicator. Examples of radionuclides used for radiation sources are cesium-137 and iridium-192 sources used in low dose rate and high dose rate afterloading devices. Older techniques include the use of radium sources and gold seeds.

Teletherapy is performed with radiation machines such as linear accelerators, Co-60 machines and orthovoltage machines. Here the treatment radiation is given via a configuration of external beams. These beams can consist of photons (x-rays), electrons, protons or neutrons. Protons are usually accelerated in large cyclotrons and, if a suitable target is chosen (lithium), neutrons can be produced by the protons striking the target and being absorbed by the atomic nuclei. These neutrons can then be used for radiation treatment. The type of particle beam to be used will depend strongly on the type and location of the tumor since each type of beam has its own characteristic tissue penetrating properties. A beam's penetrating power is governed primarily by its energy and linear energy transfer (LET) properties that also depends on the configuration of different tissue types in the path of the beam. In this study the focal point will be teletherapy performed with x-rays of nominal energy 8 MV, produced through the physical process of brehmstrahlung by 8 MeV electrons striking a thin tungsten target.

The important aspect is that all these types of radiation treatments must be planned carefully. The use of any form of ionizing radiation will lead to radiation of the tumor volume as well as the surrounding healthy tissue. Radiation of matter with particle beams, such as high energy X-rays is accompanied by interactions with the atoms. These interactions will cause energy deposition that can cause ionizations of the atoms of the material. Thus when tissues are subjected to ionizing radiation the ionized atoms inside the cells are chemically very reactive and are known as free radicals. They can alter the chemical composition of the cell which then causes the cell to terminate, being unable to divide and create new cells, or the cell can mutate (Yarnold, 1997). Some of these mutations can be dangerous in a sense that they can induce cancer. Thus radiation has a dual role in patient treatment: it can kill malignant cells, but it can also induce malignancy in normal cells. The absorbed dose is a physical quantity that is used to describe the amount of energy the radiation is imparting per unit mass of tissue when travelling through it. The effects of radiation on tissues can be related to the absorbed dose. It is usually prescribed in a treatment so that the dose would be tolerable for healthy tissue to avoid complications and lethal for malignant tissue/tumors (Upton, 1987). The SI unit for radiation dose is the Gray (Gy) and is measured in Joules per kilogram.

1.2 Treatment planning

The risk factors involved in radiation treatment make it necessary to perform accurate and careful treatment planning. Treatment planning is performed with a computer. For the treatment of tumors with afterloading devices and high-energy teletherapy machines treatment planning computers are used to calculate the optimal dose distribution using specialized software in a patient model. Most modern treatment planning systems have algorithms that can model the patient by using digital images obtained from a CT scanner. The patient model is usually constructed from a series of transverse CT slices with a slice thickness 1 cm. Each slice contains data related to the cross sectional tissue distribution in the patient. Each volume element in the CT slice contains a CT number or Hounsfield number that is related to the relative attenuation (total photon absorption) coefficient of the tissue type contained in the volume element to that of water at the effective energy of the scanner x-ray beam. With enough CT slices an accurate map of a patient's internal geometry can be reconstructed. The CT slices which contain the tumor volume are used by the treatment planning system to calculate dose distributions in its patient model when one or more beams of X-rays are directed on the tumor. CT scanners have improved the way the patient data is used for treatment planning purposes by enhancing the accuracy by which treatment planning computers can take the internal anatomical heterogeneities (different tissue types) into account (Sontag et al, 1977 and Mackie et al, 1977). The main objective of the treatment planning phase is to find an arrangement of radiation beams that will give a uniform dose to the target volume (which will include the tumor and some surrounding tissue in the patient) and which will minimize the radiation dose and complications to the surrounding healthy tissue (Dahlin et al, 1983, Brahme and Ågren, 1987, Sherouse, 1993 and Bedford et al, 1997). The target volume is established by the radiation oncologist.

With the patient model (CT slice data) and the treatment volume known, the radiation treatment can be planned. This is usually done by selecting various x-ray beams of suitable field sizes to envelop the treatment volume. These beams are directed so as to converge on the treatment volume in the patient model. The individual x-ray beam dose

distributions can be altered by using beam modifiers such as wedges, blocks and compensators. These devices alter the dose gradients or beam areas in order to fit the dose distribution to the geometrical shape of the treatment volume. The dose of each beam accumulates on the treatment volume and the healthy surrounding tissue receives less dose. It has the effect of sparing the healthy tissue due to radiation damage and minimizes the risk of complications.

After the dose distribution has been calculated, the radiation oncologist prescribes the total dose to be delivered to the treatment volume and the number of treatments the patient should receive (fractionation). (This is usually determined with the aid of a radiation biologist who knows how the specific tumor will respond to radiation dosage and fractionation). All this information is recorded on a radiation treatment plan that consists of a 2-D drawing of the patient outline and the dose distribution from all relevant radiation fields. It contains information of all beams such as field size, the use of wedges, gantry angles, collimator angles, source skin distances and prescribed monitor units. At this point a medical physicist is responsible for doing a final review of the plan. This includes verifying parameters like field sizes, wedges, the prescribed dose for each beam etc. The patient can then start treatment on the relevant accelerator.

1.3 Uncertainties in patient treatments

There are several factors which influence the dose delivered to the treatment volume. The patient can be set up with a certain error in the position on the couch of the accelerator. The patient can move during the radiation treatment. These factors are due to handling errors and can be minimized with careful set up techniques.

Other factors, which contribute to error in dose delivered, are of a more abstract nature. The CT scanner slice information of anatomical structures in the patient may not correspond to the true anatomical structure in the patient because of artifacts. They can be minimized through proper quality control and regular service of the CT scanner. The reconstruction algorithms of the CT scanner may not be accurate enough with the result

that it reconstructs CT images with an inherent inaccuracy, which can only be improved by developing more accurate software. In general, the CT scanners used at present can reconstruct patient cross section images with an accuracy suitable for clinical use and radiation treatment planning.

Other external factors which influence the dose delivered to the treatment volume include inexact field placement on the accelerator. This means that the radiation beam is not entering the patient at the correct location, resulting in a shift in the dose volume, which will not necessary correspond to the intended treatment volume. The accelerator is calibrated routinely by a medical physicist to make sure that the dose output is accurate enough. There is, however an uncertainty associated with the calibration, which is added to the errors, made during treatment. The beam can in some treatment cases be modified with compensators or lead alloy shielding blocks to obtain a specific beam shape. These factors are all contributing to the overall dose uncertainty but are not influenced by the accuracy of the treatment planning system (Goitein, 1985). Most of these errors on the accelerator can be minimized through a thorough and routinely exercised quality control program that includes aspects like x-ray and light field coincidence verification, distance meter and isocenter verifications, regular preventive maintenance, beam energy verification and regular beam flatness checks accompanied by at least an annual water bath measurement check for different field sizes regarding depth dose and beam profiles.

Nowadays some medical accelerators make use of multileaf collimators to obtain a specific X-ray beam shape. This is known as conformal therapy, which has an advantage over conventional open field methods of radiation in a sense that better tumor control can be obtained since only the target volume is radiated with minimal healthy surrounding tissue receiving a high radiation dose. These radiation techniques are also accurate provided that beam placement and patient fixation are adequate (Convery and Rosenbloom, 1995)

1.4 Inhomogeneity corrections

In addition to all these factors known to influence the accuracy of dose delivery, there is also the treatment planning system to take into account. Studies by Brahme, 1984 showed that an overall dose accuracy of at least 5percent must be attained for effective tumor control. The treatment planning system (TPS) calculates the dose distribution in patients with fast algorithms so that daily routine treatment planning can be feasible. This generally influences the accuracy of the calculated dose distributions in patients (Mackie et al, 1988).

The dose distributions are modeled by taking the various tissue types in a patient model into account. The reason is that tissues of different electron density influence the dose distribution of a beam of ionizing radiation differently. The treatment planning system uses algorithms that take these different tissue types into account when calculating dose distributions. This is known as inhomogeneity corrections.

Many different types of inhomogeneity correction methods have been developed over the years. Some include linear attenuation corrections, ratio of tissue-air-ratios (Cunningham, 1972) and effective SSD (Sontag and Cunningham, 1978). The correction methods employed in the treatment planning system in this study are the equivalent tissue-air-ratio (ETAR) and the generalized Batho power law methods (CADPLAN, 1995). These correction methods were improved a step further in 1978 by introducing a technique known as volume integration of scatter-air ratios (Larson and Prasad, 1978). Today various pencil beam algorithms and point spread functions have been developed for inhomogeneity correction applications (Ahnesjö et al, 1987, Mackie et al, 1988). These correction methods are constantly being refined to achieve greater accuracy in dose (Wong et al, 1996).

Despite ongoing research, even these methods are not accurate enough in all applications. Knöös et al, 1995 showed that as much as an 18 percent inaccuracy in dose can be obtained by pencil beam models in inhomogeneous tissue such as the lung.

Treatment planning computers make use of simplified algorithms to speed up dose distribution calculations. These algorithms lack stringent testing conditions and are generally tested in a simple geometry (Mah and Van Dyk, 1991 and El_Khatib et al, 1984). These relatively simple conditions however will not be enough to describe the influence of various different tissue types with complicated geometric configurations as is typically found in the head of a patient. This is mainly due to the fact that such complicated configurations of different tissue types make a prediction of the dose at a certain point very uncertain and difficult when employing these correction methods.

Uniform and precise dose delivery is one of the corner stones of effective radiation therapy of patients and a treatment planning system should be able to calculate the dose to an accuracy of at least 2 - 3 per cent to achieve proper tumor control (Brahme, 1984 and Ahnesjö et al, 1987).

With the development of Monte Carlo (MC) based simulations it became possible to evaluate these algorithms since it can be regarded as the most accurate method to obtain dosimetric data in any kind of medium including patient like geometries (Neuenschwander et al, 1995 and Seuntjens et al, 1994). It thus provides a benchmark for evaluating treatment planning systems. The main advantage of MC simulation calculations of dose distributions is that it can correctly calculate perturbative effects at interfaces between tissue types which differ considerably in atomic composition and physical density (Hannallah et al, 1996 and Sauer, 1995). This disrupts electronic equilibrium at the interface to such an extend that inhomogeneity correction algorithms would fail since they are all derived from the assumption that electronic equilibrium conditions hold (Mah and Van Dyk, 1991 and Sauer, 1995)

1.5 Monte Carlo simulations

In the 1970's a Monte Carlo simulation package called EGS4 (Electron Gamma Shower algorithm version 4) was developed at the Stanford Linear Accelerator Center (SLAC),

(Nelson et al, 1985). This code was able to simulate the transport of charged particles such as electrons, positrons and muons as well as photons through any kind of material. Monte Carlo simulations of ionizing radiation such as coupled photon-electron transport through matter can be done because the interactions of these radiation types are stochastic by nature. There is a statistical chance that a radiation particle with a certain energy can undergo a certain type of interaction at a certain location in a material. The probability that a certain type of interaction will occur is determined by its interaction cross section. These interaction cross sections are calculated in a separate program prior to any simulation. The EGS4 codes use a program called PEGS4 to do these calculations. This program requires the atomic composition and weight fractions of each atomic constituent of a material to calculate this interaction cross section data. These parameters are sampled from cumulative functions during a simulation.

For a typical case where a photon with known energy is transported through matter the simulation will proceed in the following steps: 1) The path length of the photon in the material will be sampled from a cumulative function that is a function of the material's total cross section. This is done by selecting a random number on the closed interval [0,1] and obtaining the path length from an inverse function. 2) At this point it is determined which interaction the photon might undergo. A second random number over the same interval is chosen and from an inverse cumulative function the interaction type is determined. The type of interaction will determine the amount of energy the photon has lost. The scatter direction of the photon is determined and a new point of interaction is sampled. The process is repeated until the photon has either left the material or it's energy has fallen below a predetermined threshold on which occasion its transport simulation is terminated. These procedures are collectively known as the photon's history.

Monte Carlo transport simulations are based on basic physical principles in which the fundamental interaction processes of the particles, including photons, are used (Nelson et al, 1985). The EGS4 Monte Carlo code simulates the transport process by taking one particle at a time. This leads to the unavoidable situation that several million particles

have to be transported in order to improve the accuracy or statistics of the simulation (Knoös et al, 1995). This technique of obtaining dose distributions in the material through which particle transport is taking place is currently the most accurate method to obtain dosimetry data. Many authors consider it as a golden standard and benchmark for dose distributions calculated for treatment planning systems and other dosimetric applications (Neuenschwander et al, 1995). Despite the superior capability of this program it cannot be used to calculate dose distributions in patients on a daily basis as conventional treatment planning computers can. This is mainly because the simulation time required is orders of magnitude larger than that available for treatment planning systems to calculate dose distributions since many histories have to be followed. The accuracy of MC dose distributions improves only as the square root of the total number of histories used in the simulation process. If the statistical error is to be reduced to half its present value, the number of histories used must be increased four fold. It is therefore evident that the Monte Carlo process is a slowly converging one.

This large number of histories also puts a demand on the random numbers used in the simulations. The EGS4 code makes use of pseudo random numbers that are random number strings of finite length, which contain up to 10^{18} different numbers. The main objective is that during a simulation the string will not be exhausted, because that could result in a repetition of histories, which will give, biased results.

A disadvantage of this EGS4 code is that it is very laborious to write a main program to simulate particle transport through complex geometries such as accelerators. This usually requires the mastering of a FORTRAN 77 based language called MORTRAN. In order to use the EGS4 code the user must write his own main program in which the geometry and dose scoring zones are modeled by including the subroutine programs HOWFAR and AUSGAB. This programming style could become very complex but is useful in the modeling of simple models such as water baths etc. In recent years various derivative EGS4 based codes have been developed in order to make EGS4 programming more user friendly. In the past a prospective user had to learn a great deal of programming in order to do even simple EGS4-based Monte Carlo simulations. The development of derivative

codes such as the EGS4 (Nelson et al, 1985) based BEAM (Rogers et al, 1995) and DOSXYZ (Ma et al, 1995) codes made it possible to do complex simulations with only a limited knowledge focussed on various input parameters to be able to use these codes.

1.6 The BEAM code

This code was developed at the National Research Council of Canada (NRCC) with the primary objective to simulate radiation therapy treatment machines such as medical accelerators, cobalt units and orthovoltage machines. When constructing a therapy machine the program makes use of component modules which are standard 'building blocks' which the user selects. Each of these component modules can represent a certain part of the machine. Let's say a simple accelerator is to be constructed with the BEAM code. The accelerator is made up of a target and a primary collimator with a flattening filter. The user will build an accelerator which consists of three component modules each representing the parts of the accelerator. The accelerator will then be compiled and an input file must be configured before any Monte Carlo simulation can be done. This input file will contain parameters, which are used to define the various component modules' physical dimensions and materials. Photon and electron cut-off energies can also be specified which can be used as a variance reduction technique to eliminate unnecessary particle transport through thick materials such as jaws. It is also stated where the emerging particles will be scored in a phase space file (PSF). This file contains the information of all particles crossing a certain plane perpendicular to the accelerator's emerging beam direction (z direction). This information includes the direction cosines, position, charge and energy of all particles 'collected' in the phase space file. With enough of these particles collected it can give a complete description of the radiation beam at the chosen level in the generic radiation machine. This file can be used as a beam source and can therefore be used in other simulation applications. This simulation strategy can also allow users to simulate the transport of particles through an accelerator in stages. An accelerator can be modeled from the target down to the plane above the jaws where a phase space file can be scored. This file can be used as a source of particles which can be used to simulate these particle's transport through the jaws of the

accelerator in a second stage. In this study the BEAM code was used to simulate photon transport through a Philips SL75/14 based generic accelerator. Phase space files were scored directly below an ion chamber to act as a source for open and wedged x-ray beams with different jaw settings (field sizes) and at an SSD of 100 cm. Another advantage of these phase space files is that they can be used directly in another EGS4 based Monte Carlo simulation program DOSXYZ. This feature makes the code particularly powerful since no special beam modeling is required and the original source (beam) characteristics can be used directly in dose distribution simulations in more complex geometries with the DOSXYZ Monte Carlo code.

1.7 The DOSXYZ code

This is also an NRCC development of the EGS4 code with the aim of simulating particle transport through any desired medium of any inhomogeneous material distribution in a Cartesian co-ordinate system. The code was designed to contain an EGS4 main program with the subroutines HOWFAR and AUSGAB imbedded in it. The coordinate system is Cartesian and the user is allowed to determine the number, dimension, material and the density in each voxel. This type of program is suitable for obtaining dose distribution simulations of particle transport through a constructed water bath and even complex media such as patient models made up from CT-slice data. The user has to supply a suitable input file containing the patient model and describe the particle source which can include phase space files, etc. The field size and direction of the beam impinging on the medium must also be given.

1.8 Patient models

Any treatment planning system needs a patient model in order to calculate dose distributions. Some use CT slice data of the patient which include the tumor. The advantage of using CT data is that inhomogeneity corrections can be readily applied. A CT image of a patient is a map of linear attenuation coefficients (CT numbers) measured in Hounsfield units. These CT numbers are converted to relative electron densities from

an experimentally determined bilinear function. This converted data is used to perform inhomogeneity corrections. The treatment planning system under evaluation uses the Batho and the equivalent tissue-air-ratio (ETAR) methods that make use of each voxel's relative electron density in inhomogeneity corrections.

Monte Carlo programs such as DOSXYZ can in principal calculate dose distributions in a patient model. CT slice data cannot be used directly as a patient model since at each voxel only the CT number is known. The program must have information of what type of material/tissue is present in each voxel. The EGS4 based Monte Carlo codes use interaction cross section data during a particle's simulation. This cross section data is not readily obtainable from CT slice data. For the purposes of this study a method was developed to assign a certain tissue type to a range of CT numbers in a CT image. The tissue types were selected on a basis of dosimetric equivalence. The CT data was converted from a CT image to a tissue image. Each tissue in the image had its own known atomic composition (ICRU 44) and could be used to recalculate the relevant interaction cross section data. This enabled the use of CT data through a transformation technique in DOSXYZ (Du Plessis et al, 1998)

1.9 Aim of study

1.9.1 Introduction

Currently available Monte Carlo codes are able to very accurately calculate the dose in any medium due to a radiation beam. Using MC codes such as BEAM and DOSXYZ, it is possible to generate all the necessary input beam data needed by a modern 3D TPS to represent a generic accelerator, without the need for any measurements. Although such a generic accelerator will not represent any given accelerator exactly, it will approximate all the characteristics of a real accelerator very closely. After configuration of the beam data, the TPS will then be able to calculate dose distributions for beams of this generic accelerator in realistic patient models, based on CT scans of real patients.

By using the original PSF's, with which the above beam data were generated, as source input for the DOSXYZ code, and constructing 3-D phantoms from the same patient CT data used for the TPS patient models, DOSXYZ can be used to calculate the corresponding dose distributions very accurately. These dose distributions can then serve as benchmarks against which the TPS's calculations can be compared. This will yield an objective evaluation of the TPS's algorithms, eliminating any uncertainties inherent in the use of measured dose distributions.

1.9.2 Aim

The aim of this study was to:

1) Generate input beam data and configure a CADPLAN TPS for an 8 MV photon beam of a generic accelerator based on a Philips SL75/14 accelerator, using the BEAM and DOSXYZ MC codes.
2) Calculate 3-D dose distributions with the CADPLAN TPS in CT based patient models for a number of common treatment sites.
3) Evaluate the CADPLAN dose calculation algorithms by comparing the distributions in 2) with corresponding dose distributions calculated with the DOSXYZ code using the original PSF's as source input.

1.10 Summary

In a radiation oncology department cancer patients are treated using ionizing radiation. Tumor localization is frequently done with CT scanners. This patient information is used to construct a patient model and to simulate the radiation treatment of the cancer on a treatment planning computer. This computer makes use of fast algorithms which approximate the dose distribution in the patient model. These algorithms use various inhomogeneity correction methods such as the generalized Batho power law and the equivalent tissue-air-ratio method. All these algorithms lack the ability to model the electronic disequilibrium at the interface between tissue types which differ in electron density. This can lead to large inaccuracies in the dose distribution near these interfaces.

Monte Carlo programs such as BEAM and DOSXYZ can be used to obtain dosimetric data for a generic accelerator. This beam data can be used to calculate dose distributions in patients on a treatment planning system using CT data for its patient model. Dose distributions can also be calculated on a corresponding patient model with DOSXYZ. This allows a direct comparison of the Monte Carlo calculated dose distributions and dose distributions obtained on the treatment planning system (TPS), leading to an objective evaluation of the TPS algorithms.

CHAPTER 2

Photon and electron interactions and dosimetry

2.1 Introduction

Radiation dosimetry concerns itself with the determination of the energy absorbed in a medium from a known beam of ionizing radiation. The particles in the beam interact with the atoms in the material and this result in an energy loss of these particles. The interaction processes are well understood and depend on the type of particles (in this sense photons can be thought of as particles) and beam energy as well as the atomic composition of the medium. Radiation interactions are stochastic by nature meaning that it is impossible to calculate with a high degree of precision what type of interaction will occur and also where it will occur in the medium (Attix 1986, and Nelson et al, 1988). It is however possible to calculate the probability for a certain type of interaction to occur. This can be done through the use of interaction cross section data.

There are many types of particles but in this study attention is focussed on photons and electrons. It is important to know the types of interactions that photons and electrons can undergo in materials and how they are related to interaction cross sections. The latter form the basis for any Monte Carlo code. In this chapter the interactions of photons and electrons with matter will be discussed. This will then be followed by a discussion of dosimetry to give a clear outline of the concepts used in deterministic dose calculations.

2.2 Particle interactions

Particles such as photons interact with a medium; the probability to interact with the medium is characterized by interaction cross sections. If more than one interaction can

take place then the probability of the photon undergoing an interaction is the sum of the individual probabilities. In practice if an x-ray beam contained N photons and passed through a medium of thickness say x then the total number of photons that did not interact with the medium could be expressed as:

$$N(x) = N_O \exp(-\mu x) \qquad 2.1$$

where μ is referred to as the total linear attenuation coefficient of the material (Bjärngard and Shackford, 1994 and Hubbell and Seltzer, 1995)). This quantity is related to interaction cross sections which are expressed per electron or atom. The attenuation coefficient is thus the bulk interaction cross section of the total number of atoms or electrons per gram of material. Its units are m^{-1}. This quantity could also be made density independent to obtain the mass-attenuation coefficient with units m^2/kg. On the atomic level the interaction cross section is expressed in barns/atom with 1 barn = 10^{-24} cm^2.

2.2.1 Photons

The quantum of the electromagnetic field is the photon. Thus a beam of x-rays can be completely described as a set of photons each having its own energy, direction and position in the beam. These photons can interact with matter. Some interactions are with the atomic electrons and others more directly with the nucleus. Photons can undergo six types of interactions in matter depending on their energy (Hubbell and Seltzer, 1995). At low energies the most predominant of these interactions are coherent or Raleigh scattering and photoelectric absorption. At energies of about 100 keV these interactions decline and the incoherent or Compton scatter events start to become dominant up to about 1 MeV. At and above this energy the pair production interaction becomes more dominant. At about 5 MeV the triplet production interaction is energetically possible followed by the photonuclear reaction at about 10 MeV. This energy dependence of the interaction types is material dependant and the above example will be observed for carbon. In this study the nominal x-ray beam energy at which the treatment planning

system's dose calculation algorithms will be evaluated is 8 MV with a mean energy of 1.5 MeV. For tissue material which is water-like the three most important interactions that will be discussed are Compton scattering, pair production and photoelectric absorption. The Compton interaction is the most dominant at these photon energies and accounts for about 97 to 98 percent of all interactions followed by about 2 to 3 percent for pair production to about 0.1 percent for the photoelectric interaction. In all these interaction types the probability for it to occur is called the interaction cross section. Thus if it is stated that 97 percent of the interactions are Compton events, it is the same as saying that the probability (P) is 97percent that an interaction event will be a Compton event. It can be calculated if the interaction cross section data is available for soft tissue types and at these photon energies (ICRU 44, 1989) by the simple formula:

$$P = \sigma_c/(\tau_{ph} + \sigma_c + \sigma_{pp}) \qquad 2.2$$

Where τ_{ph} and σ_{pp} are the atomic cross sections for the photoelectric and pair production events and σ_c is the atomic Compton cross section.

2.2.1.1 Photoelectric absorption

In the photoelectric interaction a photon interacts with an inner bound electron in an atom, usually in the K and L energy levels (Krane, 1988). All energy is transferred to the electron and if the original photon had enough energy the energized electron could overcome its binding energy and the remaining energy is liberated as kinetic energy. The probability for this interaction to occur is strongly dependent on the energy of the photon as well as the effective atomic number of the material (Johns and Cunningham, 1983). Storm and Israel have derived formulae for the calculation of photoelectric cross sections. Some authors use approximations for calculating photoelectric cross sections (Hubbell, 1980). The energy dependence of this interaction is complicated and as a crude rule it can be said that it obeys an inverse relationship with photon energy roughly as E^{-3} with strong interaction edges for photon energy values that match the binding energies of the electrons. This is quite apparent for high atomic number (Z) materials such as lead

(Johns and Cunninham, 1983). Its variation with atomic number is also given as a crude $Z^{3.8}$ dependence.

2.2.1.2 Incoherent or Compton scattering

During a Compton event a photon loses part of its energy to an outer bound or loosely bound atomic electron (Krane, 1988). The electron is liberated and scattered through a certain angle. Conservation of momentum dictates then that the photon must be scattered at a fixed angle for a given energy after colliding with the electron. This interaction probability is determined by the electron density of the material as well as the energy of the photon. Klein and Nishina have derived a formula for the calculation of the Compton interaction cross section per electron based on quantum mechanical reasoning (Hubbell, 1980, Johns and Cunningham, 1983 and Krane, 1988). If this cross section is multiplied by an incoherent atomic scatter function S(x,Z) the atomic Compton cross section is obtained (Johns and Cunningham, 1983 and Hubbell, 1980). The Compton interaction is almost independent of Z and decreases with increase in photon energy and is regarded as the most important interaction in soft tissue for the energy range 100 keV to 1 MeV (Johns and Cunningham, 1983).

2.2.1.3 Pair production

In a pair production event a photon interacts with the coulomb field of a nucleus creating an electron-positron pair. A heavy nucleus is required for momentum conservation purposes (Krane, 1988). After the event only these two particles exist. All the photon energy was converted into mass and kinetic energy. The energy threshold of 1.022 MeV must be attained for pair production to occur since each particle of the pair has the same rest mass energy of 0.511 MeV. Cross section data for these interactions have been derived by Bethe and others (Hubbell and Seltzer, 1995). A photon can also interact with the coulomb field of an atomic electron, liberating an electron-positron pair plus the bound electron to give a triplet of particles. The positron can be regarded as an electron that possesses a positive charge equal in magnitude to the electron charge with the same

mass and spin. The pair production interaction varies as Z^2 and increases rapidly with energy above 1.02 MeV when pair production becomes energetically viable (Johns and Cunningham, 1983).

The calculation of the photoelectric, Compton and pair production interaction cross sections are treated quantum mechanically and involves atomic form factors and incoherent scattering functions (Hubbell et al, 1980). It is beyond the scope of this study to investigate these calculations in detail.

2.2.2 Electrons

The three most important interactions of photons with water-like tissue in the few MeV energy range all have one common result. In all three interactions charged particles are emitted or created. Electrons are thus intimately coupled to photon transport. If photon transport is to be simulated then the transport of the liberated electrons should also be simulated. In order to do that it is necessary to evaluate electron interactions with matter. These interactions can be characterized as ionization and radiation interactions or events.

2.2.2.1 Ionization interactions

As electrons travel through matter they can undergo thousands of interactions in a unit path length. The ionization events are dominant in the lower electron energy range. Here the electron loses energy through collisions with other bound atomic electrons. These electrons can be liberated from their bound states. Interactions of this type involve electron – electron scattering and it could be differentiated further into Møller scatter, Bhabha scatter and annihilation. Møller scatter occurs when electrons collide with electrons, whereas a Bhabha scatter event is between an electron and a positron. Annihilation events occurs at low kinetic energies where an electron-positron pair is annihilated to create two oppositely propagating photons each with an energy of 0.511 MeV that is equal to the electron rest mass energy. Thus electrons in the lower energy range lose energy mainly through collisions (Attix, 1986, Nelson et al, 1985 and Krane,

1988). If the critical energy is defined as that energy at which the collisional and radiative stopping powers become equal. It has a value of 90 MeV in water and 10 MeV for lead. Thus in water the collisional energy losses dominates for most electron energies used in clinical practice up to 22 MeV.

2.2.2.2 Radiative interactions

Electrons with high enough energy lose energy through brehmstrahlung events. As an electron approaches a nucleus it experiences a strong coulomb force of attraction. The electron decelerates as it passes the nucleus, the loss of energy it experiences manifests itself in the production of a photon that carries off the kinetic energy that the electron has lost. In a sense the brehmstrahlung interaction is very similar to the pair production interaction. In the former case a photon is created and in the latter the photon is destroyed. Both occur in the coulomb force field of the nucleus (Attix, 1986).

2.2.2.3 Linear energy transfer, stopping power and range

The electron is a charged particle and therefore interacts via the coulomb force with electrons and nuclei in matter. If an electron with high enough energy travels through matter it will lose energy through brehmstrahlung events due to coulomb interactions with atomic nuclei. The electron experiences an energy loss at each brehmstrahlung event and it slows down. As it loses energy it experiences more collision type interactions with atomic electrons. The rate of energy loss depends roughly on the inverse of the electron velocity. Thus as it slows down its rate of energy loss increases sharply until it has lost all kinetic energy and it just diffuses through matter (Attix, 1986).

The two types of electron interactions are combined into a quantity very useful for radiation dosimetry purposes known as the stopping power (S). These stopping powers describe the amount of energy loss that an electron will experience as it travels a certain distance through matter. It is classified into radiative (S_{rad}) and collision (S_{coll}) stopping powers (Low and Hogstrom, 1994, Ding et al, 1995 and Maughan et al, 1999). In some

cases only the collision stopping power is of interest and the quantity is then known as the restricted stopping power (L). The stopping power is a function of the electron energy that is closely related to its average linear energy transfer (Li and Rogers, 1995). This quantity can be made density independent by taking the quotient of the stopping power and the material density to obtain the mass-stopping power (S/ρ).

As the electron experiences energy losses through collision and radiation events it slows down. As it slows down it can transfer more energy per unit path length. At the stage when its energy is very low it abruptly loses all of its energy within a fraction of a path length at the so called Bragg depth. This depth is the maximum depth that the electron can travel through matter. The range of the electron can be calculated from its rate of energy loss if its stopping power is expressed as a continuous function of its energy. This method of range calculation is known as the continuous slowing down approximation (CSDA) that ignores the erratic way the electron is losing energy and the fact that it is not traveling in a straight path.

2.2.3 Electron scatter

Another aspect of electron transport is that electrons also change direction at each interaction event (Papiez et al, 1994 and Jette and Walker, 1997). A quantity useful to describe this directional change is the so called mass-scattering power that can be defined as the increase in the mean square angle of scattering per unit mass thickness traversed (Attix 1986 and Li and Rogers, 1995).

2.3 Dosimetry

In this section a brief discussion of photon dosimetry will be given. As seen in section 2.2.1 photons liberate/create electrons in their interactions with matter. These electrons interact with matter according to section 2.2.2. It is these electrons that transfer energy to matter. If a small volume of interest is evaluated it is seen that some electrons impart energy to this volume element while other electrons are set in motion in this volume

element and impart their energy outside this volume (Attix, 1986). This phenomenon is utilized in the concept of electron equilibrium and is discussed by Nizin, 1993 and Hannalah et al, 1996. Various theories have been developed for dosimetry measurements on the basis of volume elements, which are surrounded by a different medium for the case where for example ion chambers are used. These are known as cavity theories (Attix, 1986; Ogunleye et al, 1980; Horowitz et al, 1983; Kearsley, 1984; Ogunleye, 1987; Haider, 1997). Some of these theories were evaluated by Miljanic et al, 1997 for Co-60 photon radiation using thermoluminescent dosimeters (TLD's).

Absorbed dose (D) due to particle interactions is defined (Attix, 1983 and Johns and Cunningham, 1983) as the total energy (dE) imparted to a volume element of mass (dm) and is defined by the equation:

$$D = dE/dm \qquad 2.3$$

Its unit is Jkg^{-1} referred to as the gray (Gy). Note that the imparted energy is of interest and not simply the energy transferred to the volume element. This is because although there is energy transference from radiation interactions in and around the volume element some of the energy is carried away from it or carried out of it.

It can be described as the net fraction of energy imparted from all energy transferred from a beam of photons to a mass (m). The transferred kinetic energy due to a beam of photons to the mass is also defined as the kerma (Attix, 1986 and Johns and Cunningham, 1983). It can be interpreted as the kinetic energy released to electrons as to set it in motion from their bound states. Here the kerma is further classified into a radiative and collision kerma (Attix, 1986). Kerma is a two stage process, the first involves an energy transfer during an interaction with a photon and an atomic electron and second the transfer of energy from the liberated high energy electron via excitation and ionization (Johns and Cunningham, 1983). The kerma is related to the mass energy-transfer coefficient and can be calculated from a known energy fluence (Ψ) as:

$$K = \Psi(\mu_{tr}/\rho) \qquad 2.4$$

where (μ_{tr}/ρ) is the mass energy-transfer coefficient that depends on the photon energy as well as the material which the photons are traversing.
The energy fluence (Ψ) can be defined as the total number of photons with a certain energy distribution crossing a unit area, that is the total energy crossing a unit area (Johns and Cunningham, 1983).

A useful quantity in photon dosimetry is the mass-energy absorption coefficient (Hubbell and Seltzer, 1995; Hubbell, 1982; Seltzer, 1993). This parameter is energy and material dependant. It is useful for calculating the dose in unknown media if the photon fluence is known as well as the dose in another medium, say water, irradiated with the same photon fluence. Under charged particle equilibrium conditions (CPE) the dose to the medium can be related to that of water through 2.5:

$$D_{med} = D_{water}(\mu_{en}/\rho)^{m}_{w} \qquad 2.5$$

Where $(\mu_{en}/\rho)^{m}_{w}$ is the ratio of the mass energy-absorption coefficients of the medium and water (Attix, 1986). The mass energy-absorption coefficient is the remainder of the mass energy-transfer coefficient after the energy lost to brehmstrahlung events has been subtracted, since this energy is carried out of the mass and does not contribute to the dose. It should be emphasized here that dosimetry theories and methods stretch far beyond the scope of this study.

2.4 Summary

Beams of particles such as photons and electrons interacts with matter in a stochastic manner. Photons undergo basically six interaction types of which the photoelectric, Compton and pair production events are the most important for high-energy radiation through tissue like substances. The interactions are expressed in terms of cross sections. Photon beams liberate/create secondary electrons that are primarily responsible for

energy transfer to matter. These electrons experience energy losses through ionization (collision) or brehmstrahlung (radiative) events. This can be explained through the concept of the collision and radiative kerma and the mass-energy transfer coefficient. The energy imparted to a mass can be calculated through the use of the mass energy absorption coefficient or collision kerma under CPE conditions (Attix, 1984).

CHAPTER 3

Monte Carlo Principles and the EGS4 code

3.1 Introduction

In the previous chapter the interactions of electrons and photons with matter were discussed. It was seen that interaction cross section data could be used to describe each photon and electron interaction type. These interaction cross sections can be interpreted as probabilities for these interactions to occur. Radiation interactions are stochastic by nature meaning that they can be modeled by means of a computer through random sampling. This is precisely what the Monte Carlo method does and it can thus be regarded as the method of choice for precise modeling of photon-electron showers.

When a high energy photon with energy say of a few MeV enters an arbitrary volume of semi-infinite dimensions then it will interact with the atoms in the medium. It will however travel a certain distance before interacting. The mean distance it travels before an interaction takes place is known as the mean free path. It depends on the photon energy and type of medium with regard to its physical density and atomic constituents. The type of interaction is governed by the relative magnitude of the cross section for each interaction. For example, let us argue that only two interactions could occur, say Compton and pair production events, and the total fraction of Compton events is say 90 percent. Then it is clear that 90 percent of the interactions must be Compton events. For each interaction type the resulting particles that can be photons and/or electrons must have a proper energy and direction. This would be determined by choosing a random direction for the photon. The resulting electron energy and scatter direction would then be calculated from the kinematics of the interaction. The electron loses energy by radiative

and collisional losses and the photon would travel another distance before another interaction type will take place. This is an example of how an electron-gamma shower evolves from one incident photon. It could also be produced by an incident electron with a kinetic energy of a few MeV. Here the photons would be produced by brehmstrahlung events in radiative energy losses. The whole electron-gamma shower resulting from a single primary particle is known as a history. If a Monte Carlo simulation is set for 1000 histories, this means that 1000 electron-gamma showers are completely simulated.

The modeling of such electron-gamma showers is essentially what Monte Carlo codes aim to do in simulating coupled photon-electron transport. Some of these codes were developed to calculate radiation shield thickness for gamma radiation in large accelerators like at Stanford (Nelson et al, 1985) while others made efforts to incorporate it into dosimetric calculations for medical physics applications (Berger and Spencer, 1959 and Webb, 1978). Others gave reviews on what the Monte Carlo method is and what the principles of it are (Reaside, 1976). Today there are several different Monte Carlo codes available. Some of them include EGS4 (Nelson et al, 1985), ITS3 (Halbleib and Melhorn), MCNP (Wallice et al, 1995; DeMarco et al, 1994 and 1998, Lewis et al, 1999), MCPAT, a derivative code of EGS4, (Wang and Sloboda, 1996) and codes for investigating scatter at diagnostic photon energies (Persliden, 1983; Chan and Doi, 1985 and Sandborg et al, 1994). For 3D electron dose calculations there is the VMC code (Kawrakow et al, 1996) and the SHAPE code (Manfredotti et al, 1990). Another code for radiation transport simulations is the PEREGRINE code developed at Lawrence Livermore laboratories (Hartmann-Siantar et al, 1995).

The EGS (EGS3 and the later version EGS4) codes have been used extensively in various medical physics applications like the study of Co-60 gamma ray beams (Attix et al, 1983; Higgins et al, 1985 and Rogers and Bielajew, 1985) and brachytherapy studies (Valicenti, 1995; Wang and Sloboda, 1996; Ballester et al, 1997; Cheung et al, 1997 and Pérez-Calatayud et al, 1999). It has also been used to study dosimetry and cavity theories (Mobit et al, 1997; Bielajew, 1985 and Rogers and Bielajew, 1985). The code can also calculate quantities like mass scatter and stopping powers as well as various other

accelerator characteristics such as head scatter, the calculations of dose point kernels, beta dose kernels and x-ray spectra of radiosurgical beams (Chaney et al, 1994; Ebert and Hoban, 1995; Sixel and Faddegon, 1995; Li and Rogers, 1995; Mohan and Chui, 1985; Udale-Smith, 1992; Ding et al, 1995; Mackie et al, 1988 and Simpkin and Mackie, 1990)

The EGS4 code has also been utilized in several derivative codes (Monte Carlo codes based on EGS4 transport simulations) for example DOSXYZ, DOSRZ and the BEAM code. DOSXYZ calculates 3D dose distributions in a Cartesian co-ordinate system while DOSRZ uses a cylindrical co-ordinate system. The BEAM code is very powerful and diverse for the simulation of radiotherapy treatment machines. The MNCP code has also been utilized to model a linear accelerator (Lewis et al, 1999) as well as the McRad code (Lovelock et al, 1995).

In this chapter the basic operation and requirements for Monte Carlo codes will be given with the emphasis on the EGS4 based codes.

3.2 The PEGS4 preprocessor code

Interaction cross section data is essential for the simulations of coupled photon and electron transport. For each interaction type cross section data must be available that depends on the material and the energy of the particles to be transported. The EGS4 code can simulate the following physical processes: brehmstrahlung x-ray production, pair annihilation, Moliere multiple (coulomb) scattering, Møller and Bhabha scattering, pair production, incoherent (Compton) and coherent (Thompson) scattering, photoelectric absorption, continuous energy loss of electrons and radiation and collisional interaction. The dynamic energy ranges from a few keV (1keV for photons) up to hundreds of GeV.

The PEGS4 preprocessor program calculates the relevant cross section data by reference to a suitable input file that contains among other variables the atomic composition, physical density, and energy range over which the data must be generated for photons and electrons. The state of the material can be gaseous, solid (mixtures or compositions)

or liquid. This input file is to be set up for each material through which transport simulations are to be carried out. The output data is stored over a number of intervals (60) over the energy range specified. Since cross section data can be calculated up to hundreds of GeV it is desirable to keep the energy range as small as possible, since this would improve the accuracy of interpolations between cross section values. An option can be given to interpolate between energy values via a piece wise linear fit (PWLF).

This procedure is carried out prior to the Monte Carlo simulation since this data has to be calculated first. This approach leads to shorter simulation times since cross section data can be obtained much faster than on line calculations would allow during a simulation. It is reduced to a simple look-up-and-interpolate procedure (Nelson et al, 1985). The EGS4 code has tables containing cross section data for the first 100 elements.

Various cross section data can be calculated depending on what type of simulation is carried out. For very high energy simulations fluorescence phenomena might not be of interest so it would not be specified in the input file for cross section calculations.

Other Monte Carlo codes such as the ITS3 code also use the principle of pre-generating cross section data before a simulation can be started.

3.3 Random numbers

The Monte Carlo technique involves random sampling from known particle interaction cross sections. This means that large arrays of independent random numbers must be supplied in order to carry out Monte Carlo simulations. Computers cannot generate infinite arrays of random numbers but can generate pseudo random numbers. This means that an array of random numbers is deterministically calculated and that after many iterations it would start to repeat itself. As long as the numbers are not used up in the array the numbers will be random (Raeside, 1976). The EGS4 code utilizes an algorithm of the form:

$$I_{n+1} = (aI_n + c) \bmod 2^k \qquad 3.1$$

where a is the multiplier and c is the increment.

The length of the string is determined by the constants a and c and can give up to $4*10^9$ numbers on a 32-bit computer where k = 32. The first random number is given by the user and is known as the random generator seed. This seed is an integer, between 1 and 100, and is entered by the user in the BEAM and DOSXYZ input files to run these codes. The rest of the numbers are calculated from the recurrence relation described by equation 3.1. The EGS4 code utilizes this method (the multiplicative congruential method) by setting c = 0 and a = 663608941. This method of random number generation is preferred over sampling from tables because it is faster and saves memory. This random number generator is used 'in-line' in the EGS4 code since it can calculate random numbers quite fast. Raeside, 1976, gave an account of the various tests that can be carried out to test the 'randomness' of a string of numbers that include the moments, frequency, serial, poker and gap tests. The random numbers that are generated are uniform over the unit interval.

The Monte Carlo simulations used in this study require millions of histories and this sequence of random numbers would unavoidably be used more than once. This is not considered a problem since the particle histories would have to be synchronized with the repetition of the random number string before histories can become identical. However, if this phenomenon did occur, it would be difficult to tell that it had occurred.

3.4 Random sampling

The EGS4 code utilizes the so called direct method of sampling. To give a crude illustration of what it is consider the following: Suppose we have two random variables x' and y'. Suppose these two variables are related through the function $y' = h(x')$ with h a monotonically increasing function. If x' and y' have distribution functions, say F and G, then it can be shown that $F(x) = G(h(x))$ (Nelson et al, 1985). Thus F can be found, provided that G and h are given. If x' is defined by the relation: $x' = F^{-1}(\varsigma)$, where ς is a

uniformly distributed random variable (generated random number) then G(y) = y and h(x) = F(x). This is the direct sampling method of sampling x' that involves setting F(x) = ς and solving for x.

For functions of several variables, as is typically found in cross section generating functions where the energy and the scatter direction of a particle are two variables that determine its interaction cross section, other methods of random sampling are employed. The EGS4 code uses a combination of the composition and rejection techniques (mixed method) (Nelson et al, 1985). In this case a function f is composed of two functions f_i and g_i such that:

$$f(x) = \sum_{i=1}^{n} \alpha_i f_i(x) g_i(x) \qquad 3.2$$

To sample from f, f_i is sampled and g_i is evaluated from equation 3.2.

3.4.1 Sampling of the distance between photon interactions

With a suitable random number generator the Monte Carlo technique can be employed. The first question one would ask oneself is how far a photon is to be transported in a medium before it interacts and from the stochastic nature of these interaction events how is this to be sampled by making use of random numbers?

The probability that a photon will interact is described by the total linear attenuation coefficient (μ). The mean free path is defined as 1/μ (Johns and Cunningham, 1983). This simply implies that the smaller the total linear attenuation coefficient, the smaller the probability for any type of interaction and therefore the photon travels larger distances before it interacts with the medium. However, the probability for an interaction to take place increases as the photon travels larger distances, for example more than one mean free path length.

Thus, to sample the distance traveled into the medium where an interaction will take place involves setting up a cumulative distribution function F(x) normalized over the unit interval since this is the interval over which random numbers are generated. If the probability that no interaction occurs for a photon traveling a distance x is given by $\exp(-\mu x)$ then $\mu\exp(-\mu x)dx$ is the probability that an interaction will occur between x and $x + dx$. The cumulative probability function would then look like this:

$$F(x) = 1 - \exp(-\mu x) \qquad 3.3$$

Equation 3.3 thus states that the probability for a photon interaction to occur would approach unity, as its traveling distance (x) becomes infinite in the medium. In the direct sampling method F(x) is sampled from the random number generator to yield a number r that is bounded by the unit interval [0,1]. To solve for x equation 3.3 is written as:

$$x = -(1/\mu)\ln(1-r) \qquad 3.4$$

But (1-r) is also a random number so that equation 4 becomes:

$$x = -(1/\mu)\ln(r) \qquad 3.5$$

The distance traveled by the photon is then calculated by equation 3.5 after r has been sampled. An important observation is that the cumulative probability function F(x) contains the total linear attenuation coefficient that is calculated from interaction cross section data of all photon interactions that could take place depending on the energy of the photon and the composition of the material. Qualitatively it can be seen from equation 3.5 that the distances between interactions increase with increase in photon energy since the interaction cross sections decrease overall with an increase in photon energy for the energy interval 1 to 10 MeV in tissue-like substances (Low atomic number)(Hubbell and Seltzer, 1995). Thus equation 3.4 models the increase in photon penetration or transmission through thick materials. The EGS4 code uses a slightly different variation of

equation 3.4 where the number of mean free path lengths ($N\lambda$) is sampled from the equation:

$$N\lambda = -\ln(r) \qquad 3.6$$

where $\lambda = M/(N_a\rho\sigma_t)$ and is defined as the mean free path of the photon. N_a is Avogadro's number and σ_t is the total atomic interaction cross section for the photon energy and material. Equation 3.5 is an example of the direct method of sampling.

3.4.2 Sampling of the interaction type

After the distance traveled by a photon is determined from random sampling the type of interaction must by sampled next. The EGS4 code uses the following distribution function to determine the interaction type:

$$F(i) = \frac{\sum_{j}^{i} \sigma_j}{\sigma_t} \qquad 3.7$$

The summation index j (running from 1 to i) in equation 3.7 symbolizes all the interaction types the photon can undergo and is normalized to a maximum of unity by the total atomic cross section. Thus F(i) has fractional values over the closed unit interval [0.1]. If a random number (r) is sampled then the inequality relation:

$$F(i-1) < r < F(i) \qquad 3.8$$

is evaluated by calculating equation 3.7 in steps of j until condition 3.8 is reached. If there are say three interactions possible for the photoelectric (j=1), Compton (j=2) and pair production (j=3) then the index satisfying condition 8 determines the type of interaction (Nelson et al, 1985).

3.4.3 Sampling of interaction dynamic variables

Since it would be quite laborious to explain all the different interactions' dynamic variable samplings performed by the EGS4 code only the principle of the sampling technique will be given.

An interaction cross section function is written in terms of the product of two functions say $F(\varepsilon)*G(\varepsilon)$ where the mixed method of sampling is employed and the interactions are written into a form analogous to equation 3.2. Interactions written in this form are: brehmstrahlung and pair production, Compton, Møller and Bhabha (Nelson et al, 1985).

3.5 Electron transport

When a photon travels through a medium it interacts tens of times before leaving it or all its energy is expended. When an electron travels through a medium it experiences hundreds or thousands of interactions in a medium through radiative and collisional processes. In order to simulate its energy loss and scattering through a medium efficiently a different approach is needed to account for energy loss and scatter. The EGS4 code utilizes the condensed random walk method. The electron loses energy in a continuos fashion by combining its interactions. The appropriate scatter angle is sampled from electron elastic multiple-scattering distribution functions like the Molière multiple-scattering distribution (Nelson et al, 1988). For a discussion on the selection of transport parameters and the effect of electron-electron multiple scatter the reader is referred to the work of Li and Rogers, 1995 and Simpkin and Mackie, 1990. Werner, 1997 made improvements on the over-estimation of the electron scattering power by modifying a function $FUDGEMS. It is used in determining the scattering power of atomic nuclei and the orbital electrons ($T_{nuclear}$ + orbital electrons.)

In an actual Monte Carlo simulation the user must define the lower bound of electron kinetic energy transport by specifying the variable ECUT. This is frequently taken as 0.521 MeV that corresponds to a kinetic energy of 10 keV. An ESTEPE variable is also

specified that indicates the maximum fractional energy loss an electron can experience. This parameter cannot be chosen too high (not more than 0.04) and if chosen low (0.01) then the simulation times are markedly increased though the actual electron transport becomes more realistic (accurate). In order to circumvent this an algorithm called PRESTA was introduced that optimizes accuracy of energy deposition with simulation speed (Bielajew and Rogers, 1986 and Nelson et al, 1988).

3.6 Running the EGS4 code

The programming language used in the EGS4 code is called MORTRAN. It can be thought of as a hybrid FORTRAN programming code because of its similarity. The use of the EGS4 code requires a knowledge of this MORTRAN code. The user must write a MAIN program that contains two subroutines, HOWFAR and AUSGAB (Nelson et al, 1985). HOWFAR determines the geometry of the simulation and AUSGAB determines the dose scoring zones. These subroutines have been generalized in user friendly codes such as DOSXYZ and BEAM that allow for the use of these powerful EGS4 transport simulation codes without any knowledge of MORTRAN.

3.7 The BEAM code

The ultimate radiotherapy problem is to simulate the dose distribution in realistic patient models for particle beams with Monte Carlo methods. The BEAM code was designed for the purpose of obtaining such particle beam information (Rogers et al, 1995). This EGS4 based code can be used for the simulation of various radiotherapy treatment machines such as linear accelerators, Co-60 units and orthovoltage machines. The user first specifies a set of component modules (CM's) that have various geometrical shapes, such as SLABS, JAWS, PYRAMIDS etc. This can be used to construct therapy machines. This 'machine' is then compiled and the user is tasked to supply a suitable input file describing the radiation control parameters, the dimensions of each CM, photon and electron energy transport cut-offs, number of histories etc.

The output consists of particles crossing a plane perpendicular to the beam is then stored in a phase-space file (PSF). These PSF's can occupy quite a large amount of disk space with $3*10^7$ particles occupying in the order of one GByte. The position where a PSF is collected is determined by the user and is located at the back of CM's. In the default mode up to three PSF's can be used at different planes perpendicular to a beam axis. These PSF's contain information of each particle scored in the plane. These parameters are each particle's charge, energy, position and direction cosines. If enough particles are scored in the PSF then it gives a complete description of the radiation beam at the plane distance from the primary source in say a linear accelerator. This PSF can then be used as a source for other simulations in the BEAM and the DOSXYZ codes.

The BEAM code allows for independent electron and photon transport energy cut-offs in each CM and employs other variance reduction techniques such as brehmstrahlung splitting, Russian Roulette, and photon forcing. If used sensibly it can reduce simulation times considerably without the loss of accuracy. Another useful feature of the code is to determine the dose contribution of particles originating from different CM's. This is useful when accelerator head scatter is studied and the dose contribution of electrons from the jaws is evaluated.

If disk space is a problem then another useful program called BEAMDP can be used to construct source models from these PSF's. The advantage of this is that not as many particles need to be scored in the PSF (Ma et al, 1995). BEAMDP manipulates data in PSF's to construct distribution functions like fluence, energy (spectral) distributions, angular distributions and to combine a set of two PSF's into one, etc. In this study raw PSF data was used in the Monte Carlo simulations and the BEAMDP code was used for PSF analysis only.

3.8 The DOSXYZ code

The DOSXYZ code is an EGS4 based code that can be used for 3D absorbed dose calculations. The co-ordinate system is Cartesian. The geometry consists of a rectilinear volume with perpendicular x,y and z directions. The dimensions of volume elements (voxels) can be set arbitrarily for each direction. The material in each direction can be specified and its density can be varied. Different sources can be used such as BEAM generated PSF's, parallel beams, point sources and BEAMDP generated beam characterization models. DOSXYZ also has a parameter ISMOOTH that can be used to redistribute PSF particles when used more than once during a simulation. In this study ISOURCE = 2 was used since the user can specify any desired direction of beam incidence into the volume.

Transport simulation parameters must be supplied through a user written input file. That contains information regarding transport energy cut-offs, the radiation source to be used, the number and dimensions of voxels, number of particle histories etc.

3.8.1 CT based patient models

The DOSXYZ code is tailor-made for simulating particle transport through patient models. CT slice data contains a cross section map of CT numbers that represents different tissue types. The problem is that these CT numbers are not suitable for direct incorporation into DOSXYZ. In this study a method was devised to manipulate CT data by transforming it into a tissue matrix (Du Plessis et al, 1998) (See section 6.4). The CT image was reduced to 57 tissue types and the cross section data was calculated (PEGS4). These transformed data could be used directly in the DOSXYZ code through a suitable user written input file.

3.9 Summary

Monte Carlo codes such as the EGS4 code are being used extensively in medical physics applications. The basis for all Monte Carlo codes is accurate interaction cross section data that are pre calculated in such codes as in the EGS4 and ITS3 codes. Stochastic events can be sampled from suitable random number generators like the multiplicative congruential algorithm used by EGS4. User friendly codes such as BEAM and DOSXYZ have been developed to allow users without a knowledge of MORTRAN to handle many dosimetry problems by writing suitable input files. Patient-like geometries are essential if dose distributions are to be simulated in realistic patient models. This can be done by transforming CT numbers to materials for direct use in DOSXYZ.

The main drawback of Monte Carlo dose calculations is that considerable time is needed for accurate dose calculations. The stochastic nature of radiation interactions has the effect of varying the dose scored in a voxel. This variation can be reduced provided the number of simulations is increased. This method unfortunately converges slowly. If the standard error (σ) is to be halved then the number of histories must be increased fourfold. The standard error converges like:

$$\sigma = \frac{1}{\sqrt{N}} \qquad 3.9$$

where N is the number of histories.

Monte Carlo simulations demand considerably more time if high accuracy is required in simulation data. Various techniques, known as variance reduction, can be employed to actually speed up simulations. Some of these methods include PRESTA and range rejection. Nelson et al, 1988, gave a good account of different types of variance reduction techniques. Some techniques used in this study include the setting of global energy transport cutt-offs for electron transport, the use of the PRESTA algorithm and the re-use of PSF's.

CHAPTER 4

Inhomogeneity correction methods

4.1 Introduction

The scope of this study is to evaluate treatment planning systems by means of comparing treatment planning system generated dose distributions with dose distribution data calculated by Monte Carlo methods through simulated coupled photon-electron transport. The main focus will be on the evaluation of 8 MV photon dose distributions in CT slice based patient models calculated with a commercial treatment planning system and with Monte Carlo simulation methods. In this section some basic inhomogeneity correction methods are discussed. These correction methods form the basis for dose distribution calculations in radiation treatment planning. Some of them can be used in manual dose distribution calculations , while other more complex types must utilize computers for fast calculation.

If a known photon dose distribution in a homogeneous medium is compared with the dose distribution in the same medium but with a small inhomogeneity (different material or density) present, a small difference between the dose distributions will be observed. The presence of the inhomogeneity distorts the homogeneous dose distribution near it. The effect diminishes as the dose distribution is evaluated further from the inhomogeneity. If this inhomogeneity is displaced to another location in the homogeneous medium (but still in the x-ray beam), there will be a different distortion effect in the dose distribution. To complicate the situation another different inhomogeneity may be introduced into the medium. This will cause another unique distortion of the dose distribution. It is not difficult to grasp that an infinite number of different dose distributions can be obtained in such a way.

In a real patient there is a large number of tissue types present. A beam of photons passing through the patient will be scattered and absorbed to various degrees characteristic of the beam energy and geometry and composition of each tissue type. In order to calculate the dose in the patient model a correction for these inhomogeneous tissue distributions must be made. The aim of such correction methods is to relate the photon dose distribution in a homogeneous medium such as water to the dose distribution in an inhomogeneous medium for the same field size and beam energy. This is known as inhomogeneity correction.

Some inhomogeneity corrections are designed to calculate correction factors (C) which can be defined as the ratio of the dose at a point in a heterogeneous medium (D_{med}) to the dose at the same point in a homogeneous medium which is often taken as water (D_{water}). Mathematically the correction factor can be expressed as:

$$C = \frac{D_{med}}{D_{water}} \qquad 4.1$$

In the following sections the development of various inhomogeneity correction methods will be discussed with the aim of deriving the correction factor C.

4.2 The effective attenuation method

Before the advent of CT scanners inhomogeneity corrections were made on patients by only identifying gross structures such as the lungs and bone (Young and Gaylord, 1970) which were considered large inhomogeneities. With conventional diagnostic x-ray equipment only large inhomogeneities such as bone and lung could be resolved. Thus apart from these tissue types the rest of the tissues were considered water equivalent. Inhomogeneity correction factors needed only to be obtained for bone and lung.

4.2.1 Radiological path length

A technique was developed suitable for manual calculation of these inhomogeneity correction factors namely the effective attenuation method. In this approach a radiological depth (d) was defined as follows (Siddon, 1985):

$$d = \int_{s}^{p} \rho(r)dl \qquad 4.2$$

The radiological depth is equivalent to the effective depth of a ray from an x-ray source S to the point P of dose calculation in a heterogeneous medium with a density distribution $\rho(r)$. It is calculated by multiplying each section of the ray length, which passes through a homogeneous section of the medium with the density of that section. The radiological lengths obtained from all sections intersecting the ray line is added to obtain the radiological depth. The calculation of the radiological depth is illustrated in figure.1.

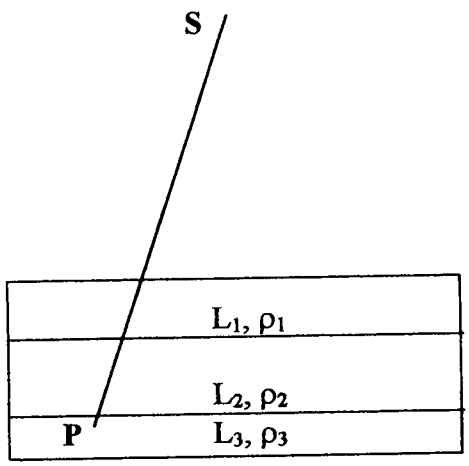

Figure 4.1 A ray extending from a source (S) to a dose calculation point (P) is intersecting three regions of different density (ρ_1,ρ_2 and ρ_3) each of path length (L_1, L_2 and L_3). The aim is to calculate the radiological path length (d) in the heterogeneous medium.

Consider a ray extending from a source (S) to a dose calculation point (P) in a heterogeneous medium. The medium is made up of 3 layers of different density and the ray is traversing the layers with path lengths of L_1, L_2 and L_3. The radiological path length is calculated as:

$$d = L_1 * \rho_1 + L_2 * \rho_2 + L_3 * \rho_3 \qquad 4.3$$

From a physical point of view the role of the effective radiological path length can be described as follows. In figure 1 let's assume that the first layer is water equivalent with a density $\rho_1 = 1$. The next layer has a density of say $\rho_2 = 0.5$ and the third layer is also water equivalent ($\rho_1 = 1$). A dose D' is calculated at point P. If all three layers were water equivalent then a dose D would have been calculated at point P. Dose D is less than dose D' because the middle layer was of a higher density (water equivalent).

4.2.2 Effective attenuation

This can be described by means of attenuation. For the case in which the whole medium was water equivalent the dose at point P was less due to more attenuation of the beam in the middle layer of the medium. For the case where the middle layer had a smaller density the dose at P was larger because more photons could reach the third layer. The beam attenuation was less. Thus the dose at point P increased by a certain fraction for each unit length of water equivalent material missing in the middle layer. Thus the radiological path length plays the role of an effective attenuation coefficient for the radiation beam.

The correction factor C is calculated as:

$$C = e^{\mu'(d'-d)} \qquad 4.4$$

where d' is the physical path length of point P and d is the radiological path length.

Some limitations of these methods are that they do not take field size, the position and shape of the inhomogeneity or electronic equilibrium into account (Orton, 1982).

4.3. Effective SSD and isodose shift methods

4.3.1 Effective SSD method

In this method the dose to a point P in a medium is calculated as follows: From figure 4.2 the dose in the medium is, to a first approximation given by the value on an isodose chart obtained from measurements made in water for the same field size. Due to an inhomogeneity further 'upstream' at A, the dose at P will be affected.

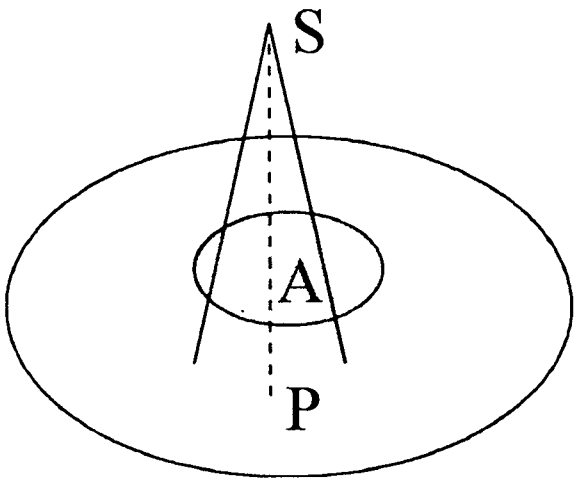

Figure 4.2 A radiation field, originating from source, S, irradiates a phantom which is water equivalent except for region A, which have a different density.

The effective SSD method calculates the dose at P as follows: The radiological path length is first calculated to obtain the water equivalent depth d'. The isodose chart is then shifted to this new position d'. The dose at point P is then the value on the isodose chart at P after an inverse square law correction has been applied.

In mathematical terms the correction factor C can be expressed as:

$$C = \frac{P(d', W_0, F')}{P(d, W_0, F)} \left(\frac{F + d'}{F + d} \right)^2 \qquad 4.5$$

where $P(d',W_o,F')$ is the new percentage depth dose at point P for a field size W_o and d' is the water equivalent depth. $P(d,W_o,F)$ is the percentage depth dose at P, at depth d, for a totally water equivalent phantom. The latter term in parenthesis is an inverse square law correction to account for the difference in distance to source from the isodose chart reference point S. F is the source skin distance.

4.3.2 Isodose shift method

This method is nearly the same as the effective SSD method. Instead of moving the isodose chart to the point d', the calculated radiological path length, it is shifted only a fraction of the distance d-d'. The correction factor is mathematically expressed as:

$$C = \frac{P(d'',W_o,F')}{P(d,W_o,F)} \qquad 4.6$$

where d'' is a depth which can be regarded as an equivalent depth containing the inverse square law correction.

$$d'' = d - n(d - d') \qquad 4.7$$

where n is the fraction of the distance (d - d') that the isodose chart is shifted. This fraction is beam energy dependent. The advantage this method provides is that a dose value can be read off directly from the isodose chart. Limitations of both correction methods are their inability to take electronic equilibrium, the shape and position of inhomogeneities into account (Orton et al, 1982)

4.4. Scatter-Air ratios (SAR's)

This method was developed to calculate the dose at a certain point in a medium due to scatter from other points in an irradiated medium (Cunningham, 1972). These scatter-air ratios were derived from tissue-air ratio's (TAR's), a quantity that describes the fraction

of the dose in a medium at point p for a certain field size to the dose at the same point in air (Johns and Cunningham, 1983). The scatter-air ratio is defined as:

$$S(d,r_d) = T(d,r_d) - T(d,0) \qquad 4.8$$

where $S(d,r_d)$ is the scatter air ratio for a beam of radius r_d at depth d,

$T(d,r_d)$ is the tissue-air ratio at depth d for the same field size and

$T(d,0)$ is the tissue-air ratio at depth d for a zero area field size (pencil beam)

This data was obtained from TAR plots against field size extrapolated to zero area. The SAR increases rapidly as a function of field size for small field sizes but gradually saturates to become a more slowly varying function at field sizes of radii $\geq$ 25 cm. The function is a monotonically increasing function of the field size. This suggests that the dose due to scatter will increase at a point in a medium irradiated by increasing fields.

4.4.1 Scatter dose calculations using the Clarkson method

In order to use these SAR's in dose calculations from scattered radiation to a point P the Clarkson method is used (Cunningham, 1972 and Thames, 1973). The total scatter (S) can be calculated from the formula:

$$S = \sum_{i=1}^{n} S(d,r(\theta_i)_d)\frac{\Delta\theta_i}{2\pi} \qquad 4.9$$

where $S(d,r(\theta_i)_d)$ is a scatter function, which is a measure of the dose delivered by scattered radiation to a point at depth d, $r(\theta_i)_d$ is the distance from the calculation point to the beam edge. The index n describes the number of sectors over which to sum in describing the beam. $\Delta\theta_i$ is the angular width of the sector. Cunningham has shown how to derive the scatter function for non-uniform beams irradiating homogeneous phantoms

as well as uniform beams irradiating non-homogeneous phantoms by casting the SAR's in differential form.

The theory was tested by example of Thames and Pla et al. who applied the Clarkson integration method to obtain first order scattering in off-axis points in a cobalt beam (Thames, 1973) and the calculation of dose profiles for partially attenuated photon beams (Pla et al, 1988). An accuracy of 3 percent was observed for beam profiles that were partially attenuated by irregular lead blocks as measured in water with 4 MV x-rays. Limitations of this technique were that it could not account for electronic equilibrium perturbation at interfaces between different media (Orton, 1982).

4.5. The generalized Batho-power law.

This technique was proposed by Sontag and Cunningham in 1977 (Sontag et al, 1977). They expanded the Batho-power law to make inhomogeneity corrections to the dose below and in the inhomogeneity itself. This correction gave a 6 to 7 percent improvement in dose calculation accuracy. They derived the dose in a grid point P of a patient model made up of CT slices as:

$$D'(p) = D(p) * CF \qquad 4.10$$

The dose at a certain point in a homogeneous phantom is D(p) and D'(p) is the dose at the same point but with the inhomogeneity taken into account. CF is the correction factor, which relates the dose at a point in an inhomogeneous phantom to the dose to the homogeneous phantom.

4.5.1 Derivation of correction factor

Batho, Young and Gaylord (Young, 1970) derived a method to obtain the correction factor employing tissue-air ratios (T(d,A)) and electron densities (ρ_e) of the inhomogeneities.

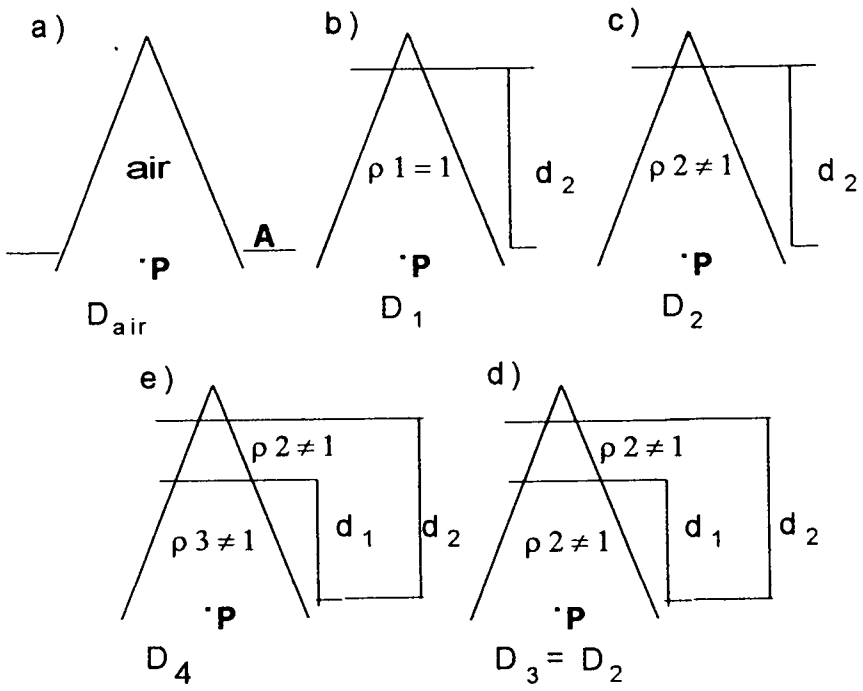

Figure 4.3. The geometrical set-ups for derivation of tissue-air ratio power law. The diagram was is from Med. Phys. 4 (1977), 423

They considered the point P in figure 4.3a which received photon radiation in air. A small mass at P received a dose D_{air}. In figure 4.3b the point P was at the same location, but instead of air the phantom is now a tissue like homogeneous material. The dose D_1 is measured at a depth d_2 below the phantom surface for a field size A. The dose D_1 is related to that in air by the tissue-air ratio as:

$$D_1 = D_{air} * T(d_2, A) \qquad 4.11$$

If the tissue-like material's physical density is doubled as in figure 4.3c this means that the electronic and atomic densities also double. This results in a doubling of all interaction types, meaning that the tissue-air ratio is to be applied twice by multiplication. The dose at point P will now be given as:

$$D_2 = D_{air} * [T(d_2, A)]^2 \qquad 4.12$$

In more general terms: if the density is altered by a factor ρ then the dose will be given by:

$$D_2 = D_{air} * [T(d_2, A)]^{\rho} \qquad 4.13$$

In the therapeutic energy range of linear accelerators (6 - 15 MV) the Compton interaction dominates the photoelectric and pair production processes. The physical density can then be replaced by the relative electron density, which is the ratio of a tissue's electron density to some reference tissue's electron density. Note that this is an approximation since the photoelectric interaction dominates for photon energies roughly less than 100 keV. The pair production interaction dominates for energies above a few MeV. These interactions are also functions of the atomic number (Z) of the tissues, which does not enter in equations 4.11 and 4.13.

From eq. 4.11 and 4.13 the dose to a tissue-equivalent material and a medium with relative electron density ρ_2 is given as:

$$D_2/D_1 = T(d_2, A)^{\rho 2}/T(d_2, A) \qquad 4.14$$

The dose D_4 in figure 4.3e can be derived in more general terms:

$$\frac{D_4}{D_1} = \frac{T(d_1, A)^{\rho 3 - \rho 2}}{T(d_1, A)^{1-\rho 2}} \qquad 4.15$$

The definition of the correction factor is given by eq. 4.16. for inhomogeneities which have the same effective atomic number as muscle.

$$CF = \frac{T(d_1, A)^{\rho a - \rho b}}{T(d_1, A)^{1-\rho b}} \qquad 4.16$$

This equation is of the same form as developed by Batho. It does not account for the atomic number differences between non-tissue like materials and tissue. This can be corrected for by multiplying the Batho equation (eq. 4.16) with a ratio of mass energy absorption coefficients.

$$CF = \frac{T(d_1, A)^{\rho a - \rho b}}{T(d_1, A)^{1-\rho b}} * \frac{(\mu_{en}/\rho)_{\rho_a}}{(\mu_{en}/\rho)_{\rho_b}} \qquad 4.17$$

This is the generalized Batho equation.

This inhomogeneity correction method could be applied to patient models based on CT scans and was more accurate than the effective linear attenuation method. Limitations of this correction method are that the shape of the inhomogeneity structures are not taken into account nor is the electronic equilibrium at the interfaces (Orton. 1982)

4.5.2 Limitations in model

According to Sontag and Cunningham, 1977. the generalized Batho-power law is derived on the following assumptions:

1) Only geometry above the calculation point is considered. This means that back scatter due to inhomogeneities further downstream which could influence the dose is not taken correctly into account.

2) The effect of the inhomogeneity on the dose at the point is independent of its thickness.

3) Electronic equilibrium exists but at the interface between adjacent inhomogeneities it will fail and can lead to large errors in the dose. This effect will be more pronounced for high energy photons where the electrons set in motion will travel a few centimeters.

4) The lateral dimensions are assumed to be at least that of the beam.

Van't Riet et al, 1985, tested the generalized Batho-power law. They did a series of lung inhomogeneity corrections to 23 patients. They concluded that:

1) For small field sizes the method showed good results when compared to experimental data. This was shown by El-Khatib and Battista in a similar paper.
2) The method is not valid in the build-up region at the lung/tissue interface.
3) Electronic equilibrium will play an important role at high photon energies.

4.5.3 Improvements in model

In 1984 El-Khatib and Battista showed that the Batho method could be markedly improved by using tissue-maximum ratio's (TMR's) instead of Tissue-air ratio's (TAR's). The accuracy improved by 5percent for Co-60 radiation for larger fields.

4.6 The equivalent tissue-air ratio method

The equivalent tissue-air ratio inhomogeneity correction method (ETAR) was proposed by Sontag and Cunningham in 1978 (Sontag et al, 1978). The primary use of this correction method was to do inhomogeneity correction methods in 3 dimensional patient models based on CT-slice data after conversion into electron densities. This correction method belonged to a third generation which examined the shape, size and position of inhomogeneities and was capable of running on computers with only 32k of memory. The method of correction involves the determination of a quantity, analogues to a tissue-air ratio, derived for phantoms containing water equivalent materials by scaling the depth and field size in an appropriate manner. The correction factor is defined as:

$$C = \frac{T(d',r')}{T(d.r)} \qquad 4.18$$

where T(d',r) is a tissue-air ratio for the scaled field size r' and the scaled depth d'
and T(d,r) is a tissue-air ratio for the unscaled depth d and field size r.

This method gave an accuracy of 2 percent under certain conditions.

4.6.1 Theoretical development

The tissue-air ratio for a medium of density (ρ) can be expressed as:

$$T(d,r) = T(d^{*}\rho, r^{*}\rho) \qquad 4.19$$

$T(d,r)_{\rho}$ is the tissue-air ratio at depth d, and radius r for a medium with relative electron density ρ. $T(d^{*}\rho, r^{*}\rho)$ is the tissue-air ratio for water for depth d.ρ and field radius r*ρ. The tissue-air ratio is expressed as the sum of a scatter (S) and a primary component (zero area field size):

$$T(d,r) = T(d,0) + S(d,r) \qquad 4.20$$

From eq. 4.19 and eq. 4.20 it can be shown that:

$$T(d,r)_{\rho} = T(d^{*}\rho,0)_{\rho} \quad \text{and} \quad S(d,r)_{\rho} = S(d^{*}\rho, r\cdot\rho) \qquad 4.21$$

4.6.1.1 Evaluation of primary component

It is assumed that the primary component for a mono energetic radiation beam is of the form:

$$T(d,0) = \frac{e^{-\mu d}}{A_{eq}} \qquad 4.22$$

A_{eq} is a factor associated with the determination of the absorbed dose in a small mass of medium material. For a phantom with relative electron density (ρ) for the same depth (d) the exponent would become [-μρ.d] and it would be the same as if a unit density phantom was described at depth d*ρ. This argument can also be extended to a heterogeneous photon beam.

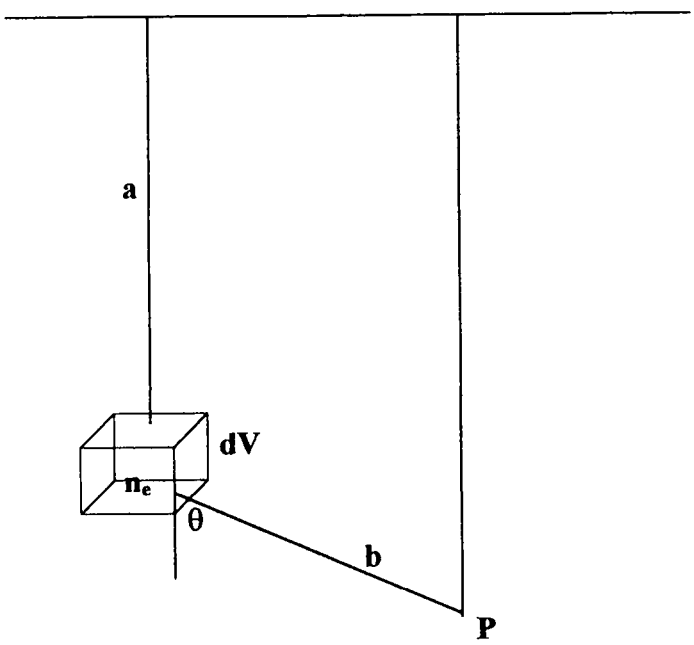

Figure 4.4 The dose is determined at point P. Scatter radiation reaches the point from a volume dV at distance a, from P. The phantom is of unit density and dV has an electron density n_e.

4.6.1.2 Evaluation of scatter component

The dose is to be determined at a point (P), see figure. 4.4, in a phantom with unit density as a result of scatter radiation reaching P from a volume element (dV) at a distance (a) from P. The portion of the scatter-air ratio due to single scattered photons can be written as:

$$S(d,r) = \frac{1}{A_{eq}\left(\frac{\mu}{\rho}\right)E_{abs}} \int_{\nu} \left[e^{-\mu a}\right] \cdot \left[n_e \frac{d\sigma(\theta)dV}{d\Omega}\right] \cdot \left[\frac{e^{-\mu(\theta)b}}{b^2}\right] \cdot \left(\frac{\mu(\theta)}{\rho}\right) \cdot E(\theta)_{abs} \qquad 23$$

where $\frac{\mu}{\rho}$ is the mass attenuation coefficient for the primary photons in the scattering medium. E_{abs} is the average energy absorbed per primary photon interaction, μ is the linear attenuation coefficient for primary photons, a is the path length to the scattering

volume dV, n_e is the number of electrons per unit volume, $\frac{d\sigma(\theta)}{d\Omega}$ is the Klein-Nishina probability per electron of scattering a photon through angle θ, $\mu(\theta)$ is the linear attenuation coefficient for the scattered photons, b is their path length to point P, $\frac{\mu(\theta)}{\rho}$ is the mass attenuation coefficient for the scattered photons and $E(\theta)_{abs}$ is the average energy absorbed per scattered photon interaction.

For a homogeneous phantom the linear attenuation coefficients, the number of electrons per volume and the distances must be scaled through multiplication by ρ, the phantom density.

For a non-homogeneous phantom the density differs at certain locations. An equivalent tissue-air ratio method was proposed to account for multiple scatter of the photons from every irradiated volume element in the phantom. Sontag et al, 1977. proposed a weighted average of the density (ρ') to evaluate the denominator of eq. 4.23. They found this effective density to be:

$$\rho' = \frac{\sum_i \sum_j \sum_k \rho_{ijk} \cdot W_{kijk}}{\sum_k W_{ijk}} \qquad 4.24$$

where ρ_{ijk} is the density and W_{ijk} is the weight factor for each density element. The function of these weight factors is to express each density element's importance in scattering photons to point P.

4.6.2 Use with CT data

A patient model can be constructed from CT slice data. This CT data is then converted to electron density data. If say n slices are used for the patient model the effective density is obtained by combining all the slices into a single slice by using the following formula:

$$\rho_{ij} = \frac{\sum_k \rho_{ijk} \cdot W_k}{\sum_k W_k} \qquad 4.25$$

where W_k are overall weighting factors for the effect of each slice in producing scatter. Each element in this new slice is a weighed average of all elements that have the same xy co-ordinates in the n slices. The result is the creation of an effective scattering slice a distance Z_{eff} from the slice of calculation.

In the next step the effective density is then calculated. The formula has the same form as eq. 4.24, but W_{ijk} is evaluated at Z_{eff}. From $W_{ijk}(Z_{eff})$ the scatter-air ratio is obtained for each point of calculation in the model and from the equivalent depth the effective tissue-air ratio can be calculated.

4.6.3 Evaluation of ETAR method

Studies of ETAR inhomogeneity corrections on 100 CT based patient models were evaluated (Mah and Van Dyk, 1991). These patients have undergone radiation treatment in the thorax which includes the lungs. It was found that for parallel-opposing photon fields encompassing the mediastinal and bilateral lung regions the correction at the point of target absorbed dose was as much as 5 to 16 percent for photon energies between ^{60}Co and 25 MV. A disadvantage of the ETAR method is its inability to handle electron transport leading to errors at tissue interfaces due to electronic disequilibrium. In a study of photon dose distributions near interfaces between different materials undertaken by Sauer, 1995 it was found that for high Z-materials the dose was enhanced between 33 to 14 percent in front of materials like iron and aluminum due to back scatter. The attenuation properties of iron caused a decrease in dose at the back of between 16 to 2 percent for 5 to 16 MV photon energies.

4.7 Summary

The treatment planning system (CADPLAN) under evaluation in this study uses correction based algorithms. The Batho and ETAR methods for inhomogeneity corrections are some of the more advanced methods that are used by the treatment planning computer. None of these methods are capable of modeling electronic equilibrium at different material/tissue interfaces. This is a point of prime concern and justifies the evaluation of the CADPLAN with a benchmarking dose calculation method such as Monte Carlo dose simulations.

CHAPTER 5

Treatment Planning Systems

5.1 Introduction

Treatment planning systems form an integral part of radiation therapy. It is used for the optimal radiation dose planning to treat tumors in the body. The aim is to obtain a uniform dose distribution in the target volume which encloses the tumor and to spare other critical organs and healthy tissues, with regard to the radiation dose they will receive. This is achieved by modifying the total x-ray dose distribution through a selection of the appropriate x-ray field sizes, angles of incidence on the patient model and the use of wedged fields in such a configuration that the above conditions hold. Treatment planning system use x-ray beam data, patient model data and inhomogeneity correction algorithms for the effective calculation of the dose distributions.

Beam data is obtained from water bath measurements of the depth dose and beam profiles of various x-ray field sizes. Since this data is machine specific this set of measurements must be performed for all teletherapy units that will be used for radiation treatments. This beam data is obtained by setting up a tank filled with water such that x-ray beams impinge perpendicularly onto the water from above (accelerator gantry angle at zero degrees). The water tank is equipped with an ionization chamber that can be moved using electrical motors to any desired point in the water. This feature enables the use of this probe to scan automatically in the beam axis direction to obtain percentage depth dose measurements as well as cross plane and in- plane scans to obtain x-ray beam profiles at predetermined depths. These measurements are repeated at several field sizes for open and wedged x-ray beams. This data is used by the treatment planning system in modeling arbitrary rectangular x-ray fields.

Patient information is obtained from CT slice data of the patient and is imported directly into the treatment planning system. CT data contains information regarding the relative total attenuation of material X to that of water at the scanner x-ray beam energy, that lies in the 80 – 130 kVp range, dependant on what CT scanner is used. This CT slice data is representative of the electronic density in each image pixel. This is very useful since inhomogeneity corrections can be made readily, with the added advantage that a complete map of different tissues can be obtained and taken into account in inhomogeneity corrections. The use of CT data therefore improves the use of inhomogeneity corrections and outperforms conventional radiology methods for obtaining internal structure information. With the older methods only structures such as lung and bone could be resolved, therefore allowing only crude estimates for inhomogeneity corrections to the dose (Johns and Cunningham, 1983).

5.2 The CADPLAN treatment planning system

The CADPLAN treatment planning system uses two methods of inhomogeneity corrections namely the generalized Batho-power law, which can calculate inhomogeneity correction factors (CF's) inside the inhomogeneity, as well as the equivalent tissue-air-ratio (ETAR) method. The latter method is more accurate than the first because it also takes the inhomogeneity size into consideration. These correction methods are explained in chapter 2. Briefly: both methods can be described as algorithms designed to calculate correction factors (CF's) in each voxel where the dose is calculated. These CF's are then multiplied by a corresponding dose in water for a certain field size after certain corrections had been made regarding changed SSD, that alters percentage depth dose curves, and obliquity factors to account for the distortion of the dose in water due to obliquely incident fields. Thus dose distributions are calculated by assuming that the patient is initially water equivalent. In this chapter the basic operation of the treatment planning system will be discussed with regard to beam modeling and inhomogeneity correction methods for photons.

5.2.1 External beam modeling

The CADPLAN uses two photon beam models for calculating dose distributions namely the regular photon beam model for rectangular field shapes, and the pencil beam convolution model for the calculation of dose in irregularly shaped photon beams. The regular model first calculates the dose in a water equivalent patient model and then calculates a CF for each voxel by using a chosen inhomogeneity correction method.

The generalized Batho-power law calculates these CF's more rapidly than the ETAR method but assumes that the inhomogeneities are finite only in the beam direction. The ETAR method includes the scatter component of radiation from adjacent slices in the inhomogeneous material.

5.2.1.1 Regular x-ray beam model

When an arbitrary square or rectangular x-ray beam is modeled by the CADPLAN, it uses the measured x-ray beam input data for this purpose. For irregular fields it uses a pencil beam convolution modeling technique. For the purpose of this study the treatment planning system was evaluated for 8 MV x-ray beams using the regular beam model. Normally the beam data are measured in a water tank for a specific therapy unit such as a linear accelerator. This will usually be depth dose data and field profile data for various square photon field sizes ranging from the smallest to the largest field size. This will include open as well as wedged fields.

In this study the set of input beam data was actually obtained with the DOSXYZ Monte Carlo code by simulating various photon beams in a mathematical water bath. These photon beams were characterized by phase space files containing millions of photons emerging from a generic accelerator as produced by the Monte Carlo BEAM code.

5.2.2 Dose Calculations

The next sections in this chapter give an outline of the different functions used by the CADPLAN treatment planning system for actually calculating dose distributions in CT based patient models. The treatment planning system actually calculates the dose in matrices consisting of 160x112 pixels in each CT slice of the patient model. The grid spacing of these dose matrices can be adjusted to 2.5 mm, 5 mm, 1 cm or 2 cm. The physical dimensions covered by the 2.5 mm grid corresponds to 400 mm x 280 mm. The treatment planning system can display the isodose distribution of these dose points superimposed on a CT slice image of the section that was used for dose calculations. A grid spacing of 5 mm was used to calculate dose distributions in patient models of a head, lung and prostate treatment plan.

The dose in a grid point (P) can be expressed as:

$$D(p) = PDD(d) * OA(x, z, d) * CO * CF \qquad 5.1$$

where D(P) is the dose at point P,
PDD(d) is the percentage depth dose at depth d,
OA(x,z,d) is the off-axis factor at the point (x,z) in a plane at depth d perpendicular to the central axis of the field,
CO is the skin obliquity factor for oblique x-ray fields and CF is the inhomogeneity correction factor that the dose in water must be multiplied with to obtain the dose in 'tissue'.

The dose is first calculated for a water equivalent phantom or patient at point P. It is then corrected for skin obliquity and inhomogeneities. The dose at point P at co-ordinates (x,z,d) is given as a product of a depth dose at d and the off-axis factor.

5.2.2.1 Percentage depth dose curves

As mentioned the CADPLAN uses percentage depth dose data to first calculate the dose in a water equivalent patient model. These data are only measured for a few fixed equivalent field sizes at a fixed source-phantom distance. In order to modify these percentage depth dose curves for other field sizes and skin source distances some corrections needs to be done. The first is a correction for a change in field size and source skin distance and then one for the inverse square law.

The expression for the percentage depth dose data has the following form:

$$DD(d_1) = DD_m(d, A) * CF_{dd}(d) * CF_{inv} \qquad 5.2$$

The treatment planning system stores depth dose curves for photon beams as measured in a water bath. The field dimensions are from 0 cm to 40 cm. It is measured at the source phantom distance (SPD), (usually at the isocenter, which is 100 cm for Philips machines). These depth dose curves can then be modified to include isocentric treatment plans where the source-skin distance (SSD) is less than 100 cm. The correction of the depth dose curves is given by the following formula:

$$CF_{dd}(d) = \frac{T(d, A_2)}{T(d, A_1)} * \left(\frac{SSD + D_{max}}{SSD + d}\right)^2 * \left(\frac{SPD + d}{SPD + D_{max}}\right)^2 \qquad 5.3$$

where $A_1 = K_1 * A$, $A_2 = K_2 * A$ and D_{max} is the depth of the maximum dose.

$$K_1 = \left(\frac{SPD + d}{SPD}\right)$$

$$K_2 = \left(\frac{SSD + d}{SSD}\right)$$

where T(d,A) is the tissue-air ratio or tissue-phantom ratio (Johns and Cunningham, 1983) at a depth d for equivalent square field size A. D_{max} is the dose maximum depth of the depth dose curve.

This correctional factor modifies the original depth dose curve due to the difference in source skin distance.

The inverse square law is taken into account by means of a correction factor:

$$CF_{inv} = \left(\frac{SSD_s + D_{max}}{SSD + D_{max}} \right)^2 \qquad 5.4$$

where SSD_S is the distance to the body surface and SSD is the original distance at which the water bath measurements were taken to obtain the entered depth dose data for the planning system.

The depth dose is given at depth d as defined for an equivalent square field. This can be calculated by the following:

$$A = \frac{2 * a * b}{a + b} \qquad 5.5$$

where A is the side length of the equivalent square,
a and b are the side lengths for the original rectangular field for which the dose distribution is calculated in the patient model. The concept of an equivalent square field arises from the fact that the input beam data for the CADPLAN consists of various square x-ray fields. To adjust the PDD for a rectangular field it must be set to some equivalent square field. The rule to use here is that square fields and rectangular fields are equivalent if the ratios formed by the division of area to perimeter are the same (Johns and Cunningham, 1983). These two fields would then have the same PDD curves. The PDD in equation 5.1 can be obtained for any x-ray field, say a x b. A study by Yu, et al, 1995

has shown that head scatter factors could vary as much as 3 percent if field sizes were defined by interchanging the field dimensions between the upper and lower jaw pairs. This effect was studied on a Varian Clinac 2300CD and a Clinac 600C accelerator for 6 and 15 MV photon beams. This effect became more pronounced at large field sizes. The next step involves the determination of the off-axis ratio.

5.2.2.2 Off-axis ratio

When the percentage depth dose value at point P is calculated one should keep in mind that it actually corresponds to the dose on the beam axis (central axis) for the given field set up for treatment planning. For grid points lying in the same plane at depth d perpendicular to the beam axis but displaced from the central axis the dose would not correspond to that of the central axis percentage depth dose value. Therefore the dose at those grid points must be calculated from the corresponding percentage depth dose value and be multiplied by a suitable factor that takes the geometry of the beam into consideration. These factors are known as off-axis ratios.

Off-axis ratio's have the prime advantage that they can model an x-ray beam from a limited number of measurements that include one depth dose curve and 5 beam profiles at fixed depths for a number of x-ray field sizes (Storchi and Woudstra, 1995). The off-axis ratio is calculated as a product of the primary off-axis ratio and boundary factors. The primary off-axis ratio describes the beam profiles for an infinite uncollimated field. The definition of these off-axis ratios (OAR's) is described as:

$$\mathrm{OAR}(r,d) = \frac{D(r,d)}{D(0,d)} \qquad 5.6$$

where the off-axis ratio at depth (d) and radial distance (r) is given as the ratio between the dose at point (r,d) to the dose (0,d) at depth d on the central axis.

5.2.2.3 Wedged and open fields

Wedges are used to modify the dose gradient inside a patient in order to change the beams to a specific geometry that would result in a maximally uniform dose to a target volume, which includes the tumor. The photon beam is therefore attenuated to various degrees in the lateral wedge direction. The off-axis ratio is modified to take this into account by multiplying the open field off-axis values with wedge factors defined from measured beam profiles.

The CADPLAN makes use of the following model to calculate the off-axis ratio for open fields: (fields without any attenuating material in the primary beam):

$$OA(x,z,d) = P_c(r,d) * P_B(x,d,FS_x) * P_B(z,d,FS_x) \qquad 5.7$$

where $r = (x^2 + z^2)^{0.5}$

$P_c(r,d)$ is an envelope profile value at a radial distance r at depth d in the xz-plane perpendicular to the beam axis. Envelope profiles are derived from the measured beam profiles at 5 standard depths and are stored in an envelope profile table. This contains the beam profiles as well as an infinite beam profile.

$P_B(x,d,FS)$ is the boundary profile value at distance x at depth d for a field size FS. Boundary profiles describe the shape of the beam profiles in the boundary region of an infinite beam, limited by collimating jaws. Boundary profiles are derived from the measured beam profiles by dividing them by the envelope profile.

For wedge fields these profiles are calculated as:

$$OA(x,z,d) = OA_0(x',z',d_1 + y_w(x)) * P_{w/o}(x,d) \qquad 5.8$$

where $x' = x*J$ and $z' = z*J$,

J is a scalefactor defined by eq. 5.9.

$$J = \frac{(SSD + d + y_w(x))}{(SSD + d)} \qquad 5.9$$

and $y_W(x)$ = is the equivalent water thickness of the wedge.

$OA_0(x',z',d_1+y_w(x))$ is calculated with eq. 5.7
The $P_{w/o}(x,d)$ term is the lateral wedge profile corrected for the off-axis influence of the open field.

5.2.2.4 Skin obliquity correction factor

The skin obliquity correction factor (CO) arises from the situation where a photon beam of certain field size A is entering the body surface of a patient at an area which is curved and not perpendicular to the beam axis. This has the effect of shifting the isodose lines in dose distributions therefore altering the dose delivered to the patient.

CADPLAN makes this correction by using TAR or TPR ratio's and the inverse square law, where TAR is the tissue-air-ratio and TPR is the tissue-phantom-ratio. A short definition of TAR is the ratio of the dose at a certain depth (d) on the beam axis in a tissue equivalent material (water) for a certain field size (A) at an SSD (z) to that in air for the corresponding point at depth (d) for the same x-ray field size and SSD.
The tissue-phantom-ratio is defined as the ratio of the dose in water for a certain field size and SSD to the dose in a phantom material at a point (a) that is the same distance from the source but not necessarily the same SSD for the same field size in the plane of point (a). If the depth dose is calculated at d and the depth from the calculation point to the patient surface is d_1. a correction for the skin obliquity factor is given as:

$$CO = CO_{dd} * \left(\frac{SSD + d_{bc}}{SSD + d_{fe}} \right)^2 * \frac{TAR(d_{bc}, A_4)}{TAR(d_{bc}, A_3)}$$

where

$$CO_{dd} = \frac{DD(d_1, A)}{DD(d, A)} \qquad 5.10$$

where d_{bc} is the distance from the skin along the fanline for field size A, d_{fe} is the distance along the fanline between the dose calculation grid point and the plane perpendicular to the field central axis, where it intersects the body contour.

Corrections are done along fanlines from the grid point to the target, which include an inverse square law term: $\left(\frac{SSD + d_{bc}}{SSD + d_{fe}} \right)$ and the TAR/TPR term.

5.2.3 Inhomogeneity corrections

The CADPLAN makes use of two types of inhomogeneity corrections for beam modeling in patients. The first type is the generalized Batho power law (Sontag et al, 1977). This type of correction takes into account the radiation path length of the inhomogeneity in the patient, the field size of the photon beam and the position of the inhomogeneity in the patient. It does not take the shape or structure of the inhomogeneity into account and cannot correct for electronic equilibrium at the interface of the structure. This generalized correction factor can also take points within the inhomogeneity into account.

The other correction factor is the equivalent tissue-air ratio method (Sontag and Cunningham, 1978). This correction factor can take into account the radiation path length, field size and the position and shape of the structure. It also cannot correct for electronic equilibrium perturbation at the structure's interface. The only method capable of handling electronic disequilibrium is the Monte Carlo method. These inhomogeneity

correction factors have been discussed in detail in chapter 4. It is however instructive to give an overview of its implementation in the CADPLAN treatment planning system, since this links theoretical aspects to practical aspects regarding handling of discrete patient data in these correction theories.

5.2.3.1. Implementation of generalized Batho method in CADPLAN

The generalized Batho power law is suitable for use with CT data. CADPLAN uses CT slice data for its patient model. This slice data consists of matrices of linear attenuation data (CT numbers) which are converted to relative electron density data by means of a bilinear function relating the CT number to relative electron density. This relative electron density is defined as the ratio of electron densities for the tissue in a matrix element to that of water. In order to fit a bilinear function of relative electron density to CT numbers one must generate suitable data. This is done by scanning a phantom that contains several materials of known electron density on the CT scanner. Each material's relative electron density is then plotted against its CT number. A resulting bilinear trend is observed with a sharp line slope change for bone-like materials with CT numbers ranging from 100 to 2000 HU.

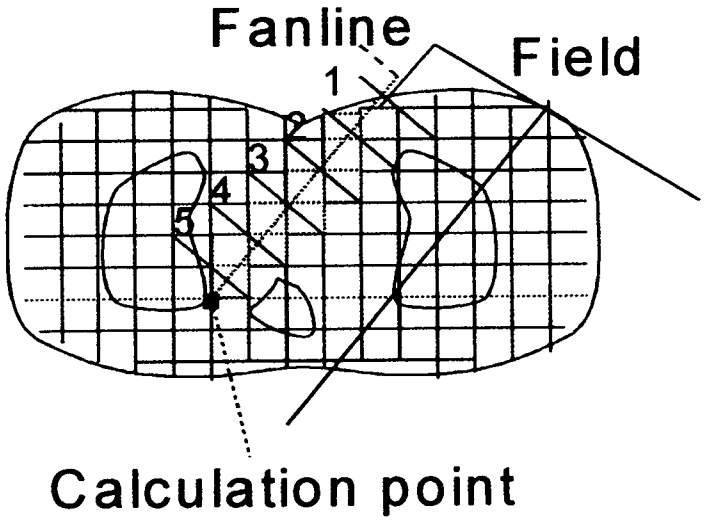

Figure 5.1 A patient slice showing a photon field incident from the right anterior oblique direction. A fanline is shown penetrating 5 layers before reaching the correction calculation point in the sixth layer.

The CADPLAN calculates the correction factor in a field using the following method: The correction factor is calculated along a fanline ranging from the calculation point to the focus point as shown in figure 5.1. The program tracks the inhomogeneity layers at 1 cm intervals and calculates the mean electron density for each layer. The correction factors are then multiplied together for each layer to obtain the total correction factor for the calculation point. The Fox and Webb equation is used to do this:

$$CF = K_N * \prod_{M-1}^{N} T(d_m, A)^{(\mu_m - \mu_{m-1})/\mu_0} \qquad 5.11$$

where T is the TAR value at depth d_m,

m is the index for inhomogeneity boundaries,

d_m is the distance from the calculation point to the Mth inhomogeneity layer,

A is the field size,

μ_m is the linear attenuation coefficient for the Mth inhomogeneity layer,

μ_0 is the linear attenuation coefficient for water.

K_N is the ratio of energy absorption coefficients for the Nth layer and water.

Equation 5.11 is also written in terms of relative electron densities as:

$$CF = K_N * \prod_{M=1}^{N} T(d_m, A)^{(\rho_e^w)_m - (\rho_e^w)_{m-1}} \qquad 5.12$$

$(\rho_e^w)_m$ is the mth material electron density relative to water.

In the CADPLAN application equation 5.12 is used, but the K_N factors are all defaulted to 1.

The TAR/TPR values are obtained through interpolation of a table containing this data for the calculation point.

5.2.3.2 Implementation of ETAR method into CADPLAN

The ETAR method is also suitable to use with relative electron densities and CT data. The main difference compared to the Batho method is that it can take the structure of the inhomogeneities into account and take a little longer to compute than the Batho method. The ETAR method is basically a ratio of tissue-air ratios and we can express the correction factor as:

$$C = \frac{TAR(d',r')_W}{TAR(d,r)_W} \qquad 5.13$$

The denominator expresses the TAR for a field size r at depth d in water. The numerator expresses the TAR at a scaled depth d' and field size r' in the heterogeneous medium. This scaling is performed according to the average relative electron density of all elements along the beam ray up to depth d. Thus if d is multiplied by this average electron density, d' is obtained. For the scaling of the field dimension r it becomes slightly more complicated. The relative electron densities (E_{ijk}) of the volume elements in the whole field are multiplied and divided by the product of each volume element's weight factor (W_{ijk}). These weight factors express each volume element's relative importance regarding scattered radiation dose contributions. Weight factors are defined in terms of scatter-air ratios (SAR's) (Cunningham, 1972). Sontag derived a function to obtain the field size scaling factor (E_r) through the equation:

$$E_r = \frac{\sum_i \sum_j \sum_k E_{ijk} W_{ijk}}{\sum_i \sum_j \sum_k W_{ijk}} \qquad 5.14$$

The weight factors must be calculated for each calculation point.

5.2.3.3 TPR, TAR and SAR

The CADPLAN makes use of the TAR, TPR and SAR in its inhomogeneity corrections. These data are derived from the input x-ray beam data and is stored in data files as matrices for different x-ray fields (rows) and depths (columns). The data is stored as TAR/TPR tables and SAR/SPR tables (SPR = scatter-phantom ratio). The TAR is typically used for low energy beams such as Co-60, while the TAR's is used for higher energy x-ray beams e.g. 8 MV x-rays. These values are calculated from measured depth dose curves for different x-ray fields on a 1 cm grid spacing for both parameters up to 40 x 40 cm x-ray field size to a range of depths from 0 to 40 cm. The same grid is used to calculate the SAR/SPR table from input depth dose data.

5.3 Other treatment planning algorithms

This section gives an overview of other dose calculation/optimization algorithms used in treatment planning systems. The CADPLAN uses measured x-ray beam data as obtained from water bath irradiation measurements. Its basic dose calculation algorithms have been described and it can be said that it calculates perturbations to the dose in water from input beam data in water due to different SSD's and skin obliquities. This geometrically corrected dose distribution in water is then multiplied by correction factors to take inhomogeneities into account to give the dose distribution in a CT based patient model. Other types of treatment planning algorithms use different approaches. One such approach is based on convolution methods, some use inverse planning techniques (Holmes and Mackie, 1994, Liu et al, 1993, Liu et al, 1999). The CADPLAN algorithm can be regarded as a correction based algorithm while convolution methods are known as model based algorithms.

5.3.1 Convolution methods

When a zero area (pencil) beam of particles such as x-rays are directed into a medium, say a water filled bath, a three dimensional (3D) dose distribution is obtained. This 3D dose distribution is generated from a very small x-ray field. If it is argued that any shape of x-ray field contains a set of such small field sizes, then it must be possible to reconstruct the total dose distribution for this arbitrary x-ray field by summing over all field elements. That is, the total dose distribution is obtained from the contribution of the 3D dose distributions of each field element. In technical terms the 3D dose distribution from a pencil beam is known as a dose kernel and the summation is performed via convolution with a suitable function such as one describing the x-ray fluence at the surface of the water.

In the 1980's a new concept for 3D dose calculations was developed with the aim to generalize high energy photon dose distributions for arbitrary field shapes and body contours. The idea was to generate so called scattering kernels or point spread functions for different photon energies. These kernels could then be convolved with the radiation field shape to obtain a 3D dose distribution. Ahnesjö et al, 1987, described a method of obtaining point spread functions for mono energetic photon beams between 0.1 - 20 MeV with Monte Carlo methods and it was used in some applications in a water phantom. Note that this type of correction method does not involve a calculation of a simple correction factor, since these kernels are derived from Monte Carlo simulation methods in mathematical water phantoms.

5.3.1.1 Terma and point spread function

When a photon beam is passing through a medium it releases energy. The terma is defined as the total energy released by primary photon interactions per unit mass. For a heterogeneous beam the terma is given as:

$$\mathbf{T(r)} = \int_0^{E\,max} \frac{\mu}{\rho}(\mathbf{E},\mathbf{r})\mathbf{E}\Phi_E(\mathbf{r})d\mathbf{E} \qquad 5.15$$

where μ/ρ is the mass attenuation coefficient for primary photon energy E and $\Phi_E(\mathbf{r})$ is the primary photon fluence differential in energy at **r**.

From eq. 5.15 the absorbed dose can be obtained if the energy transport of all secondary particles around each interaction point is known. In order to describe this a point spread function h(**r**) is necessary. This point spread function is defined as:

$$h(\mathbf{r}) = \frac{d\varepsilon(\mathbf{r})}{\mathbf{E}d^3\mathbf{r}} \qquad 5.16$$

Thus h(**r**) describes the fractional mean energy imparted in a small volume d^3r at **r** when a primary photon of energy E interacts at **r** = **0** (origin). This point spread function can as a first approximation be used to calculate the dose in another homogeneous medium with the same atomic composition but with a different density by a scaling procedure. In more general terms a spatial scaling factor c(**r**) is introduced for any kind of inhomogeneous media and is given as:

$$c(\mathbf{r}) = \frac{1}{\rho_0}\int_0^1 \rho(\alpha(\mathbf{r}))d\alpha \qquad 5.17$$

where α is a dimensionless linear scale ranging from 0 to 1.

This scaling factor gives the relative mean density along the line from the site of interaction (origin) to the energy deposition site at **r**. This scaling factor is used to modify the point spread function for use in other media with different densities as follows:

$$h(\mathbf{r}) = \frac{\rho(\mathbf{r})}{\rho_0}c^2(\mathbf{r})h_{\rho_0}(c(\mathbf{r})\mathbf{r}) \qquad 5.18$$

The absorbed dose can then be calculated from the point spread function and the terma at a field point r and a source point s, for energy imparted at r with the equation:

$$D(\mathbf{r}) = \iiint \int T_E(\mathbf{s}) h_{\rho_0}(E, \mathbf{r} - \mathbf{s}) d^3 s dE \qquad 5.19$$

This method of dose calculation can be performed with 3D fast Fourier transform (FFT) techniques. However this can only be applied for the case where the spatial distribution of h(r) is invariant, which is not the case for inhomogeneuos media since inhomogeneities "warp" the dose point kernel breaking its symmetric character which is only conserved in homogeneous media.

5.3.1.2 Generation of point spread functions

Point spread functions are generated with Monte Carlo simulations. A cylindrical phantom is constructed consisting of n layers of cylinders of thickness Δr which is subdivided into sectors at regular angular intervals to form voxels or volume elements. A beam of mono energetic photons impinges on the cylindrical homogeneous phantom at the origin parallel to the z-axis. Each photon history is followed and the total imparted energy distribution in the phantom is calculated. From the total number of primary photons and with the use of eq. 5.19 the point spread function can be constructed per primary photon of energy E.

Others (Mackie et al, 1988) also described methods for the generation of point spread functions with Monte Carlo simulation techniques. They noted that a heterogeneous photon beam can be modeled by constructing various homogeneous kernels and weighing it against the energy components of the spectrum.

These kernels are derived for point-like sources with ideal collimating conditions. In practice a radiation treatment machine such as a Co-60 or accelerator has a finite source size. This affects the generation of the beam penumbra which tends to be too narrow when convolution techniques are employed with conventional kernels. Low and

Hogstrom, 1994 described a method of measuring a photon penumbra-generating kernel for a convolution algorithm. A split photon field is scanned with conventional equipment to obtain a beam profile. The split-field profiles were differentiated to obtain strip integrals of the 2D kernel. These integrated kernels were smoothed and symmetrized after which the kernels were obtained from filtered back projection techniques. These kernels were used to generate penumbra data for photon fields in water and were compared with water bath measurements. Agreement of 1percent was achieved for 6 MV photons for field sizes of 5x5 to 20x20 cm^2 within the field boundary.

5.3.1.3 Improvements in point spread function-based dose distribution calculations

The accuracy of this technique was improved further by considering the spatial orientation of the pencil beam kernels in divergent photon beams.(Sharpe and Battista, 1993). In previous applications the kernels were incident perpendicular to the phantom surface and were not aligned according to the field divergence. Taking divergence into account improved the accuracy of dose computations near the field edges by up to 27 percent for a broad 10 MeV photon beam of 30x30 cm^2. This method was not tested in inhomogeneous media.

Kaell and Hoban, 1995, have incorporated the Fermi-Eyges electron scattering theory into primary dose calculation for external photon beam radiotherapy. The dose at point r is calculated by the formula:

$$D(\mathbf{r}) = \int_{r'} T(\mathbf{r}')\rho(\mathbf{r}')h(\mathbf{r}-\mathbf{r}', \rho_{ave})/\rho_{ave} d^3\mathbf{r} \qquad 5.20$$

where $T(\mathbf{r}')$ is the terma at point r', $h(\mathbf{r}-\mathbf{r}', \rho_{ave})$ is the dose point kernel or point spread function for an average density ρ_{ave}. The average density is derived indirectly from the Fermi-Eyges theory. This method was compared with the ETAR and Monte Carlo simulation methods and showed a better agreement with the Monte Carlo method. For a water-lung-water phantom the overall accuracy was better than 3 percent for the build-up

part of the second lung-water interface. The largest dose discrepancy was in the beginning of the lung region of 5 percent. The technique tends to overestimate the dose in the lung region and slightly underestimate the dose in the second build-up region when compared to Monte Carlo simulation methods.

Some authors (Wong et al, 1996) have adapted dose deposition kernels for 3D dose calculations in inhomogeneous media by using FFT techniques. Overall dose calculation accuracy of 3percent was achieved in simple heterogeneous phantoms.

5.3.1.4 Limitations of the pencil beam approach

Knoös et al, 1995, studied the limitations of a pencil beam model in low-density media such as the lungs. They demonstrated that the model could not account for changes in scatter from lateral heterogeneities. Measurements made in a water-cork phantom indicated that for Co-60 and 4 MV x-rays differences of 5 percent were observed in the mediastinal region between the lungs. For 18 MV x-rays the difference was as much as 18 percent. They concluded that the limitations of these pencil beam models correspond to that of conventional inhomogeneity correction models namely to account for changes in electronic equilibrium between adjacent media.

Pencil beam models can however be very useful when dose distributions are sought for irregular photon beams as used in conformal therapy. Recent refinements (Ostapiak et al, 1997) in pencil beam models by using finite-size pencil beams markedly improves the speed with which such dose distributions can be calculated.

5.3.2 Inverse treatment planning

The CADPLAN performs dose calculations for a set of x-ray beams in a CT based patient model. To obtain the optimal dose distribution in a target volume the planner at first would select the number and size of x-ray fields to irradiate the target volume. This selection would be based on his experience. If the target does not receive a high uniform

dose some of the fields are adjusted and the dose is recalculated. Inverse treatment planning techniques involve the computation of a number of modulated x-ray fields such that the tumor dose is achieved with the accompanying low dose to surrounding healthy tissue (Liu et al, 1993). Thus the dose to the target is prescribed first and then the number and configuration of the x-ray beams are determined to obtain that prescribed dose in the target.

The methods employed in inverse treatment planning involve some kind of optimization of an objective function (Liu et al. 1993, Holmes and Mackie. 1994) that is usually related to the prescribed dose and the actual calculated dose in the target. This is evaluated either on a regular dose grid or at randomly picked points (Holmes and Mackie, 1994)

One way of optimization is through the iterative approach (Liu et al, 1993). X-ray beams are modeled from energy distribution kernels or dose point kernels. The aim is to calculate energy fluence profiles corresponding to the optimal kernel density function. Liu and co-workers used the following function:

$$d(r) = \int_V h(r,r')f(r')d^3r' \qquad 5.21$$

where d(r) is the dose at point r, h(r,r') is an energy deposition kernel specifying the mean specific energy imparted to a volume element centered at r if the kernel is directed at a volume element at point r'. The kernel density function is denoted by f(r').

The aim of their inverse treatment planning technique involves solving eq. 5.21 for f(r'). By finding suitable kernel density functions the calculated dose in the target can be optimized against the prescribed target dose. The role of f(r') is to apply a weight to the energy imparted by kernel h. A complete two dimensional mapping of the kernel density would then describe the modulated x-ray beam. This is accomplished through a back projection technique of the kernel density function into the x-ray beam's kernel source points to obtain energy fluence profiles. Modern beam shaping such as dynamic multileaf

collimators, compensators and scanning x-ray beam techniques can be employed to reproduce the energy fluence profiles as determined.

Another technique of inverse treatment planning (Holmes and Mackie, 1999) is based on solving a set of linear equations of the form:

$$d = \mathbf{D}\omega \qquad 5.22$$

where d is a vector representing n samples of a 3D dose distribution, **D** is a square matrix representing the i-th fractional dose contribution to a particular dose sample in d from the j-th elemental dose distribution of weight ω_j. Just as in eq. 5.21 inverse treatment planning concerns itself with finding the optimal values for vector ω in order to optimize the sampled dose values in d. They made use of an objective function f as a quantitative measure of the closeness of fit for the prescribed and calculated dose values in d. This function f is related to the beam weights by expressing the weighing vector ω in terms of vector d. This can only be done if matrix **D** is invertable. $\mathbf{D}^{-1}$ is obtained by modeling the dose in say a 10x10x10 volume of sample points irradiated by 1000 pencil beams. The beam intensity is modulated also through a back projection method.

Liu et al, 1999 have taken inverse treatment planning a step further by speeding up x-ray beam intensity modulations through the use of x-ray beams as a whole. They made use of a theory based on the theory of variation with the aim of generating optimal intensity distributions for a set of static radiation fields. The equation used in their study has the form:

$$H = \frac{1}{2}\iint_{\Omega}\left(\sum_{i}^{m} D\left[d_i(x,y)\right] f_i\left[\tau_i(x,y) - P(x,y)\right]\right)^2 dxdy \qquad 5.23$$

Omega (Ω) is the integration volume where the dose is prescribed, P(x,y) is the prescribed dose, $D[d_i(x,y)]$ is a depth dose function and $f_i[\tau_i(x,y)]$ describes the dose contribution at point (x,y) from the i-th field and is also known as intensity distributions. H is an objective function that needs to be minimized by iterative calculations to find the

optimal set of intensity distributions. Their method only takes the number of x-ray beams into account making it much faster than methods that attempt to modulate dose point kernel intensities for each x-ray beam. Other recent improvements were introduced by Boyer et al, 1999. They developed a theory for calculating the setting of monitor units for fixed fields in intensity modulated radiotherapy with x-ray beam shaping multileave collimators. Beam modeling is achieved through the use of pencil beams and a convolution method. The accuracy of the calculated and measured dose delivered to the target was better than 4 percent in their study.

5.4 Summary

In this chapter the CADPLAN treatment planning system was discussed with regard to the various functions and input data to calculate dose distributions. This is performed in CT based patient models after the conversion of CT numbers to relative electron density. This was done to enable inhomogeneity corrections with the Batho and ETAR methods. The CADPLAN uses a correction based algorithm since it applies correction methods to the dose in water for an x-ray field in a patient model that also includes skin obliquity, depth dose and off-axis ratio corrections. Other types of treatment planning algorithms are of the beam modeling kind that includes convolution and inverse treatment planning. The convolution method makes use of dose point kernels as well as some of the inverse treatment planning algorithms. None of these algorithms makes use of input x-ray beam dose data e.g. water bath measurements as photon beams can be modulated to any shape and planar intensity with the use of dose kernels.

CHAPTER 6

Methods

6.1 The generation of phase space files for open and wedged beams for a generic linear accelerator

6.1.1 Introduction

The treatment planning system (TPS) that was evaluated uses correction based algorithms. Accelerator generated beam data must be supplied to it. This must be done to configure beam data for all accelerators for which treatment planning is to be carried out. This data is machine specific and therefore each accelerator's beam data must be collected from water bath measurements and entered separately. These beam data include percentage depth dose curves and dose profiles of a range of field sizes at a number of depths as measured in the water bath. The data must be collected for open and wedged beams. In this study Monte Carlo calculations of the absorbed dose distribution in CT based patient models were compared with those calculated by the treatment planning system, using the BATHO and ETAR inhomogeneity correction algorithms, for 8 MV x-ray beams.

Monte Carlo simulations require the energy, charge, directional and spatial distributions for all particle types (photons, positrons and electrons) in radiation beams. These parameters completely describe the beams. These beam characteristics cannot be extracted from water bath measurements. One solution is to model a generic accelerator. This was done by using the EGS4 based Monte Carlo (MC) code, BEAM. The main feature of this MC code is that it enables one to construct various types of generic accelerators and other radiation therapy machines by using component modules (CM's).

The particles emerging from the simulated generic accelerator are stored in a phase space file (PSF) and can be used as radiation sources for other BEAM applications. These PSF's contain all the necessary beam parameters.

The evaluation of the TPS calculated absorbed dose distributions proceeds as follows: In section 6.1 the procedure for the construction of an 8 MV generic accelerator, to obtain a master PSF below the ion chamber is shown. This PSF was then used in the second and third stage simulations of the accelerator to obtain the PSF's for a range of field sizes for open and wedged beams at an SSD of 100 cm. In section 6.2 the procedure for the calculation of the absorbed dose distributions in a water phantom from the previously generated PSF's with the DOSXYZ MC code is explained. Section 6.3 explains how these data were imported into the TPS. Absorbed dose calculations were then performed on the TPS using this beam data and were verified against the originally entered beam data. In section 6.4 a procedure to transform CT based patient models into discrete material data matrices for direct use in DOSXYZ is outlined. This data is then used directly in section 6.5 for the preparation and running of the DOSXYZ MC code to calculated 3D dose distributions in a *maxillary sinus*, *lung* and *prostate* patient model. In section 6.6 the procedure for the calculation of the corresponding dose distributions on the TPS is discussed. The comparison of these dose distributions is outlined in section 6.7

6.1.2 Construction of a Philips SL75/14 based generic accelerator

The simulated generic accelerator was based on a Philips SL75/14 accelerator (see figure 6.1). The beam simulation was done with the **BEAM97** MC code on a SOLARIS based 200 MHz Pentium Pro-S with two 6 GByte IDE hard disks and 128Mbyte of RAM. The simulation was done in three stages. The first stage involved the modeling and compilation (using the maximum possible optimization level) of the accelerator from the target down to the ionization chamber. Four CM's (SLABS, CONESTAK, FLATFILT & SLABS) were used to model the top part of the accelerator which housed 1) the heavy metal alloy brehmstrahlung target, 2) the primary collimator, 3) the flattening filter and

4) the ionization chamber. A phase space scoring plane was defined at the back of the ion chamber. An incident mono-energetic electron beam of 8 MeV generated a brehmstrahlung photon spectrum emerging from the heavy metal alloy (HMA) target. The number of histories used to generate these brehmstrahlung photons was 19 million. Brehmstrahlung splitting and the Russian Roulette option was used to increase the photon yield by a factor of 50 saving considerably on CPU time. The PSF that was generated at the scoring plane had a particle yield of 450 percent with respect to the number of primary histories run. The total disk space occupied by this PSF was in the order of 3 GByte containing the dynamic parameters of approximately 90 million photons. The simulation rate was in the order of 200 000 histories per hour.

During the second stage the accelerator was modeled from the previous scoring plane (below the ion chamber) to a second scoring plane at the isocenter which is below the X-ray jaws at a source-skin-distance (SSD) of 100 cm. The model consisted of an air gap, a set of 5 paired bars which formed the X-ray jaws, and an air gap extending from below the jaws to allow the collection of PSF's at the isocenter (100 cm SSD). The CM's used were SLABS, JAWS and SLABS respectively. The previously collected master PSF had now become the particle source for this stage. This time transportation was done through the lower part of the accelerator that housed the mirror and the jaws. Due to the fact that the mirror is composed of a very thin mylar-like sheet no significant perturbation of the beam was assumed and it was therefore not modeled. Range rejection was used by setting local values for the electron cutoff energy for particles entering the jaws. The energy cut-off for both photons and electrons were set at 8 MeV so as to only transport those particles that could clear the jaw aperture for each field size. This resulted in a simulation rate in the order of 40 million histories per hour. No brehmstrahlung splitting or photon forcing was used. PSF's were collected for square fields of side lengths 2, 3, 4, 5, 6, 8 and 10 cm. Each of these files was stored to be used as beam sources for the DOSXYZ MC code.

In the third stage the simulation was the same as stage two but included the geometry of a wedge filter that was created from the 'JAWS' CM. One of the jaw pairs was offset

such that its inner boundary was outside the beam of particles. The other jaw pair was tapered to form a wedge profile. This CM was inserted between the ion chamber and the jaws of the accelerator. The same sets of PSF's were generated as for the open beam cases to obtain PSF sources for the DOSXYZ simulation of wedged x-ray beams. No brehmstrahlung splitting or photon forcing was invoked.

The total number of histories for collecting a PSF for each of the open fields was set to 90 million and for the wedged fields to $1*10^9$. This was done to compensate for wedge attenuation. An added bonus is that the wedge alters most of the photons regarding the dynamic parameters (energy, position and direction) so that each one would be unique in the scored PSF's at 100 cm SSD despite the re-use of the master PSF.

6.1.2.1 Modeling the accelerator components

6.1.2.1.1 The bremsstrahlung target

The 'SLABS' CM was used for modeling the target. Its radius was set at 0.5 cm with a thickness of 0.32 cm. Thus the target was modeled as a square block with a side lenght of 1 cm and a thickness of 0.32 cm. It started at the z = -0.32 cm plane and extended to the z = 0 plane. It is constructed of heavy metal alloy (HMA) which consisted of an Iron (one percent)-Tungsten (95 percent)-Nickel (4 percent) alloy. The photon and electron energy cut-off values were set to 0.01 and 0.7 MeV respectively.

6.1.2.1.2 The primary collimator

The 'CONESTAK' CM was used for modeling the primary collimator. This CM extended from the z = 0.03 to the z = 11.95 cm plane. This collimator was made up of two layers consisting of 11 cm of Lead (96 percent)-Antimony (4 percent) alloy followed by 0.92 cm backing layer of HMA. The outer radius was set to 10 cm. An inner cone was constructed that acted as an air filled aperture through which the photons as generated in the target could travel in a collimated fashion. It had an upper radius of 0.25 cm and a

radius of 3.5 cm at the back of the HMA layer. The photon and electron energy cut-off was set to 0.01 and 0.7 MeV respectively.

6.1.2.1.3 The flattening filter

The 'FLATFILT' CM was used to model the HMA composed x-ray beam flattening filter. It extended from the z = 12.50 to the z = 14.093 cm plane. It has a simple conical shape of height 1.593 cm and a radius of 2.695 cm at the base. This is the real shape of the filter obtained from diagrams of a Philips SL75/14 accelerator. The photon and electron energy cut-off was the same as in the primary collimator case. The purpose of this filter is to flatten the sharply peaked photon fluence from the primary collimator through attenuation and scattering to make it more suitable for medical radiation purposes (i.e. to make the radiation fields flat).

6.1.2.1.4 The ion chamber

The 'SLABS' CM was used to model the ion chamber. It was composed out of three slab layers each with radii 6 cm. A layer of air with a thickness 1cm was sandwiched between two Mylar sheets of thickness 0.01 cm. It extended from the z = 15.5 to the z = 16.52 cm plane. At this plane the master PSF was scored. The photon and electron cut-off energies were the same as in the primary collimator case. This chamber collects an ion current that is related to the dose output of the accelerator as the x-ray beam passes through it causing ionization in the air. These four CM's comprised the first simulation stage of the accelerator.

6.1.2.1.5 The jaws

The jaws of the accelerator were modeled from the CM 'JAWS'. The accelerator jaws consist of 3 upper and 2 lower jaw pairs. The upper, or x-direction jaws consist of three layers. The first layer 6 cm of PbSb-alloy, the second is of 4 cm HMA and the third 0.3 cm of Al. The y- direction jaw pairs are identical in construction as the first two layers in

the x direction. For this CM the electron and photon cut-off energies were both set to 8 MeV. This allowed quite fast simulation times since it was not attempted to model transmission through these jaws. The purpose of these jaws is to define/adjust the dimensions (field sizes) of the emerging x-ray beams. This was modeled as part of the second stage of the accelerator. There is an air gap of 10.07 cm below the master PSF and the plane defining the top of the jaws. The jaws extended from the z = 10.08 to the z = 32.32 cm planes.

6.1.2.1.6 The wedge

The wedge model was based on the shape of wedge no. 2 of the SL75/14 linear accelerator. A profile of it is shown in figure 6.2. It is composed of a wedge shaped lead block mounted on a thin Al backing plate (not shown in the figure). The photon and electron energy cut-offs were set to values of 0.700 and 0.010 MeV respectively. A set of four paired bars was chosen in the x-direction. One of the jaw pairs (left side) were off-set to –10 cm in order to fall well outside the x-ray field. The wedge was modeled with the other pair (right-hand side). The length of the wedge was chosen as 25 cm by adjusting the outer boundary of the CM 'JAWS'. This CM was built as a new accelerator that used the master PSF as its beam source. The wedge was located at the z = 0.01 cm plane. It reached down to the z = 1.410 cm plane. The Al backing plate and air gap were modeled with the SLABS CM and extended down to the z = 10.07 cm plane. The Al backing plate had a thickness of 0.165 cm. Wedge filters are used to modify the photon fluence through attenuation. The effect is to modify the absorbed dose beam profile in the patient i.e. if a dose profile is flat in say a water bath measurement then it will have a gradient if a wedge is placed the X-ray beam. The thick side of the wedge will attenuate more x-rays and therefore the absorbed dose would be less than at the thin side of the wedge.

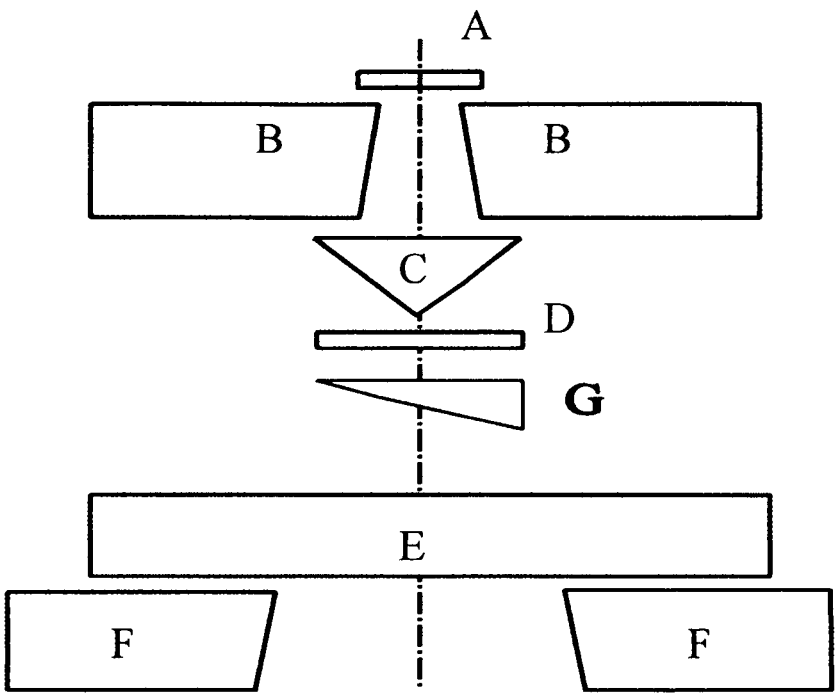

Figure 6.1 The model of the generic accelerator based on a Philips SL 75/14. The first stage of the simulation was done by transporting particles from the top of target (A) through the primary collimator (B) and flattening filter (C) to the bottom of the ionization chamber (D), where a PSF was scored. In the second simulation stage this PSF was used as a beam source and particles were transported through the lower part of the radiation head down to the isocenter. The third stage was identical to the second stage, except for the presence of the wedge (G)

The particles were transported for various settings of the jaw pairs (E and F) defining various field sizes. For each field size a PSF was scored. The third stage retained the same accelerator geometry as in stage two but with the inclusion of the wedge (G). PSF's were scored for these wedged beams for the same settings of the jaw pairs, i.e. with the same field sizes as for the open fields as in stage two.

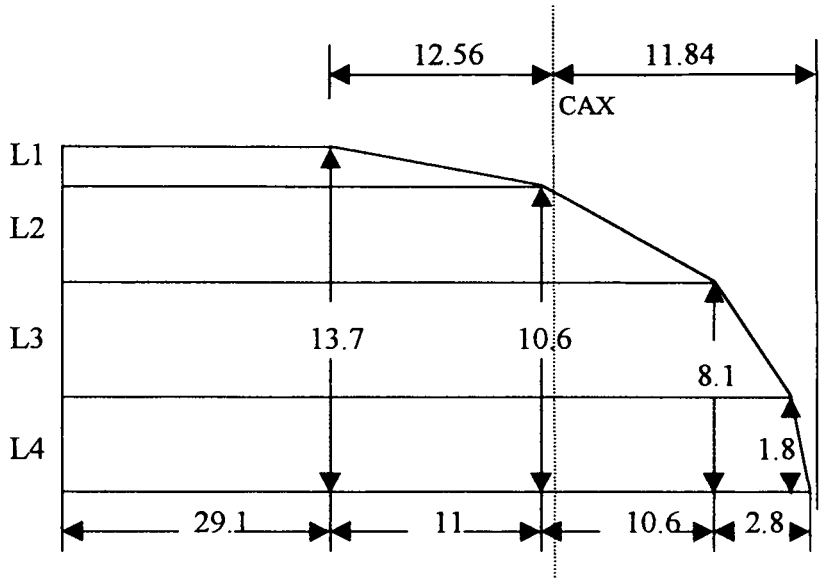

Figure 6.2 This figure shows the dimensions (NOT TO SCALE) of wedge no.2 (dimensions in mm) as used in the simulation of wedged beams in the third stage. The wedge is made of lead and CM 'JAWS' was used to model it. It consisted of four bars (L1,L2,L3 and L4) in the x-direction. The other bars in each of the pairs were off-set to –10 cm so that it was out of the particle beam. The outer boundary of this CM was set to 25 cm. The 1.650 mm Al backing plate is not shown in this figure. The central beam axis (CAX) is shown by the dotted line.

6.1.2.2 Variance reduction

The only CM that had the transport cut-off energies of the electrons and photons set to a high level (8 MeV), was the jaws of the accelerator. The transport cut-off energies in all the other CM's were set to 0.700 (ECUT) and 0.010 MeV for electrons and photons respectively. The **700icru** PEGS4 data file was used for cross section data. This decreases the simulation time since the electron transport is terminated and all its residual kinetic energy deposited locally when the electron has a kinetic energy of equal to or less than 189 keV.

The ESTEPE parameter was set to zero thereby invoking the PRESTA algorithm. Since the dimensions of the accelerator components are much larger than the average step length of the electrons, the use of PRESTA will decrease the simulation time. This is

because of its boundary crossing algorithm that allows electron transport in larger steps when 'far' from a CM boundary allowing it to deposit more energy than instead of smaller electron step sizes by setting ESTEPE (*fractional energy loss per step*) say at 1 percent or smaller.

The accelerator was simulated in three stages. The first stage took the longest time. The purpose was to generate a 'master' PSF just below the ion chamber. This file was re-used for the second and third simulation stages. This decreased the simulation time drastically because the full simulation of the upper part of the radiation head did not have to be repeated for each field size.

Range rejection was used in all three stages. It was set to 1. This meant that an electron transport simulation was terminated if its energy were below a calculated value. This value is such that if the electron could reach the bottom of the accelerator, its energy must be value larger than ECUT. The maximum energy at which this was considered was set at 0.8 MeV. This value was chosen to reduce possible transport approximations so that low energy bremsstrahlung photons could be included in the PSF at the bottom of the accelerator.

6.1.3 Cross section data for HMA and PbSb

The EGS4 based MC codes BEAM and DOSXYZ use cross section data generated by the preprocessor code PEGS4. The BEAM97 package includes data files containing the interaction cross sections of an extensive list of materials. The supplied cross section data files are called **521icru.pegs4dat** and **700icru.pegs4dat**, and contains data for electron cut-off kinetic energies of 0.01 and 0.189 MeV respectively. These files had to be extended to include cross section data for the metal alloys HMA and PbSb found in our generic accelerator. The PEGS4 preprocessor code was supplied with a suitable input file to generate this data. The physical parameters for the alloys are summarized in table 6.1.

Mixture:	WNiFe (HMA)	PbSb
Density: (g/cm3)	18.34	11.34
Percentage mass ratio:	95:3.5:1.5	96:4

Table 6.1 Lists the physical parameters for the heavy HMA- and PbSb alloys. These parameters were supplied to the PEGS4 preprocessor to generate cross section data.

The lower electron and photon energy bounds were set to: AE = 0.700 and AP = 0.01 MeV. The upper energy bounds were set to UE = 55.511 and UP = 55.0 MeV. The alloys were defined as mixtures (MIXT). The APRIM (*empirical correction factor in brehmstrahlung cross section*) option was set to a value of one (switched on). A piecewise linear fit (PWLF) option was chosen for interpolating between tabulated energy values for the appropriate cross section data together with the DECK option. IUNRTS was set to zero to use the restricted stopping power.

6.2 The calculation of the absorbed dose in a water phantom using DOSXYZ

Beam data are needed as input for the TPS. The treatment planning system must be supplied with the percentage depth dose and beam profiles for a range of square field sizes in order to construct its beam models. This data was obtained for the generic accelerator by calculating the absorbed dose in a water phantom using the DOSXYZ code. The generated PSF's for the open and wedged fields as described in section 6.1 were used as the beam sources. The beam data was extracted by writing suitable programs to read the output 3D dose files of the DOSXYZ simulations. The TPS uses a 5 mm grid spacing for the input data. This grid spacing was consequently also used in the DOSXYZ simulation.

6.2.1 The Construction of the water phantom

The water phantom was constructed with a dimension of 29.5x29.5x30.25 cm^3. The isocenter was chosen on the surface at z = 0, in the center of the horizontal xy-plane. The number of voxels in the x and y direction was set to 59 each to allow the center voxel in the xy plane to be centered on the central axis (z-axis). The voxel dimension was set at 0.5 cm (matching the TPS dose calculation grid) in the x and y directions. In the z-direction the first voxel had a dimension of 0.25 cm to allow calculation of the 'surface' dose. The rest of the voxels (60) had a dimension of 0.5 cm. The source was aligned with the isocenter with the beam direction parallel to the z-axis. This allowed depth dose values to be calculated in the central voxels in the z-direction. The boundaries of the phantom were set at $-14.75 \leq x \leq 14.75$, $-14.75 \leq y \leq 14.75$ and $0 \leq z \leq 30.25$ cm.

6.2.2 Transport control parameters

The photon and electron energy cut-off was set at 0.010 and 0.700 MeV respectively and the **700icru** PEGS4 data file was used for the supply of cross section data for water. The PRESTA algorithm was invoked because that has proved to increase the history simulation rate quite effectively. The source type was full PSF input data with the ISMOOTH option invoked for the reuse of open field PSF data only. The number of histories was chosen so as to reduce the percentage error to less than one percent in all voxels in a field. The number of histories was chosen as 400 million for a 2x2 cm^2 field up to $2*10^9$ for a 10x10 cm^2 field. The history simulation rate was in the order of $7.5*10^6$ histories per hour. No attempt was made to raise the electron energy cut-off, in order to avoid possible artifacts, though tests have shown that it could effectively reduce simulation times.

6.2.2 Data analysis

The output of DOSXYZ consists of a 3D dose array. This is a text file that can be read and manipulated by writing suitable routines. A Fortran program was written to

normalize the dose to the dose maximum in the array and to express it in terms of percentage dose. The percentage depth dose data were extracted from the voxel array centered on the central beam axis (z-direction). Five beam profiles were extracted at depths of the dose maximum (d_{max}), 5, 10, 15 and 25 cm in the x-direction. This data was extracted for open and wedged fields and was converted into a suitable input file for direct import into the TPS. This input format depends on the type of treatment planning system used.

6.3 The verification of the input beam data for the TPS

The beam data of the generic accelerator was imported directly into the TPS. This beam data could then be used to calculate dose distributions in patient models to simulate treatment on this Monte Carlo generated 'generic' accelerator. Before actual patient dose distribution calculations were carried out a set of quality control tests were carried out. The aim of these tests was to validate the calculated dose profiles in water with the beam data that was originally imported into the TPS.

6.3.1 Water phantom dose calculations

After the beam data was configured a water phantom with a relative electron density equal to one was constructed on the TPS. In the TPS the electron density of any material is always expressed relative to the electron density of water. The conversion of the electron density phantoms or CT based patient models to this format is needed for the application of the BATHO and ETAR inhomogeneity correction algorithms. No inhomogeneity correction was needed for the water phantom dose calculations. The validation required that the dose distributions calculated in the water phantom by the TPS had to be the same as the original water phantom data generated with DOSXYZ. Dose distributions were calculated in this phantom for 2x2, 5x5 and 10x10 cm^2 fields. This was done for the open and the wedged beam cases. The data consisted of central axis percentage depth dose curves, and five beam profiles at depths of d_{max}, 5, 10, 15 and 25

cm depth. After validation of the comparative beam data, the TPS could be used to calculate dose distributions in CT based patient models with this generic SL75/14 accelerator.

6.4 The transformation of CT based patient models into a format suitable for DOSXYZ

Input beam data for patient models usually consist of a set of CT slices with the patient information expressed in terms of CT numbers. These CT numbers are converted to relative electron densities by the TPS for use in its dose calculation algorithms. For a patient model to be used in the DOSXYZ code, each of its volume elements (voxels) have to be associated with a specific material entry in a PEGS4 data file with a specific material name and physical density. The PEGS4 data file must contain the relevant cross section data for each material in the patient model. A problem that arises is that it is impossible to associate CT numbers uniquely with tissues of a known atomic composition and density in order to generate the relevant cross section data for each tissue. It is possible however to associate CT numbers indirectly with various tissues through their relative electron densities. The relation between CT number and relative electron density is found to be a bilinear function. Thus it is possible to associate a specific CT number with a specific relative electron density and in turn to associate this relative electron density with a group of materials with the same electron densities. For 8 MV x-ray beams the Compton interaction represents about 98 percent of all interactions. Thus at these megavoltage energies, materials with the same electron densities will behave dosimetrically equivalent.

The conversion of CT numbers to represent material types was performed according to the method of Du Plessis et al, 1998. A question that comes to mind is whether a material such as water could be used to characterize all the tissue types by suitably altering its physical density so that its electron density, and therefore CT number, matches that of any desired material. If only electron density dependent interactions occurred in materials then this would be feasible. However the photoelectric and pair production interactions

are dependent on the atomic number or atomic composition of the material. Thus, by simply adjusting the physical density of water to, say, that of thyroid, would account for the Compton interactions correctly but, since the effective atomic numbers of water and thyroid differ, the effect on the dose due to pair production is not immediately evident. These effects were not investigated in this study and therefore it was decided to use the approach depicted by table. 7.1

Monte Carlo codes allow for density scaling and the above procedure could be simplified considerably e.g. by reducing the number of generated PEGS4 materials from 57 down to 8 (one material out of each group in table 7.1 plus air). The DOSXYZ code allows for the adjustment of the physical density of each material in its patient model. This would allow replacing the histogram mechanism of associating CT numbers with material types by a ramp function that allows for continuous CT number to material conversion. This would yield a more accurate patient model. However, the bin widths in our study already limit the uncertainties in the dose calculations to less than one percent.

The histogram approach was used since the bin widths for soft tissues were only twice that of the noise expected in the CT numbers for soft tissues. This noise is in the order of 10 – 15 HU. It was found that the CT bin widths for lung and soft tissue were 30 HU. In the method of Du Plessis et al, the CT numbers in a bin were set to the median CT number for that bin, thereby averaging out to some extent the noise from the CT scanner. The ramp method would convert CT numbers and assingn it to densities that inherets the noise on the CT data.

The main point here is that appropriate density scaling of a few materials such as found in table 7.1 could be used to convert CT numbers to material types. Reducing the need for a large PEGS4 material data base.

6.4.1 Determination of dosimetrically equivalent tissue types

The classification of various tissue types according to their equivalence in depth dose was done by utilizing Monte Carlo dose distribution calculations in cylindrical phantoms. In this study the CYLTRAN option of the ITS3 code was used. The phantoms were constructed as cylinders with radii of 10 cm and heights of 20 cm with the radiation beam directed at one of the end faces. The phantoms were subdivided into radial annuli of 2mm between 0 and 4 cm radius and 1 cm annuli beyond 4 cm radius. In the length of the phantoms the subdivision was in 2 mm thickness increments between 0 and 4 cm from the beam entry surface and 1 cm increment thickness beyond 4 cm. These phantoms were homogenous and each one was composed of a different tissue type. Sixteen different tissue types (including water) were used and their atomic compositions and physical densities were set up according to ICRU44. These tissues are listed in table 1. Of these tissues lung and hard bone were further subdivided into a range of physical densities. A pencil beam of 8 MV photons was directed parallel to the central axis, perpendicular to the circular end surface. This 8 MV photon beam was modeled in the CYLTRAN input file as a cumulative energy spectrum. These spectral data were obtained by running the BEAMDP code to analyze the 'master' PSF that was generated previously according to section 6.1.2. The energy spectrum so obtained contained 16 bins with a width 0.5 MeV to span an energy range between 0 and 8 MeV.

One million photon histories were simulated to score a pencil beam kernel in each phantom. The depth dose curves were obtained for 100 cm^2 circular fields by utilizing the reciprocity theorem in combination with the cylindrical symmetry of the phantoms (Nelson et al, 1988). These variance reduction techniques reduced simulation times to 30 min on a 200MHz Pentium Pro-S per phantom. The dose along the central axis had statistical uncertainties of less than one percent.

The depth dose curves were normalized to the global maximum found for all tissues and were smoothed with second order polynomials to reduce the statistical noise in the data. The polynomial fits were performed for the phantom thickness range (R), $d_{max} \leq R \leq 20$

cm. The correlation was better that 0.99 in all cases. These smoothed percentage depth dose curves were subtracted from that of water. The resulting curves were plotted as a function of phantom thickness. From this it was possible to group different tissues that had a dose difference variation of less than one percent into dosimetrically equivalent tissue subsets.

6.4.2 Derivation of CT number intervals

The electron densities of all the tissue types studied here are reported in ICRU 44 (see table 7.1). Using these values the range of electronic densities in each subset was determined. The relation between CT number and relative electron density was obtained in the next step. This was accomplished by scanning a RMI CT density phantom (Gammex RMI, Middleton, WI) in a Siemens Somatom HiQ-S CT scanner. This CT density phantom contains inserts of different tissue equivalent materials (from adipose to cortical bone) with known electronic densities. After each insert's average CT number was obtained it was plotted as a function of relative electron density. A bilinear function was obtained giving a one-to-one relation between CT number and relative electron density. The range of CT numbers associated with the range of electron densities of each of the dosimetrically equivalent tissue types could then be established.

The depth dose data for the soft tissues were analyzed at various depths (or phantom thickness) namely at 5, 10 15 and 20 cm. At each depth each soft tissue's percentage depth dose was subtracted from that of adipose tissue, the latter being the soft tissue with the lowest CT number in this group of tissues. This percentage difference was plotted against each tissue's CT number. This procedure was repeated for the lung and hard (cortical) bone tissue subsets respectively. From the inverse slopes of the lines fitted to the percentage dose difference against CT number a relation was found giving the maximum possible range of CT numbers that would yield a dose difference less than one percent. Mathematically the line equations is formulated by:

$$D = m^* CT + c \qquad 6.1$$

Where D is the dose difference with respect to the dose of the material with the lowest CT number like adipose for the soft tissues. CT is the CT number for the material. The constants m and c are determined from fitting procedures like regression analysis. If the maximum CT number range is to be determined for which the dose variation (δD) must not exceed one percent then eq. 6.1 is written as:

$$\delta D = m * \delta CT \qquad 6.2$$

If δD = 1 is inserted into eq. 6.2 then it follows that the CT number interval (δCT) is equal to the inverse slope, m, of the fitted line.

6.4.3 Conversion of CT numbers to material types and setting up PEGS4 input data

A FORTRAN program was written to convert the continuous range of CT numbers in images into images where the CT numbers are binned into discrete CT intervals as determined for lung, soft tissue and bone. Each interval was associated with a specific tissue type and was given the numerical label of the interval. A PEGS4 data file was set up that contained the relevant information for each of these materials and was called – **tissue700icru**. This file contained 57 different tissue types, with the lowest density of lung labeled as material 1 and the densest cortical bone labeled material 56. Air was labeled as material 57.

The input data for the PEGS4 program consisted of 31 different densities of lung, 21 different densities of cortical (hard) bone and 5 soft tissue types. The physical material related parameters for these tissues are shown in table 7.2

The lower electron and photon energy bounds were set at AE = 0.700 and AP = 0.01 MeV. The upper energy bounds were set at UE = 55.511 and UP = 55.0 MeV. The tissues were defined as mixtures (MIXT). The APRIM (*empirical correction factor in*

brehmstrahlung cross section) option was set to a value of one. A piecewise linear fit (PWLF) option was chosen together with the DECK option.

6.5 Preparing and running DOSXYZ with compatible patient models for absorbed dose calculations

In section 6.4 a method was described to transform CT based patient models containing only CT numbers into a format suitable for use by DOSXYZ. The current section describes how these patient models were imported into DOSXYZ input files so that the absorbed dose could be calculated on these patient models with MC methods.

6.5.1 Patient models

Three particular patient geometries were chosen. The *first* one was a *maxillary sinus*. This model was chosen because of the complex geometrical distribution of air and bone structures. This type of tissue configuration is ideal to test the correction based dose calculation algorithms since a variety of tissue inhomogeneities occur. The density difference of adjacent tissues is also quite large and the electronic equilibrium disruptive effects could be tested in these regions. It is known that the ETAR and BATHO methods cannot account for the loss of electronic equilibrium in such tissue configurations. The *second* chosen patient model contained *lung* tissue. Again this was chosen because lung tissue have densities lower than water equivalent tissue types like muscle and is representative of a large tissue inhomogeneity. The *third* patient model chosen was that of a pelvis containing the *prostate* gland. In this model some air cavities may be present due to the intestines. Most of the tissues present in this model will have relative physical densities higher than that of water by a few percent.

For treatment planning purposes in our institution CT data is transferred via a network connection to the TPS. Each CT slice is stored in the CADPLAN system in CART image format, which is a direct-access binary file. There are 256x256 pixels per slice. The pixel size and the z co-ordinate can be extracted from these files. These CT files were

transferred from the TPS via a local area network to a LINUX based 333MHz Intel Pentium PC with 10Gbyte of disk space and 128Mbyte of memory (RAM). A FORTRAN program was written to swap the bytes in these binary files. This was done because the CADPLAN system, which is a Hewlett Packard workstation, has a MOTOROLA based microprocessor and the PC has an INTEL based microprocessor. Data is stored in 'big-endian' format on the HP workstation and in 'little-endian' format on the PC (Kirkby and Delphi, 1997).

After byte swapping, the CART files could then be analyzed. The CART files are composed of 269 records with length of 512 bytes. Record one is an administrative block and records 2 to 13 are user blocks. Records 14 to 269 contain the CT image data stored as 2 byte integer data, with the CT numbers represented as [Hounsfield number] + 1000 (CADPLAN, 1995). The CT images (records 14 – 269) were stored in separate direct access binary files on the PC.

These CT images were transformed to discrete material images according to section 6.4.3.

6.5.2 Setting up the DOSXYZ input file

The transformed images were evaluated slice by slice in the z-direction with the WINDOWS based image processing program OSIRIS. This program is able to display images stored in direct-access binary files. From these images a series of 12 adjacent slices of thickness 1 cm were selected as the DOSXYZ patient model. A FORTRAN program was written to convert these binary files to sequential access text format and to combine them into a single file. This file contained the necessary information to construct the patient model for DOSXYZ. The z co-ordinate of the radiation beam central axis was chosen to lie midway between slices 6 and 7. The x and y beam entrance co-ordinates were obtained from the image data for the 6^{th} slice.

Another FORTRAN program was written to create the DOSXYZ input file. This had to be done since the input file must contain the x,y and z indices for each voxel in the patient model as well as the PEGS4 name and physical density of the material in each voxel. (Consider that each slice has 256x256 pixels and that there are 12 slices, this leads to an input file tens of Mbytes in magnitude). The slice thickness was 1 cm except for the first and last slices in the patient model that were set to a thickness of 5 cm.

This procedure was performed for all three patient models. The pixel sizes were the same in both the x and y directions and were 1.01 mm for the maxillary sinus, 1.96 mm for the lung and 1.667 mm for the prostate cases. Thus the DOSXYZ patient models were scaled to life size.

6.5.3 DOSXYZ absorbed dose simulations

After the patient models were imported into the DOSXYZ input file the beam direction and entrance co-ordinates were verified. This was done by simulating 100 million histories to obtain a 'premature' dose distribution. A FORTRAN program was written to extract the absorbed dose distribution in the 6^{th} slice from the DOSXYZ output file. This dose distribution is representative of the xy-plane at the z co-ordinate of the central beam axis. The dose values were normalized to and stored as a direct-access binary file containing 256 records each of length 512 bytes. This file could be displayed as an image of the dose distribution with the OSIRIS program. This image was compared with the 6^{th} slice of the patient image to evaluate the beam entrance co-ordinates and direction in the patient. After this evaluation had shown that the PSF beam source was located and directed correctly, the DOSXYZ simulations to calculate the absorbed dose distributions in the patient model were started.

6.5.4 Transport control parameters

6.5.4.1 Open fields

The photon and electron energy cut-off were set at 0.010 and 0.700 MeV respectively and the **tissue700icru** PEGS4 data file was used for the supply of cross section data for the 57 material types in the patient model. The PRESTA algorithm was invoked. The source type was full PSF input data with the ISMOOTH option invoked for the re-use of open field PSF data. The number of histories was chosen such as to reduce the statistical uncertainty to less than one percent standard deviation in all voxels in a field. The number of histories varied between $6*10^8$ for a 2x2 cm^2 field up to $3*10^9$ for a 10x10 cm^2 field. The history simulation rate was in the order of $8.5*10^6$ histories per hour for the maxillary sinus case. There was a slight increase in the simulation rates for the lung and prostate cases due to the fact that these patient models had larger voxel sizes that made the PRESTA algorithm faster. No attempt was made to increase the electron energy cut-off values. This was done to avoid possible artifacts. Tests have shown that it could effectively reduce simulation times if the electron energy cut-off values were set to higher values e.g. 1 MeV but it could result in dose artifacts. The simulations were performed with the **BEAM98** package installed on two LINUX based 333MHz Intel Pentium systems. Each one had a total disk space of 10 GByte with 128 MByte RAM.

6.5.4.2 Wedged fields

For the evaluation of wedged field dose distributions the *maxillary sinus* patient model was chosen. The dose distribution of two perpendicular 5x5 cm^2 wedged beams was calculated. The DOSXYZ calculations were done for each field separately and the resulting .3ddose output files were added to obtain the net absorbed dose distribution. These .3ddose output files contain the absorbed dose values for each voxel in the patient model as well as the uncertainties expressed as percentage values for the corresponding dose values. These files are sequentially written text files. The number of histories was set to $1.8*10^9$ per field. The PRESTA, ECUT and PCUT values were the same as those

in section 6.5.4.1 .The ISMOOTH option was disabled so that the phase space particles would not be redistributed, since this would destroy the wedged fluence of the beam.

6.6 The calculation of the absorbed dose on the TPS

The absorbed dose distributions calculated by the BEAM98 version of the DOSXYZ code was compared with the dose distributions calculated by the treatment planning system. To conform to the MC patient models, the original CT based patient models (*maxillary sinus, lung and prostate*) were also binned into 57 discrete CT number intervals on the TPS. Each interval spanned a CT number range of 30 HU for soft tissues up to CT numbers of 1100. For CT numbers > 1100 all the CT numbers were binned into CT number intervals of 100 HU (Du Plessis et al, 1998). All the CT numbers in a bin were set to the median CT number for that bin. Thus the original CT data were discretized to 57 CT numbers. These CT data corresponded to the patient models for DOSXYZ but instead of the material labels required by DOSXYZ, there were now 57 CT numbers in the patient model. This procedure was performed to eliminate any differences between the dose distributions calculated with the TPS and MC that could possibly arise due to the discrete CT number structure of the MC input data.

6.6.1 Absorbed dose calculations

The treatment planning was performed using the entered 'generic' accelerator beam data as described in sections 6.2 and 6.3. The absorbed dose distributions were calculated for the three treatment cases for the 2x2 cm, 5x5 cm and 10x10 cm^2 open x-ray beam, field sizes. The *maxillary sinus* patient model was used to calculate the dose distribution for two perpendicular 5x5 cm^2 wedged beams. The beam directions and entrance co-ordinates were the same as for the DOSXYZ dose calculations. The absorbed dose was calculated for both the ETAR and BATHO inhomogeneity correction methods in the 6^{th} slice of each patient model. This slice corresponds to the same slice number as the central beam axis co-ordinate for the DOSXYZ dose calculations. These data were stored in 2D dose calculation matrices with a grid spacing of 2.5 mm. These dose matrices have a

dimension of 160 records each of length 112x2 bytes. These files were transferred to a LINUX based PC and byte swapping was performed. Corresponding dose distributions in a water phantom were also calculated on the TPS for the same open and wedged field configurations. No inhomogeneity corrections were invoked in this step. These were needed for normalization purposes as explained later in the next section. The resulting 2D dose matrices were also transferred to the PC.

6.7 Comparison of DOSXYZ and TPS calculated dose distributions

6.7.1 Normalization of the dose distribution calculated with DOSXYZ

The methods for the calculation of dose distributions with the DOSXYZ code and the TPS were given in sections 6.1 to 6.6. The next step was to compare these calculated dose distributions. The comparison of these absorbed dose distributions requires that the normalization method in both cases be the same. The TPS normalizes the dose distribution of each field to the value of the dose obtained at the central axis maximum position for the same field in water (CADPLAN, 1995). This would be at a depth of 2 cm for a 10x10 cm^2 field for the 8 MV beam.

To make a meaningful comparison of the Monte Carlo and TPS dose distributions, it was necessary to normalize the Monte Carlo dose distributions in patient models in a similar way. The resulting distribution could then be compared to the TPS's calculated dose distribution. This comparison relies on the assumption that the normalized absorbed dose distributions in water calculated by the TPS and DOSXYZ differ only marginally. This assumption was actually tested by comparing the normalized absorbed dose distributions in water obtained from the CADPLAN and DOSXYZ. It was found that the agreement between these absorbed dose distributions were within one percent.

CHAPTER 7

Results

7.1 Introduction

In the previous chapter the methods used for the evaluation of a treatment planning system dose calculation algorithms with MC methods were described. This chapter gives an account of the results that were obtained by these methods.

7.1.1 PSF's for open and wedged beams

A master phase space file (PSF) was collected during the first simulation stage of the generic accelerator. The particle data in this file were analyzed with the BEAMDP code. The spatial photon fluence and energy (spectral) distributions for the photons are shown in figures 7.1 and 7.2.

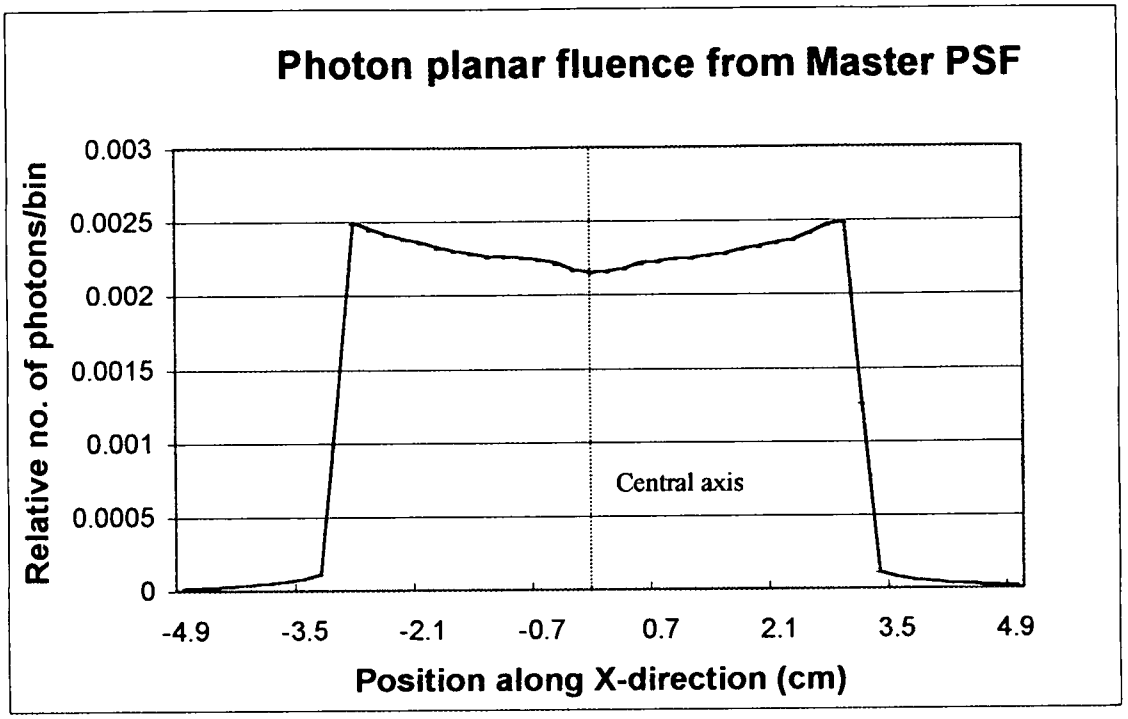

Figure 7.1 The photon fluence distribution in the x-direction in the plane of the 'master' PSF. A total of 50 bins were chosen with a width of 2 mm in the x-direction. The error bars are seen to be small in comparison with the energy fluence.

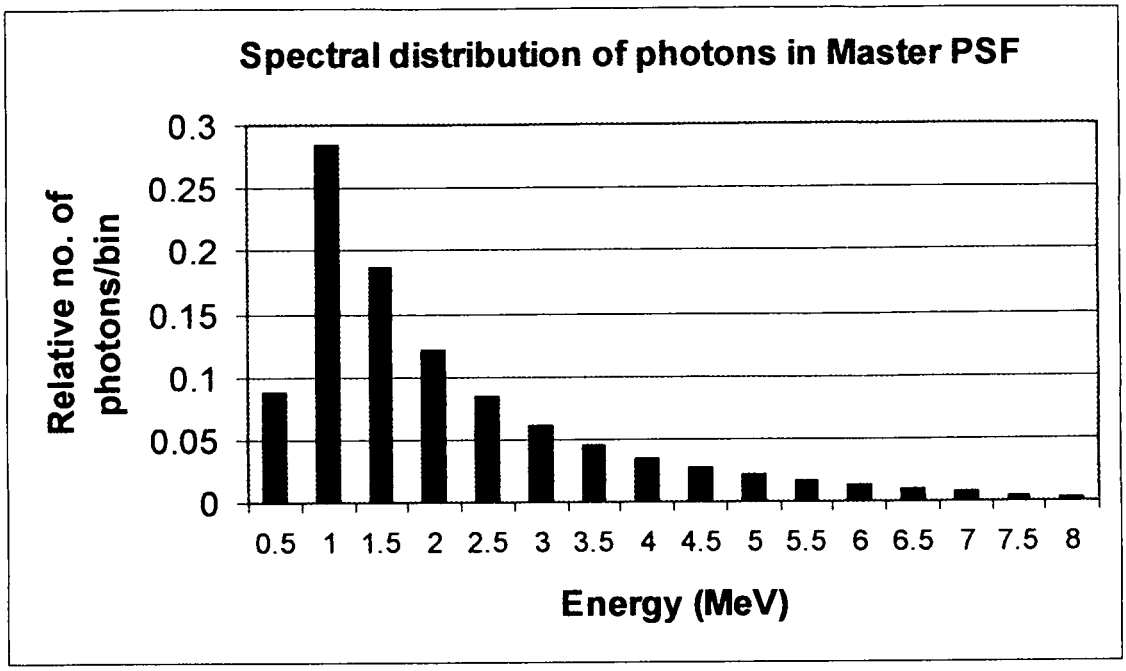

Figure 7.2 The energy spectrum for the photons with the planar fluence as shown in figure 7.1. This is the energy spectrum for photons produced in the brehmstrahlung target and scattered in the flattening filter of the generic accelerator as scored in the master PSF. The error bars are very small compared to the magnitude of the spectral energy distribution values and are not visible.

For the spectral data a rectangular region of 10x10 cm^2 was chosen to include the total PSF area. The energy bin width was chosen as 0.5 MeV. The energy labels are taken as the median energy in the range that each bins spans. E.g. the first bin ranges from 0 to 0.5 MeV with a label indicating 0.25 MeV.

This 'master' PSF was used to generate various other PSF's for open and wedged beams at an SSD of 100 cm for various square field sizes. These generated PSF's were used as sources in the DOSXYZ code for the purpose of calculating the input beam data for the treatment planning system. Figures 7.3 and 7.4 show examples of 5x5 cm^2 open and wedged photon energy fluence profiles.

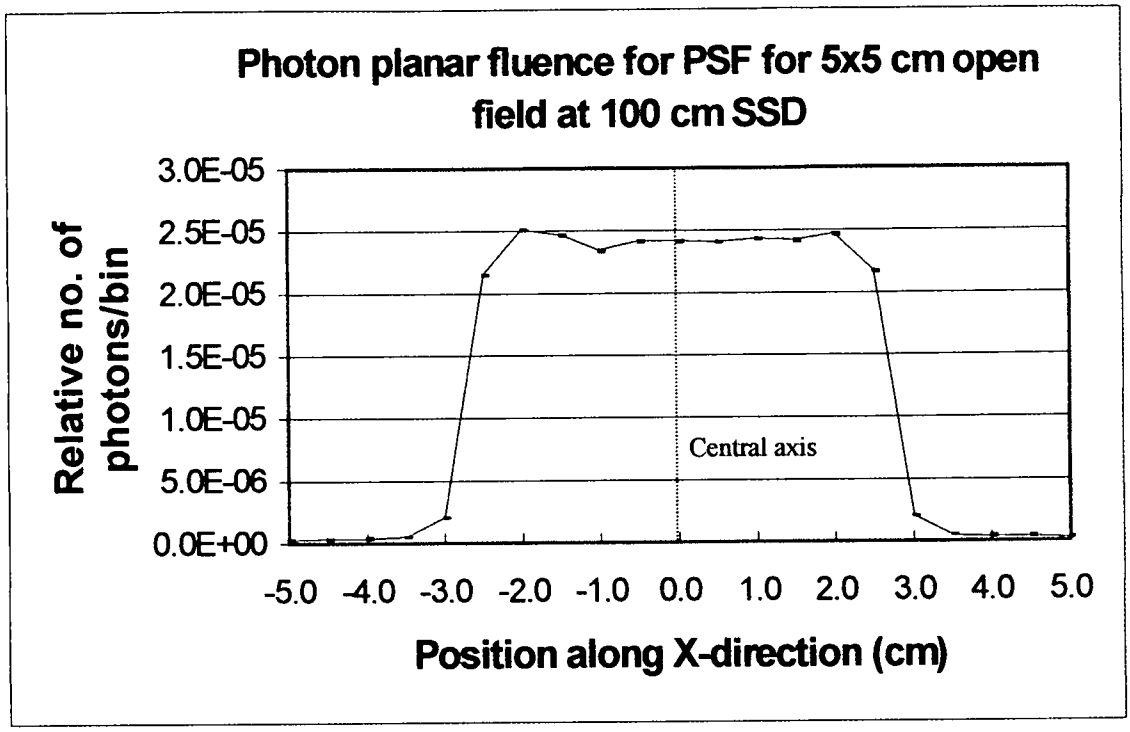

Figure 7.3 The photon planar fluence at 100 cm SSD for a 5x5 cm square open field. The statistical uncertainties are within one percent. A total of 20 bins of width 5 mm each were chosen to set up the energy fluence profile.

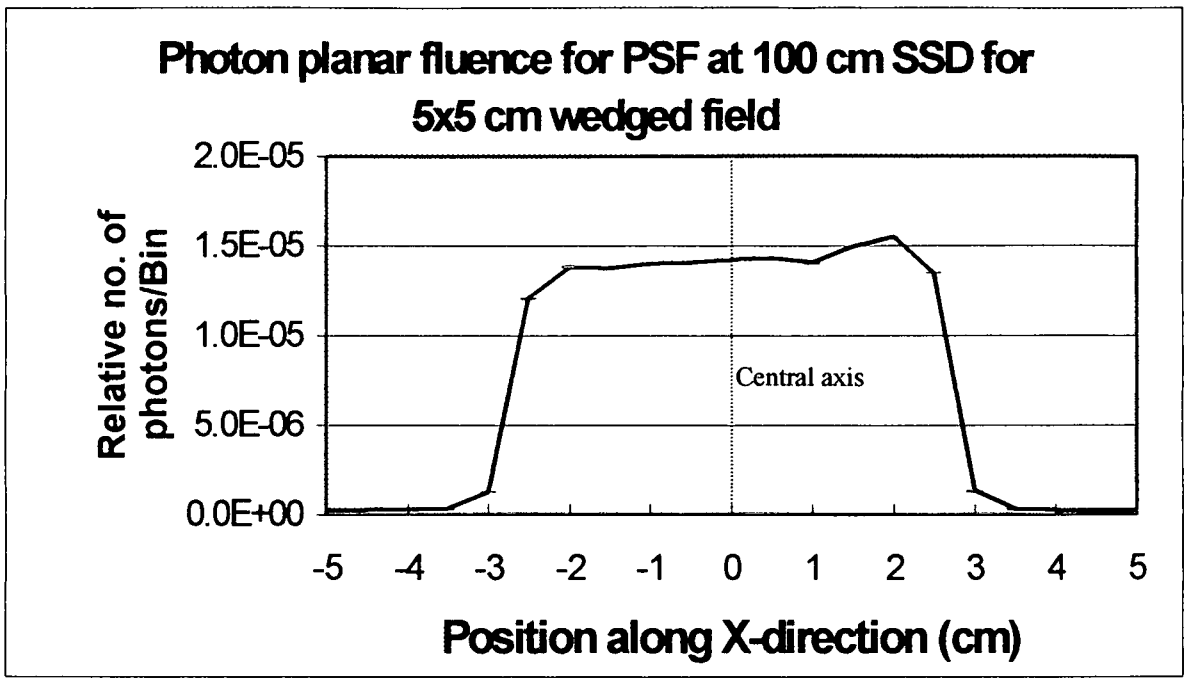

Figure 7.4 The photon planar fluence at 100 cm SSD for a 5x5 cm wedged square field. The statistical error bars are within one percent. A total of 20 bins of width 5 mm each were chosen to set up the energy fluence profile. The results shown in figs. 7.1 to 7.4 show PSF data analyzed with the BEAMDP code. The PSF's generated for the open and wedged beams were used as sources for the generation of water phantom beam data with the DOSXYZ code.

7.1.2 Input beam data for the TPS generated by DOSXYZ

As mentioned in chapter 6 dealing with the methods employed in this study, it was necessary to generate Monte Carlo (MC) based input beam data since a generic accelerator was used to evaluate the dose calculations on the TPS. The simulations were performed in a water phantom constructed in the DOSXYZ code. The data presented here were calculated with a 5x5x5 mm^3 voxel size. This coincides with the grid spacing used by the TPS for the input beam data. The relevant beam data was sampled from the output .3ddose files from DOSXYZ after the dose were normalized to the ***maximum dose on the central beam axis***. For each field the following set of data were obtained: Five beam profiles at depths of 2, 5, 10, 15 and 25 cm as well as a percentage depth dose curve along the central beam axis.

Data for 20x20 cm^2 fields were not generated because it would take about $12*10^9$ histories in patient models, taking about 8 weeks per field. This would reduce the statistical uncertainty to about one percent. The statistics would be less optimal if the simulations were performed in say two weeks. Thus time was considered a limiting factor.

The relevant data are shown in figures 7.5 to 7.12 for open fields and 7.13 to 7.20 for wedged fields.

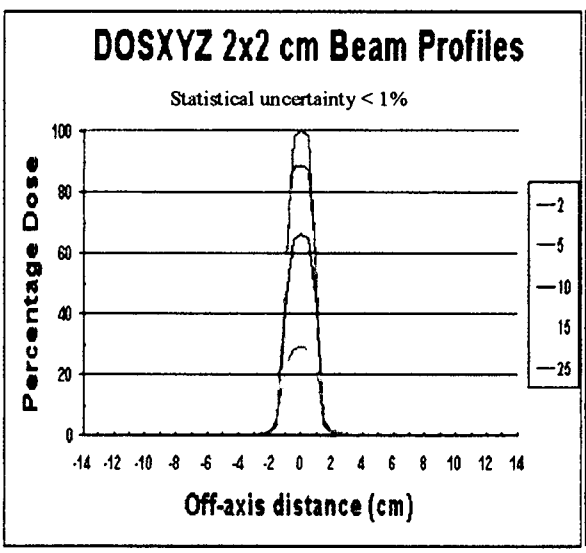

Figure 7.5

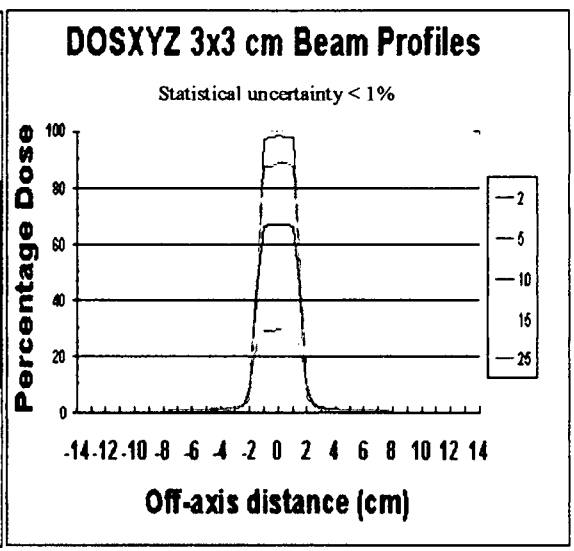

Figure 7.6

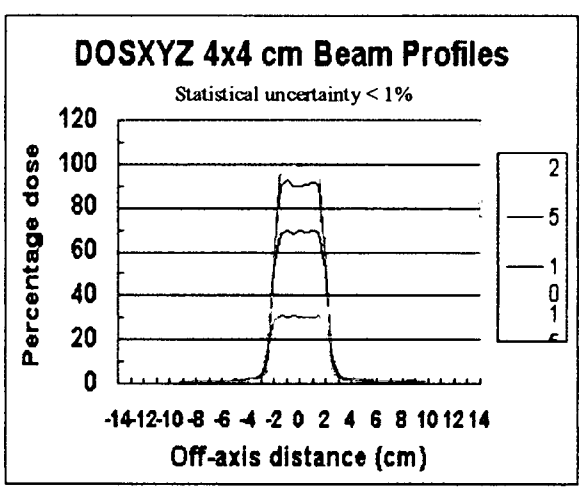

Figure 7.7

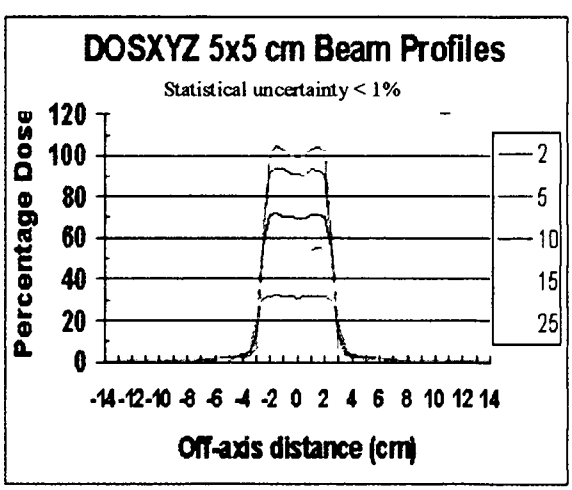

Figure 7.8

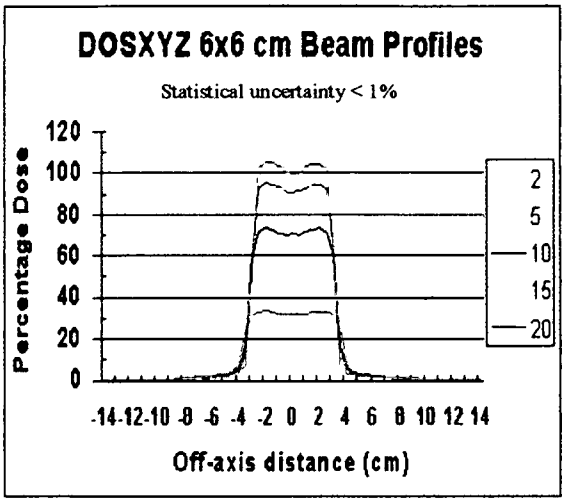

Figure 7.9

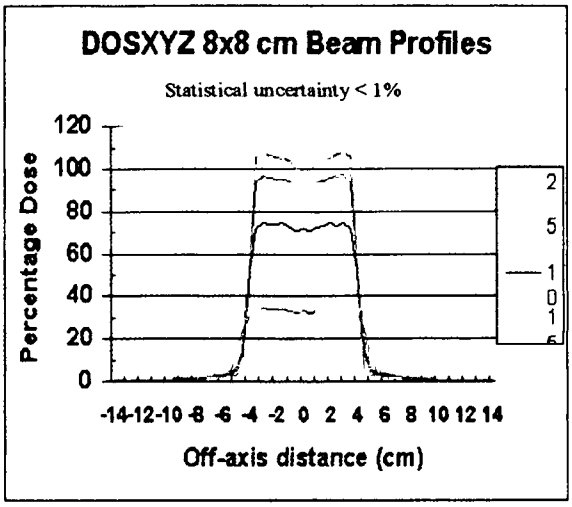

Figure 7.10

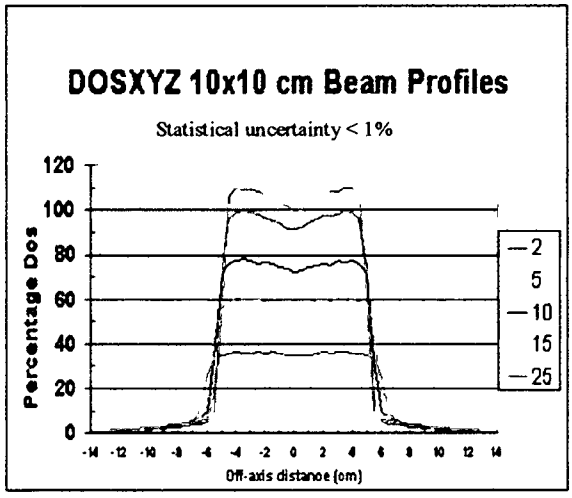

Figure 7.11

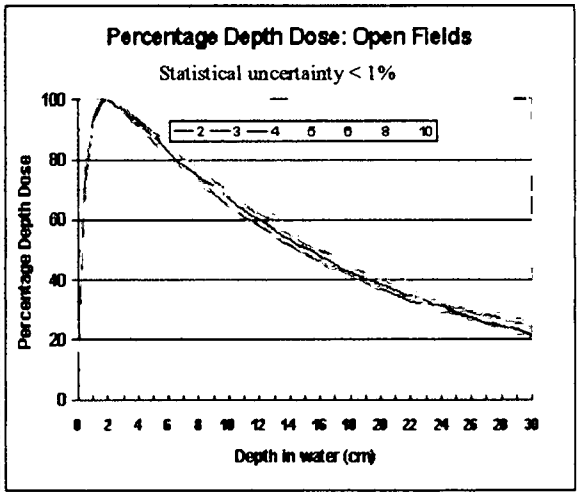

Figure 7.12

Figures 7.5 to 7.11 Open field beam profiles for 4x4 to 10x10 cm square open fields generated by the DOSXYZ code on a 5 mm grid spacing in the x, y and z directions. The legends indicate the depth in cm.

Figure 7.12 Percentage depth dose curves for the 2x2, 3x3, 4x4, 5x5, 6x6, 8x8 and 10x10 cm ^{2} open fields generated by the DOSXYZ code for a grid spacing of 5 mm.

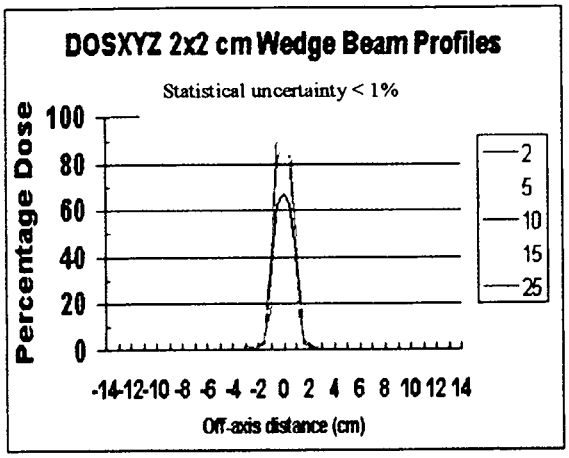

Figure 7.13

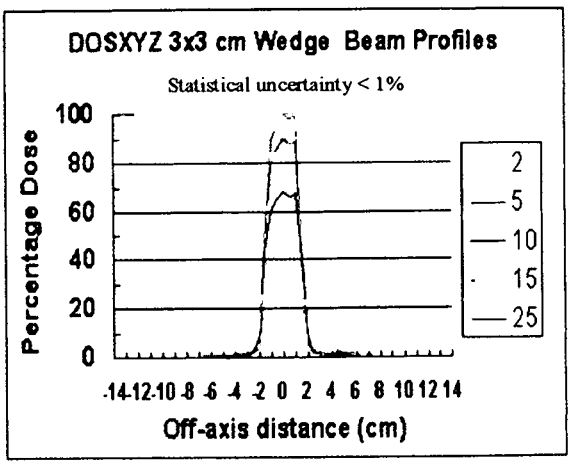

Figure 7.14

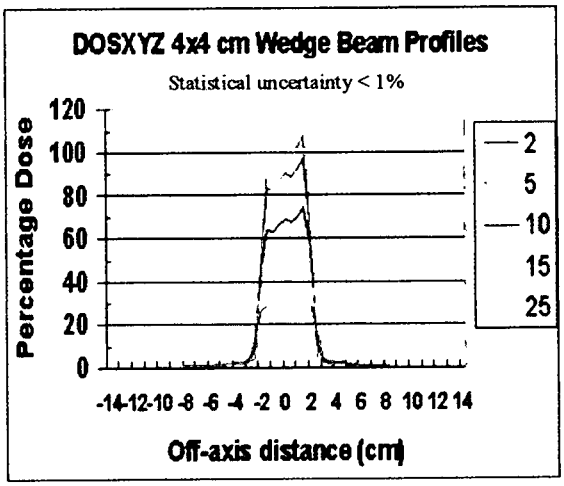

Figure 7.15

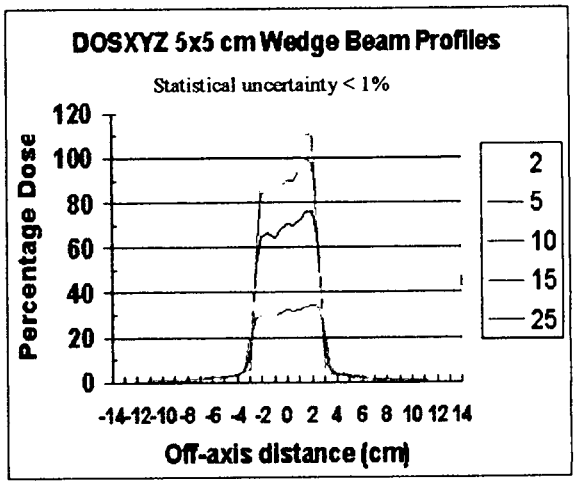

Figure 7.16

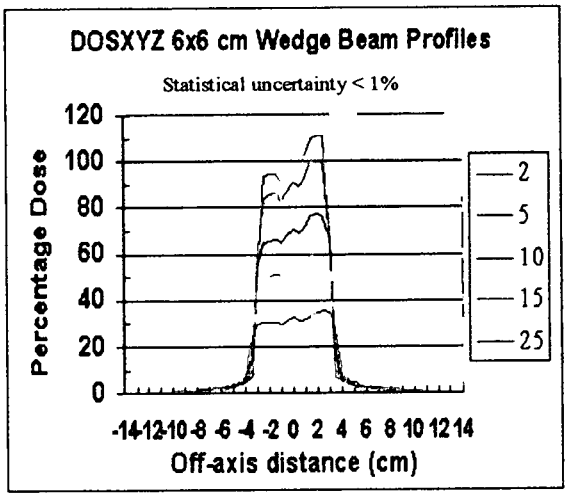

Figure 7.17

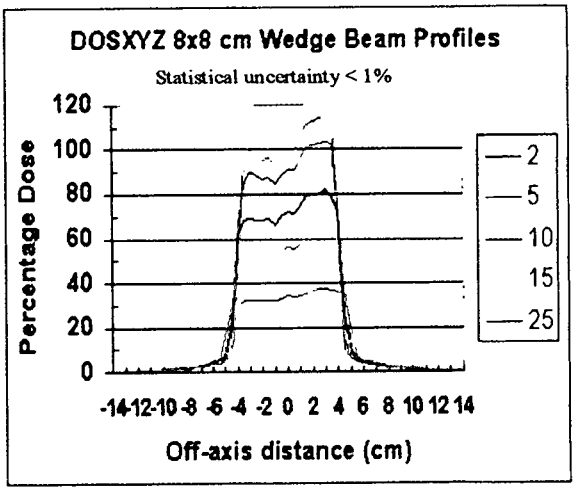

Figure 7.18

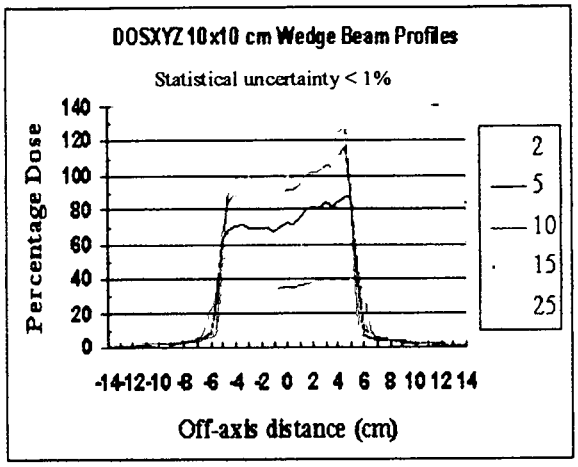

Figure 7.19

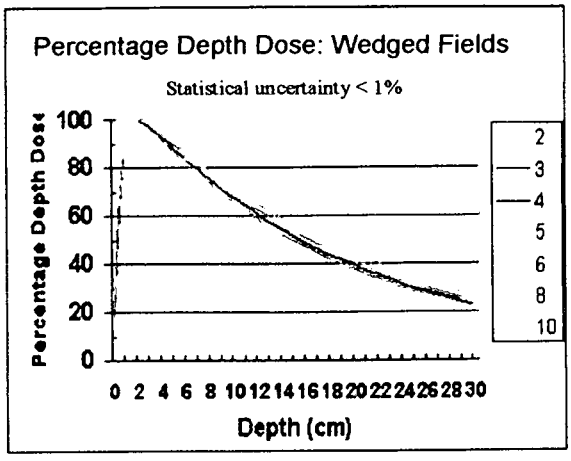

Figure 7.20

Figures 7.13 – 7.19 Wedge field beam profiles for 2x2 to 10x10 cm square fields generated by the DOSXYZ code on a 5 mm grid spacing in the x, y and z directions. The legends indicate the depth in cm.

Figure 7.20 Percentage depth dose curves for the 2x2, 3x3, 4x4, 5x5, 6x6, 8x8 and 10x10 cm ^{2} wedged fields generated by the DOSXYZ code for a grid spacing of 5 mm.

7.1.3 The verification of the input beam data for the TPS

The water phantom data generated by DOSXYZ for entering as generic accelerator data into the TPS are shown in figures 7.5 to 7.20. After this data was imported into the TPS the dose was calculated in a water phantom with the TPS. The comparative water phantom data generated by DOSXYZ and the TPS are shown in figs. 7.21 to 7.26 for the open x-ray beams. Figures 7.27 to 7.32 show the data for the wedge x-ray beams. The beam profile data are shown at depths of 2, 5, 10, 15 and 25 cm in the x-direction of the fields. Comparative depth dose distributions are also shown. The dose data were evaluated for the 2x2, 5x5 and 10x10 cm^2 x-ray field sizes. These are also the field sizes used in this study for the calculation of dose distributions in patient models.

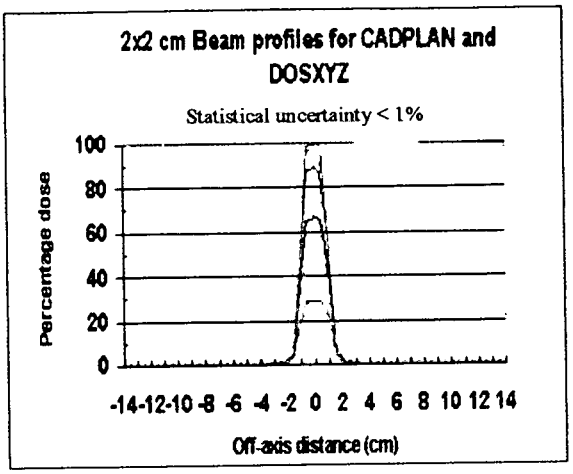

Figure 7.21

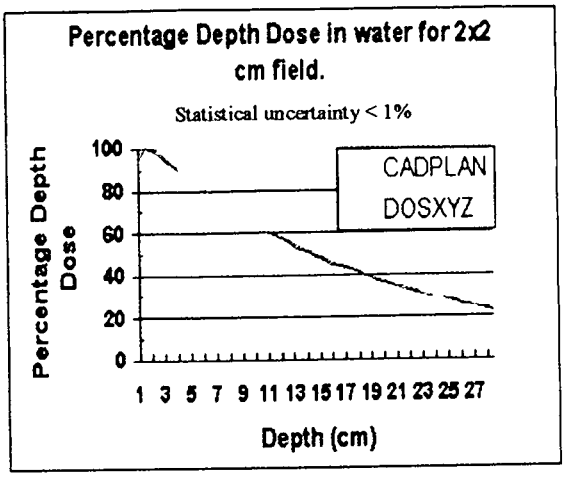

Figure 7.22

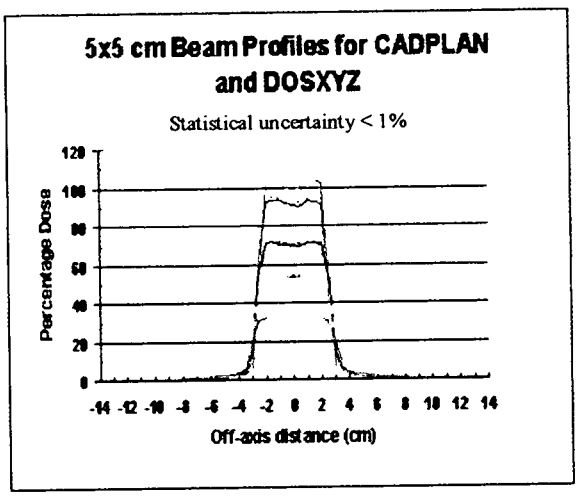

Figure 7.23

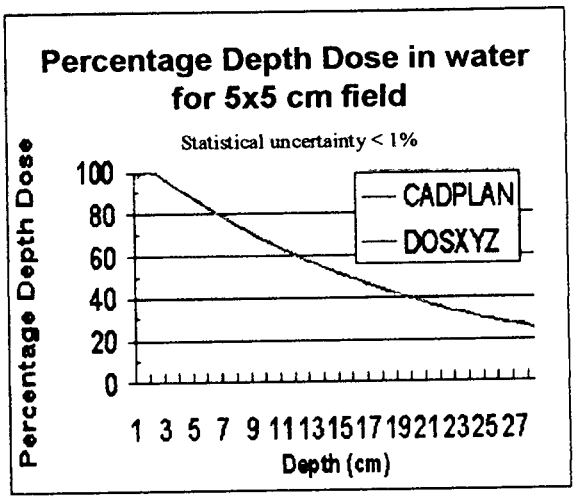

Figure 7.24

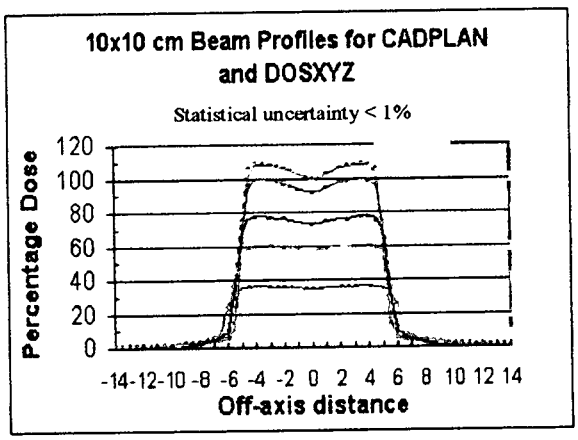

Figure 7.25

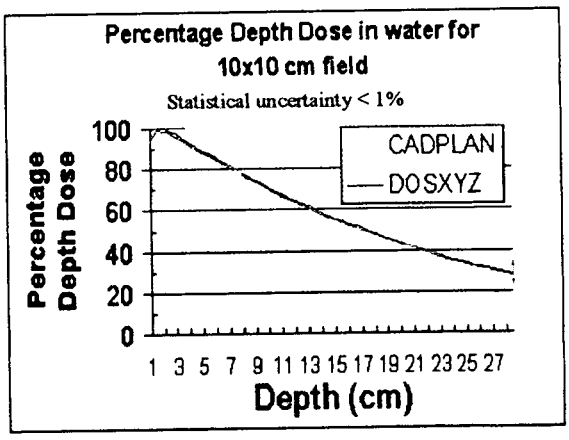

Figure 7.26

Figures 7.21, 7.23 and 7.25: Dose profiles at depths indicated by: blue = 2 cm, red = 5 cm, black = 10 cm, green = 15 cm and purple = 25 cm. Solid lines: DOSXYZ, broken lines: CADPLAN. Figures 7.22, 7.24 and 7.25: Depth dose curves for DOSXYZ and CADPLAN in a water phantom.

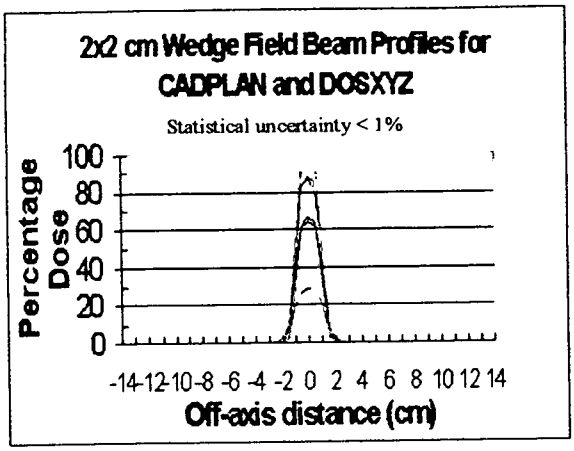

Figure 7.27

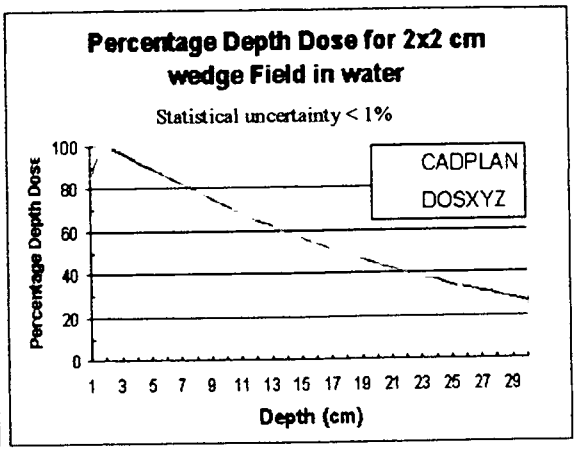

Figure 7.28

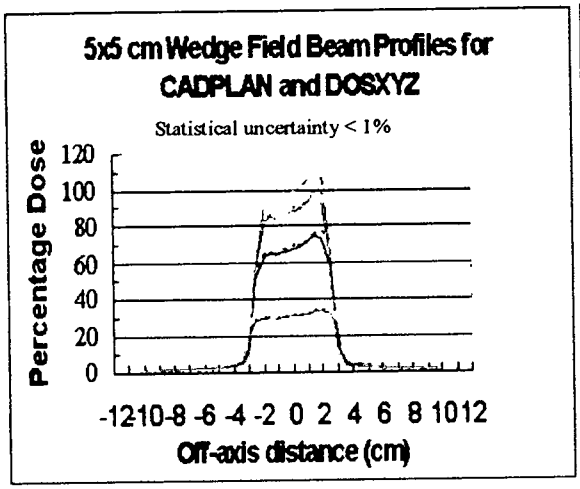

Figure 7.29

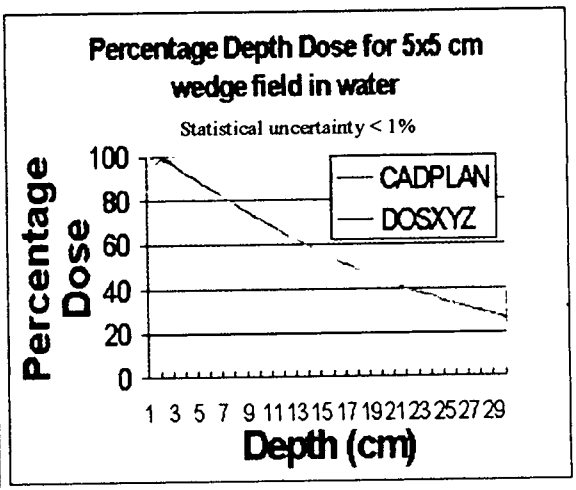

Figure 7.30

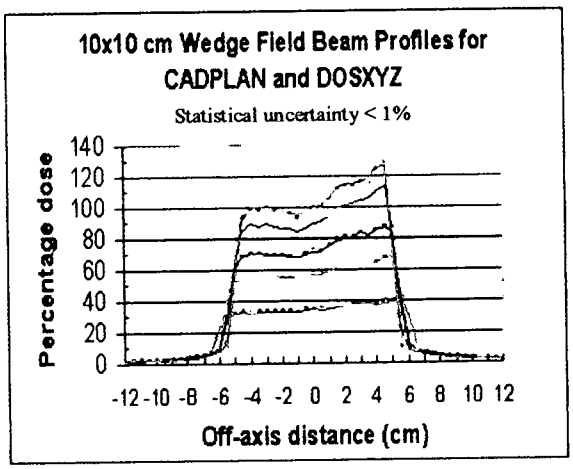

Figure 7.31

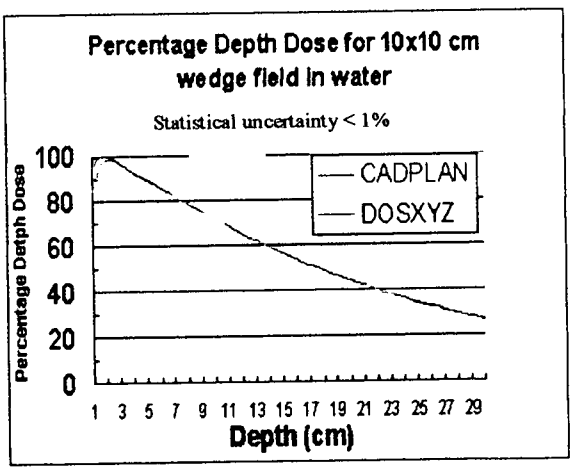

Figure 7.32

Figures 7.27, 7.29 and 7.31: Wedged beam dose profiles at depths indicated by: blue = 2 cm, red = 5 cm, black = 10 cm, green = 15 cm and purple = 25 cm. Solid lines: DOSXYZ, broken lines: CADPLAN. Figures 7.28, 7.30 and 7.32: Depth dose curves for DOSXYZ and CADPLAN in a water phantom.

7.1.4 The transformation of CT based patient models into a format suitable for DOSXYZ

Patient models are constructed from CT slice data. The TPS under evaluation converts each CT image into an electron density matrix through the suitable transformation of CT number to relative electron density. The DOSXYZ code cannot use the CT numbers to generate cross-section data with the PEGS4 code. This section gives the main results extracted from a publication (Du Plessis et al, 1998) outlining a basic method for transforming CT image data into a suitable format for direct use by the DOSXYZ code.

7.1.4.1 Dosimetrically equivalent tissue subsets

In figure 7.33 the percentage difference with respect to water of the depth dose curves of all the tissues excluding adipose, cortical bone, cartilage and inflated lung are shown. Figure 7.34 shows the corresponding curves for various densities of lung and adipose tissue and figure 7.35 for various densities of cortical bone and cartilage.
This data was used to separate the tissues into subsets, such that the members in each subset differed by less than one percent in depth dose. The resulting tissue subsets are shown in table 7.1.

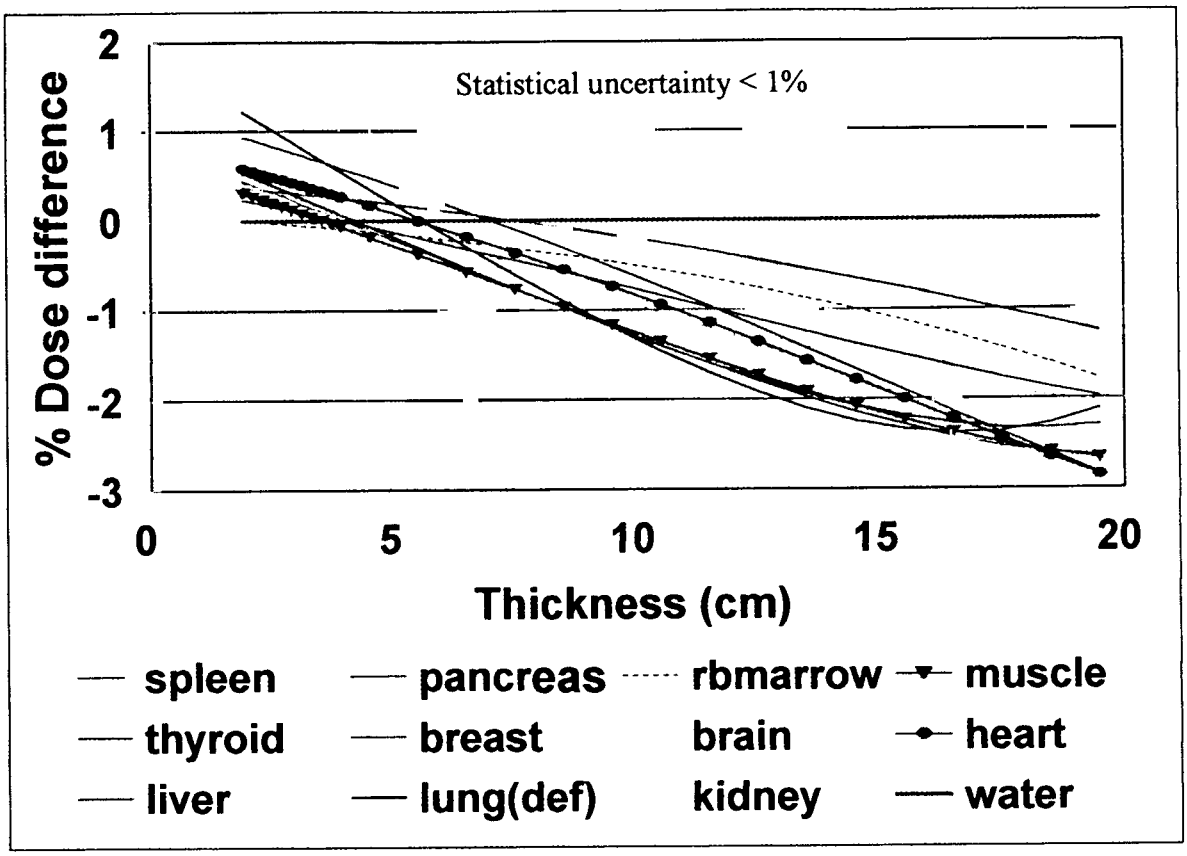

Figure 7.33. The percentage difference in depth dose relative to water of various tissue types obtained from depth dose simulations with Monte Carlo methods. This data was obtained after the original depth dose data was smoothed with quadratic functions over the range 2 cm to 20 cm and each tissue type's smoothed percentage depth dose curve was subtracted from that of water. The physical densities (g/cm^3) are given as: spleen: 1.06, thyroid: 1.05, liver: 1.06, pancreas: 1.04, breast: 1.02, deflated lung: 1.05, red bone marrow: 1.03, brain: 1.04, kidney: 1.05, muscle: 1.05, heart: 1.06, water: 1.00

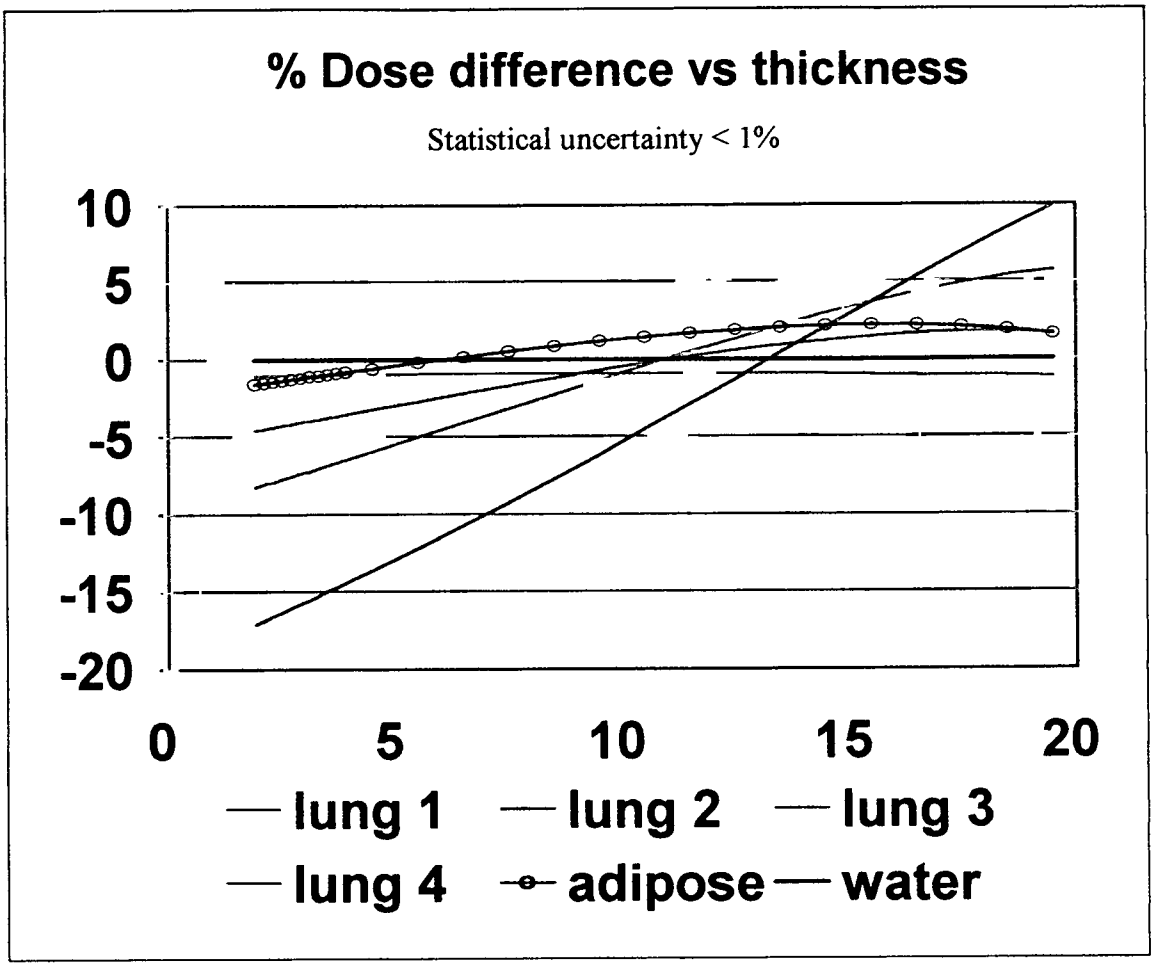

Figure 7.34. The percentage difference in depth dose relative to water of various densities of lung and adipose tissue obtained from depth dose simulations with Monte Carlo methods. This data was obtained after the original depth dose data was smoothed with quadratic functions over the range 2 cm to 20 cm and each tissue type's smoothed percentage depth dose curve was subtracted from that of water. The physical densities (g/cm^3) are given as: lung1: 0.6, lung2: 0.8, lung3: 0.9, lung4: 1.0, adipose: 0.95

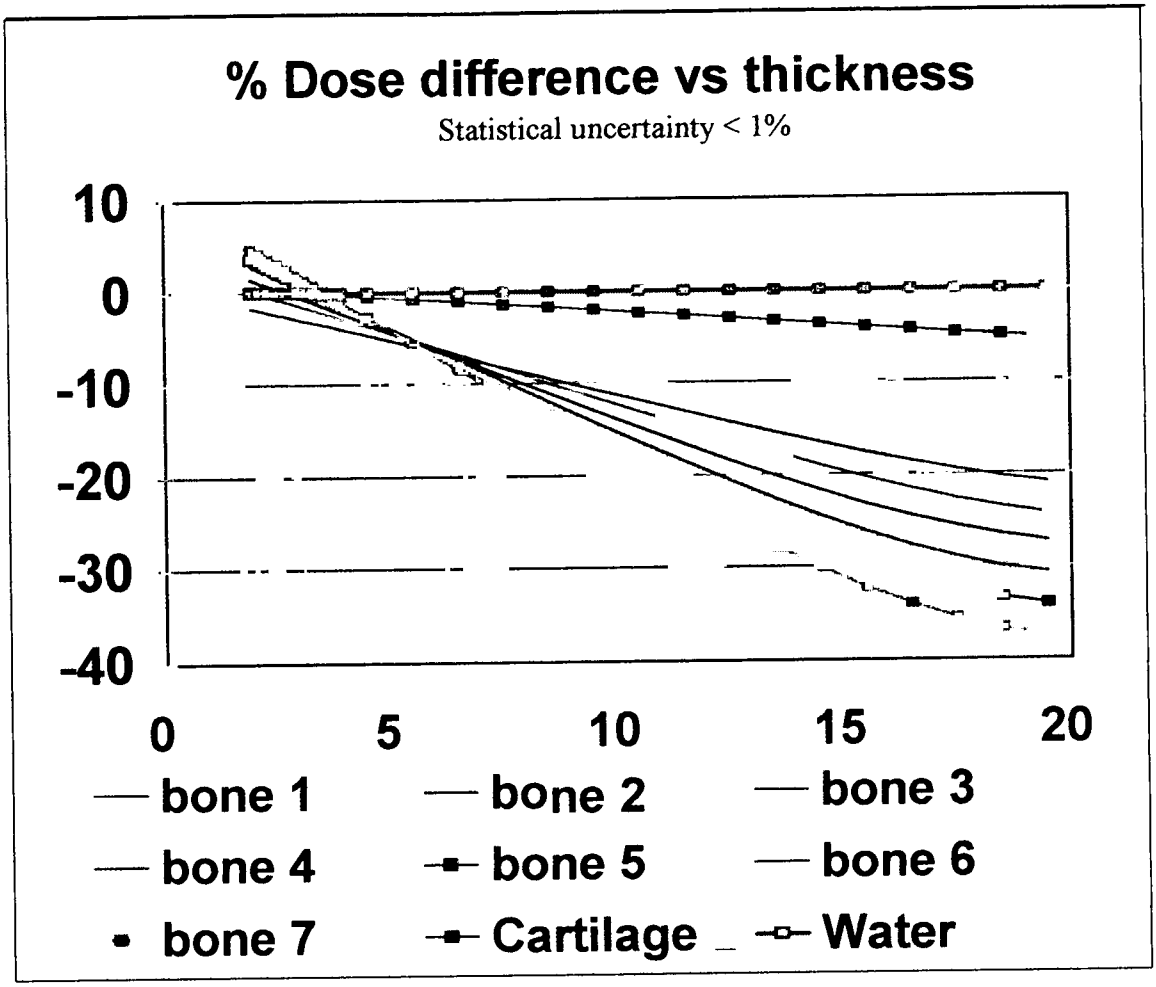

Figure 7.35. The percentage difference in depth dose relative to water of various densities of skeletal bone and cartilage obtained from depth dose simulations with Monte Carlo methods. This data was obtained after the original depth dose data was smoothed with quadratic functions over the range 2 cm to 20 cm and each tissue type's smoothed percentage depth dose curve was subtracted from that of water. The physical densities (g/cm^3) are given as: bone1: 1.4, bone2: 1.6, bone3: 1.8, bone4: 1.9, bone5: 2.0, bone6: 2.2 and cartilage: 1.1

SUBSET	TISSUE	Electron density $m^{-3} \times 10^{26}$	Lower CT limit	Upper CT limit
1	Lung (inflated)	862	20	950
2	Adipose	3180	951	980
3	Water	3340	981	1010
4	Brain	3460	1011	1040
	Breast	3390		
	Pancreas	3460		
	Redmarrow	3420		
5	Heart	3510	1041	1070
	Kidney	3480		
	Thyroid	3480		
	Lung(deflated)	3480		
	Liver	3510		
	Muscle	3480		
	Spleen	3510		
6	Skeletal bone (cartilage)	3520	1071	1100
7	Skeletal bone (cortical)	5950	1101	3000

Table 7.1. The different tissue types and the subsets into which they are separated based on the percentage difference in depth dose obtained with CYLTRAN based Monte Carlo simulations. Electron density values for the different tissue types were taken from ICRU 44. The two columns on the right shows the CT number ranges associated with the subsets of materials.

7.1.4.2 CT number intervals

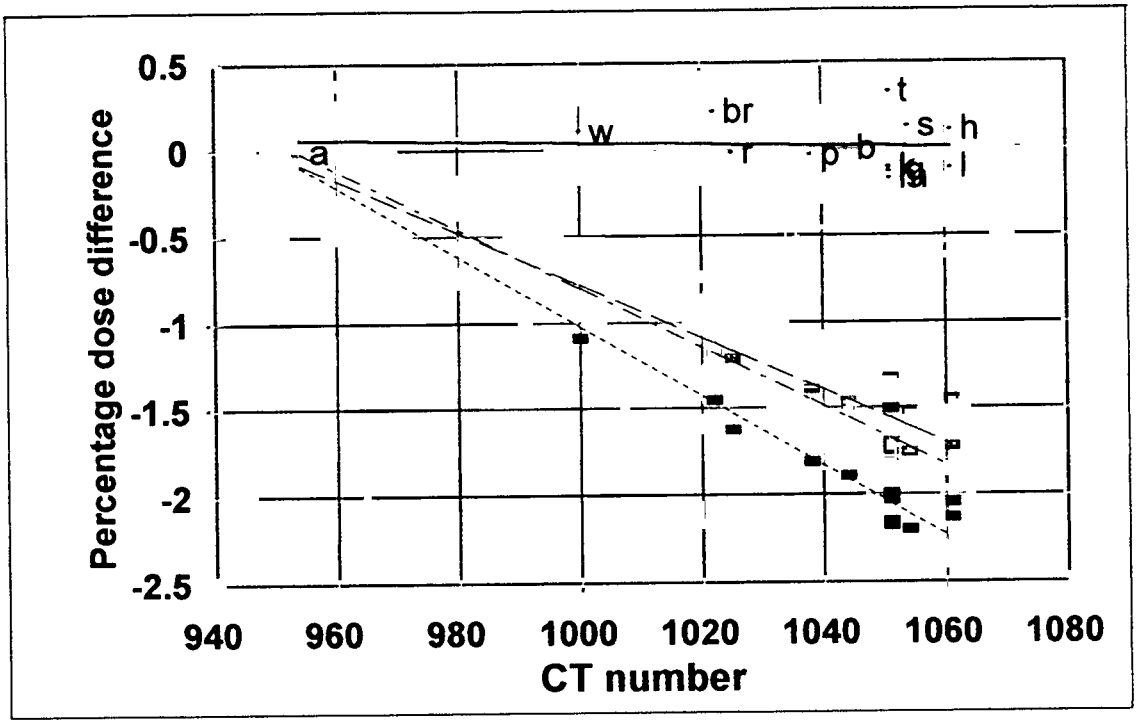

Figure 7.36 The percentage dose difference obtained by subtracting the depth dose data of various soft tissues from the dose of adipose tissue at depths of 5 □, 10 □ 15□ and 20■ cm. The solid lines are the linear fitted data and the markers represent the 12 different soft tissue types each labeled in data set 2 (depth 10 cm) according to a = adipose, w = water, br = breast, r = redmarrow, p = pancreas, t = thyroid, s = spleen, h = heart, l = liver, lg = lung (deflated), b = brain, k = kidney, m = muscle.

The same procedure was repeated for various densities of inflated lung and cortical bone as can be seen in figures 7.37 and 7.38

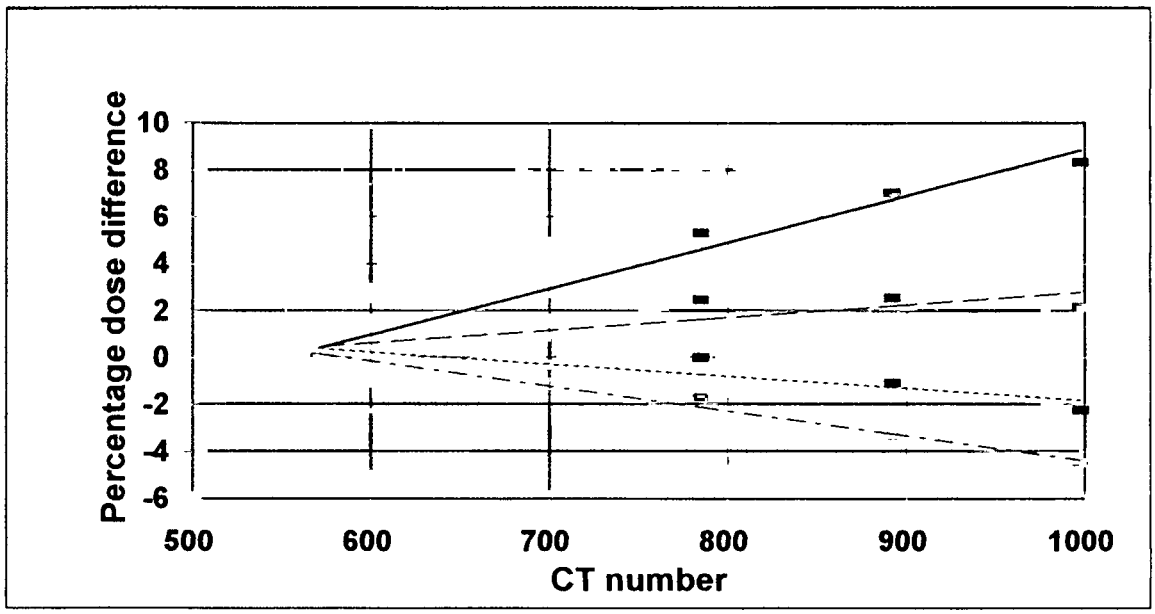

Figure 7.37 The percentage dose difference for lung phantoms of different density at depths of 5 □, 10□, 15 □ and 20 ■ cm. This was obtained in the same manner as in figure 4 but subtraction was done from the dose of the lung having the lowest density (CT number = 570).

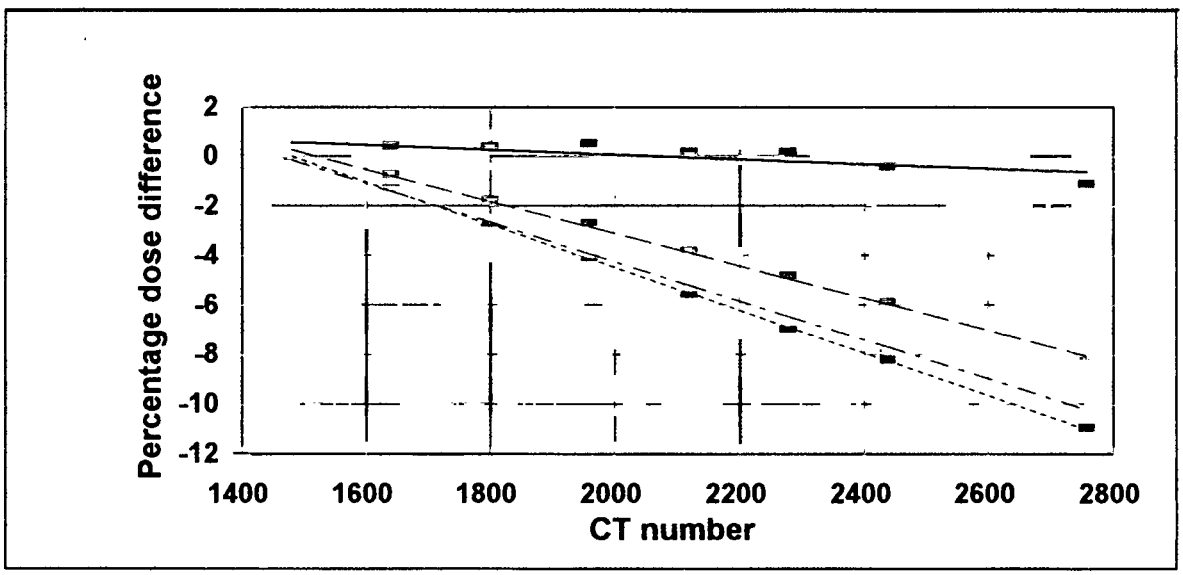

Figure 7.38 The percentage dose differences as in figs. 34 and 35 for different densities of hard bone.

From each of these graphs the CT number interval corresponding to a dose variation not exceeding one percent, was determined. This was calculated from the inverse of the slope of the graphs in figures 7.36 - 7.38, which represents the change in CT number per unit percentage dose difference. Figure 7.39 shows these inverse slopes as a function of tissue thickness. For soft tissue and lung, a CT number interval of about 30 HU, and for bone a CT number interval of about 100 HU would result in dose differences of less than one percent.

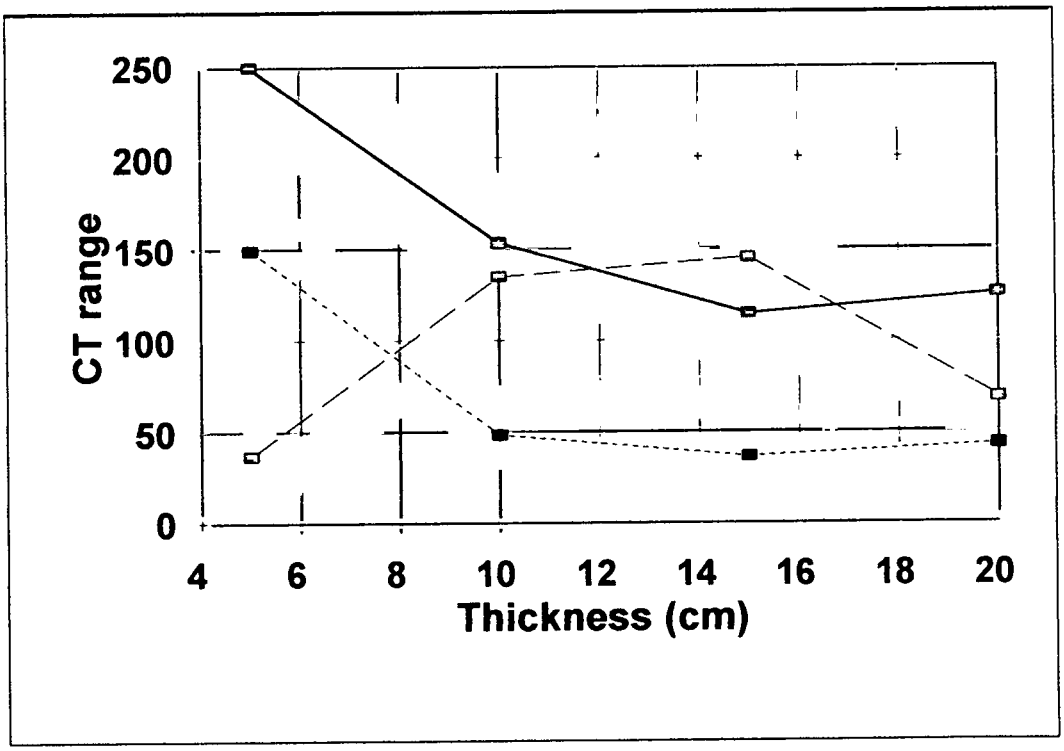

Figure 7.39 The CT intervals calculated from the slopes of the graphs in figs 7.36 - 7.38, for cortical bone (—), soft tissue (- - -) and lung (• • •).

7.1.4.3 Conversion of CT numbers to material types

Figure 7.39 indicated that the maximum allowable CT number interval can be taken as 30 HU for inflated lung and all the soft tissues up to subset 6 in table 7.1. For the bone type tissues (subset 7 in table 7.1) the maximum CT number interval was chosen as 100 HU.

These CT intervals will minimize the effect of phantom (organ) thickness. A FORTRAN program was written to read CT images and to convert each pixel's CT number into a corresponding material number. A flowchart of the program is shown in figure 7.40. The procedure consists of setting up a series of bins between the CT numbers 0 and 1100 with equal width of 30 HU and to repeat it over the range of 1100 to 3000 with equal widths of 100 HU. A CT image's pixels are read and the bins in which these will fall are determined. Each pixel value is then set to the bin number, which in turn is linked to a material type.

These materials are chosen from any of those found in the 7 subsets of materials listed in table 7.1 with the restriction that precisely one can be chosen out of each subset. As can be seen from table 7.1 subsets 2 to 6 each spans a CT range of 30 HU, exactly one bin width. However subsets 1 and 7 span a range of CT numbers containing several bin widths, i.e. 32 for lung and 19 for bone. In order to assign a material type to each of these bins the basic composition of lung and bone is used but their physical densities are varied in steps, leading, via the corresponding electron densities, to CT numbers covering the desired range.

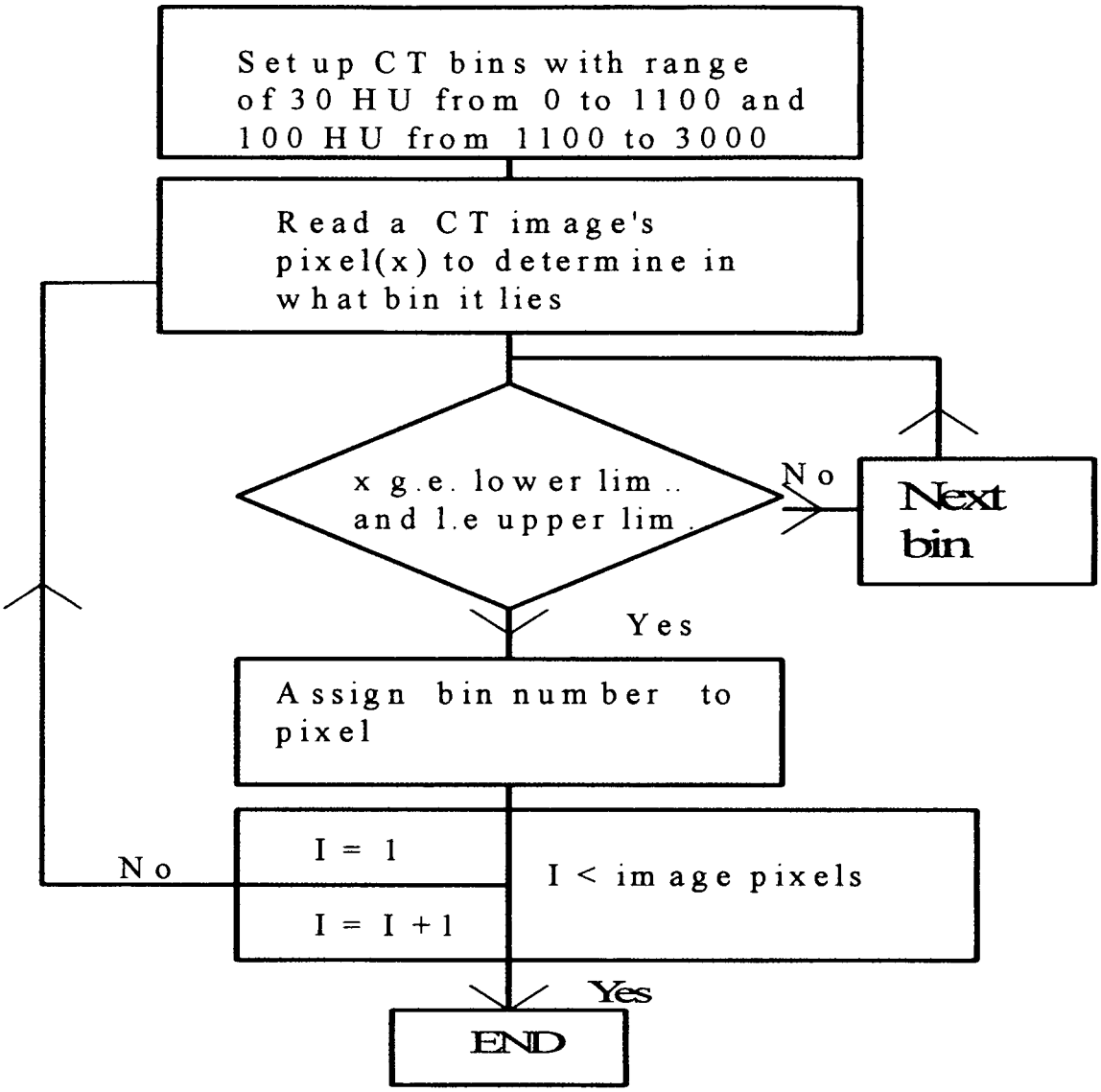

Figure 7.40 The basic operation of converting a CT image into one suitable for use with Monte Carlo simulations. As a first step the program calculates a series of bin intervals ranging from CT number 0 to 1100 with equal width of 30 HU, and bin intervals of 100 HU for CT numbers between 1100 and 3000. A CT image's pixels are read and it is determined in which CT intervals (bins) they will fall by determining the upper limit and the lower limit of the particular intervals. The pixel value is then converted to the bin number, which in turn is linked to a certain material type.

In our application we have chosen one material out of each subset as shown in table 7.2. Note that any of the other materials in the subsets would also suffice, provided that only one material from each of the 7 subsets is chosen. These materials serve as the basis for

constructing an input file for Monte Carlo programs since each of these programs have a preprocessor program which calculates each material's cross section data. They all need the atomic components, weight fractions and physical density of each material in order to do these calculations (see table 7.2).

tissue	H	C	N	O	Na	S	Cl	P	K	Fe	Ca	ρ g/cm^3
Lung	10.3	11.0	3.1	74.9	0.2	0.3	0.3	0.2	0.2			0.28
Adipose	11.4	60.0	0.7	27.8	0.1	0.1	0.1					0.95
Water	11.2			88.8								1.00
Brain	10.7	15.0	2.2	71.2	0.2	0.2	0.3	0.4	0.3			1.04
Heart	10.3	12.0	3.2	73.4	0.1	0.2	0.3	0.1	0.2	0.1		1.06
Cartilage	9.6	10.0	2.2	74.4	0.5	0.9	0.3	2.2				1.10
Cortical Bone	3.4	16.0	4.2	43.5	0.1	0.3		10.			22.	1.92

Table 7.2. The chosen materials with their atomic compositions shown as percentage weight fractions and physical density (ρ), for use in a Monte Carlo preprocessing program which calculates cross section data. This was assembled by taking one material type from each subset in table 7.1 and using its atomic composition data as found in ICRU 44.

7.1.5 Comparison between the dose distributions calculated by DOSXYZ and by the TPS for the BATHO and ETAR algorithms

7.1.5.1 Open x-ray field data

This section presents the difference between the dose calculations of DOSXYZ and the TPS Batho and ETAR algorithms for the 2x2, 5x5 and 10x10 cm^2 open x-ray beams in a maxillary sinus, lung and prostate patient model. The data shown in figures 7.41 - 7.49 are dose difference volume histograms (DDVH's) for each x-ray field and patient model.

The interpretation of this data is as follows: On the horizontal axis we have the percentage dose difference and on the vertical axis we have the percentage of the volume corresponding to that percentage dose difference. In other words the vertical axis shows the percentage of the volume that have a difference in dose when the Batho and ETAR percentage dose distributions are directly compared with the DOSXYZ percentage dose. The histogram generated gives the reader an impression of the dose difference between the Batho and ETAR dose calculation methods and the DOSXYZ percentage dose in the same patient model and for the same field size. The percentage of the irradiated volume that has a certain dose difference can be read of directly from the vertical axis. The volume included in these comparisons is the central slice with a thickness of 1 cm. These are the same slices in which the dose distributions were calculated with the TPS.

These histograms were calculated by comparing the dose values calculated by the ETAR and BATHO algorithms with the corresponding DOSXYZ dose values for a specific field size and patient model.

The statistical uncertainty is also mentioned in these plots. The plots shown here are taken from the average dose values of the DOSXYZ plots. These data do not show the effects of these uncertainties, but is taken into account in the statistical uncertainty analysis in table 8.2 from table 8.1. Another important issue is the effect that different random number sequences would have on these plots or more basically, the dose distributions of the DOSXYZ generated data. This was not studied explicitly but it seems that, provided enough histories are sampled, this would not cause a significant alteration in the absorbed dose simulations. If the random number generator is such that it can model stochastic processes realistically, then the resulting Monte Carlo calculated dose distributions cannot differ from purely choosing different starting values of the random generator seeds. It would simply mean that another set of stochastically modeled particle transport steps are simulated that on average would result in the same dose distribution from very different particle transport simulations. This would be true for a large number of histories of the same order as used in this study.

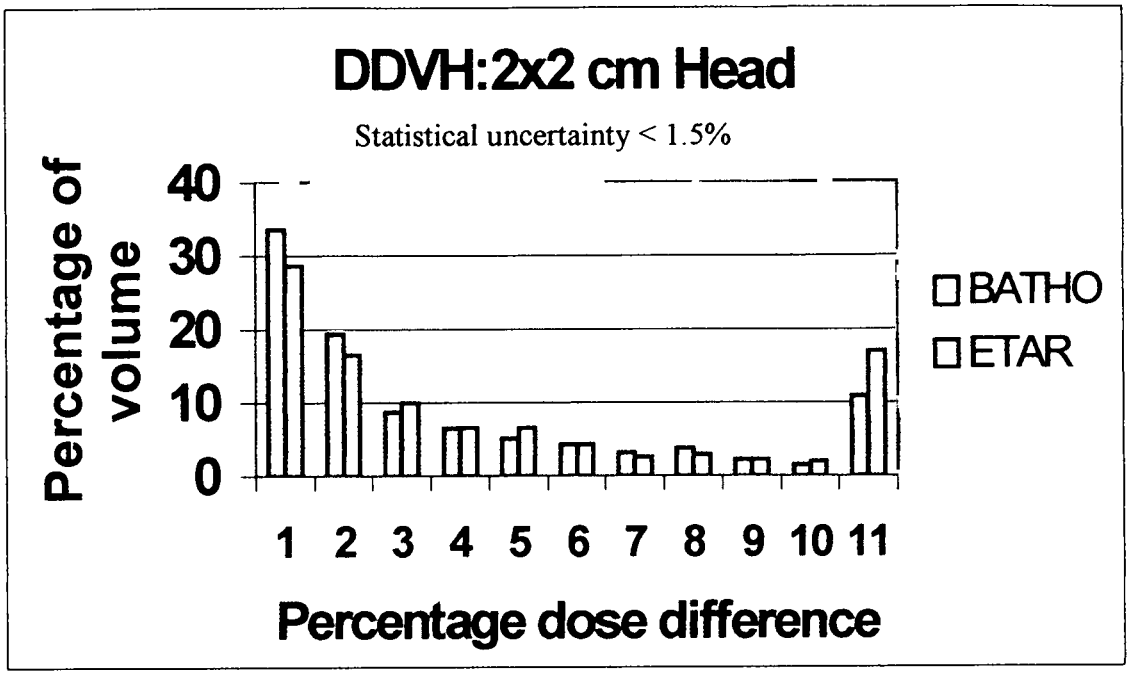

Figure 7.41 Dose difference volume histogram for the 2x2 cm^2 open x-ray field in the maxillary sinus (head) patient model.

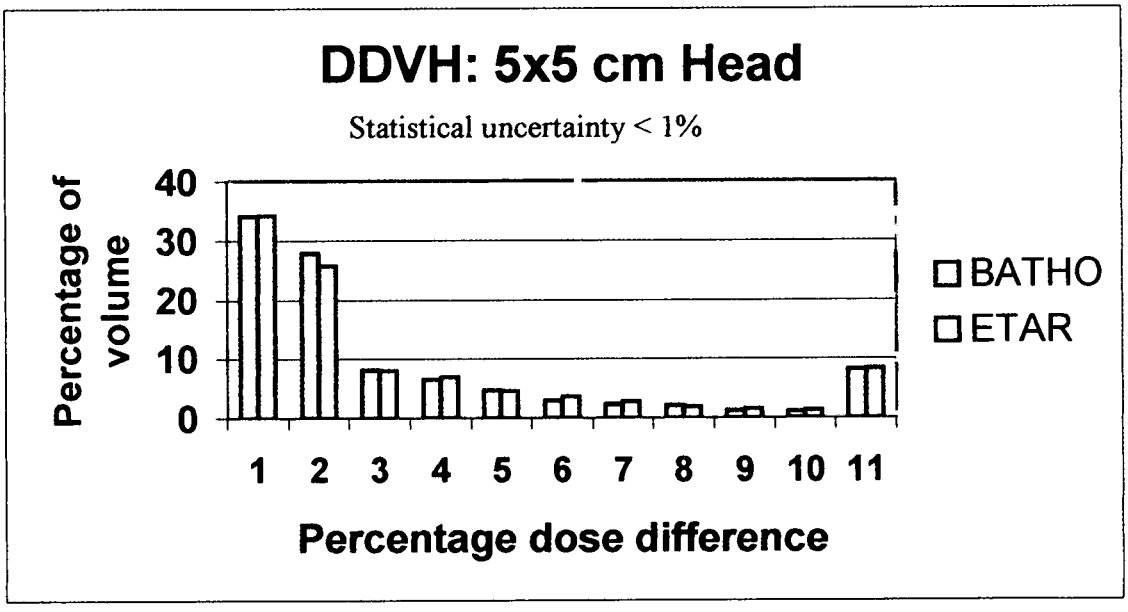

Figure 7.42 Dose difference volume histogram for the 5x5 cm^2 open x-ray field in the maxillary sinus (head) patient model.

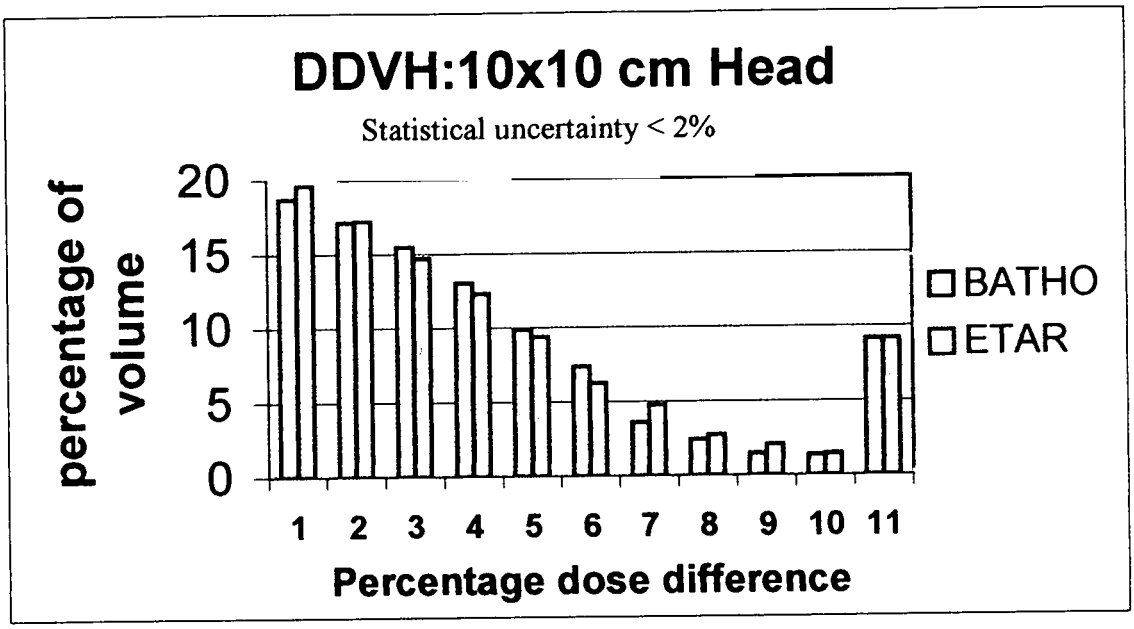

Figure 7.43 Dose difference volume histogram for the 10x10 cm^2 open x-ray field in the maxillary sinus (head) patient model.

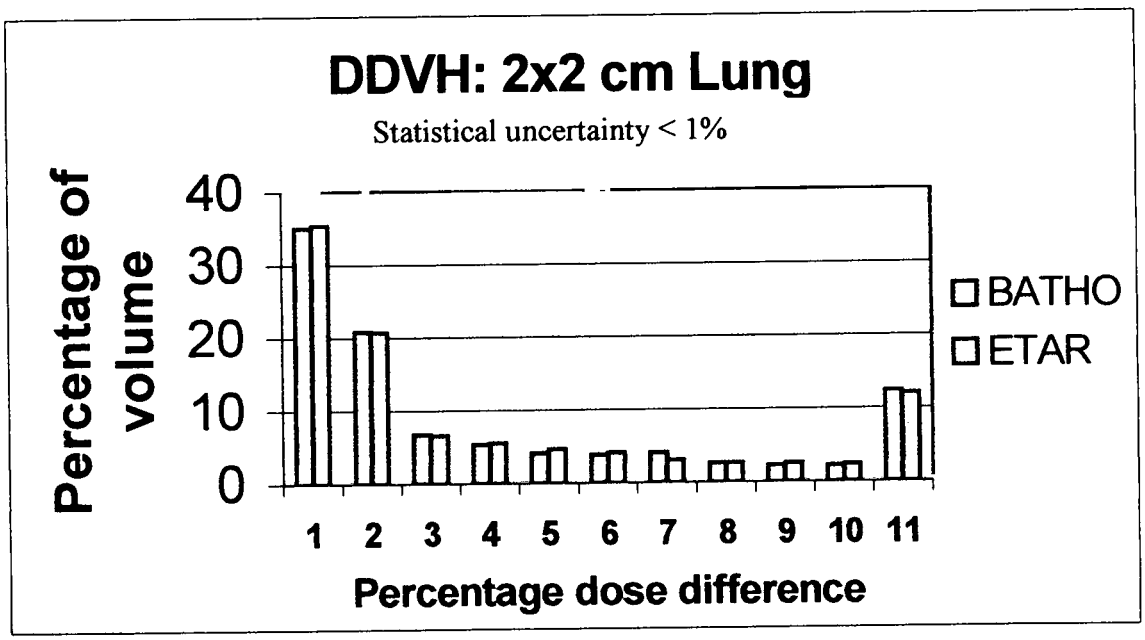

Figure 7.44 Dose difference volume histogram for the 2x2 cm^2 open x-ray field in the lung patient model.

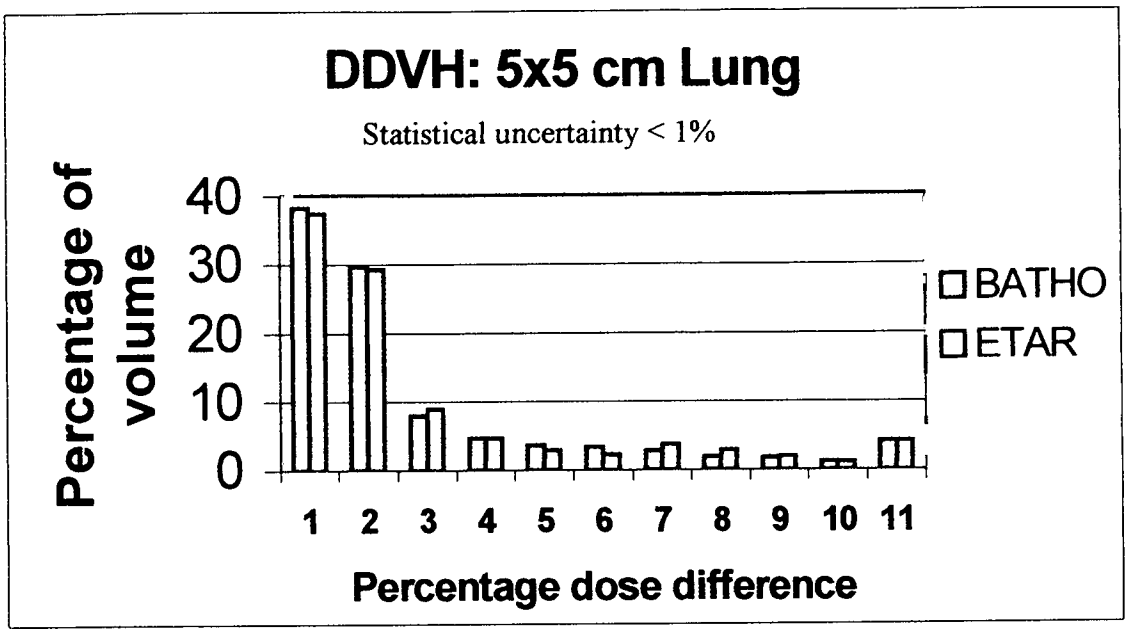

Figure 7.45 Dose difference volume histogram for the 5x5 cm^2 open x-ray field in the lung patient model.

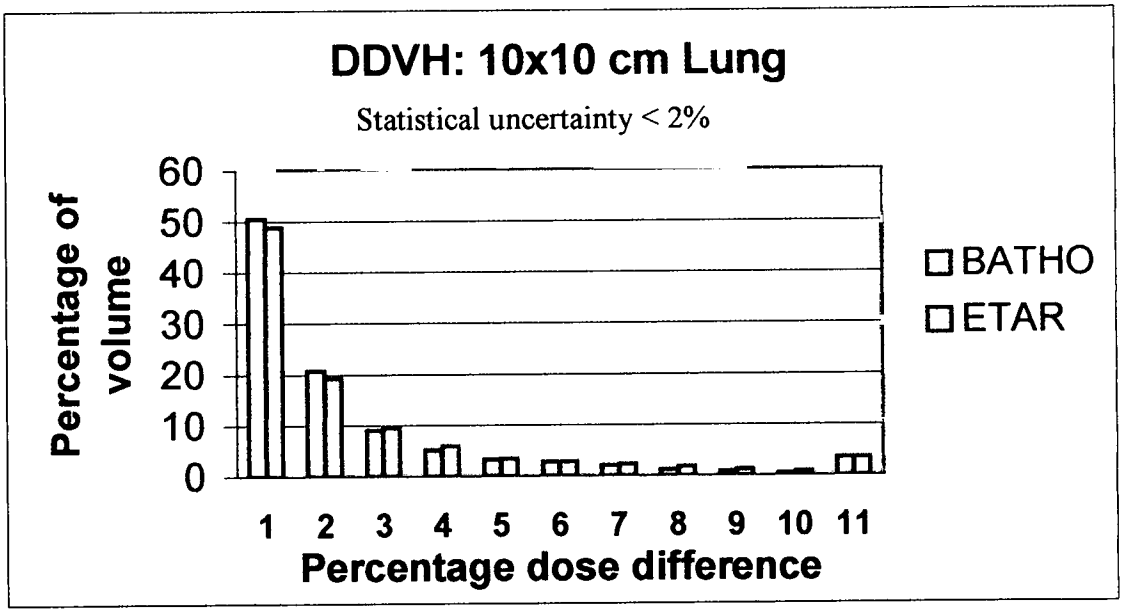

Figure 7.46 Dose difference volume histogram for the 10x10 cm^2 open x-ray field in the lung patient model.

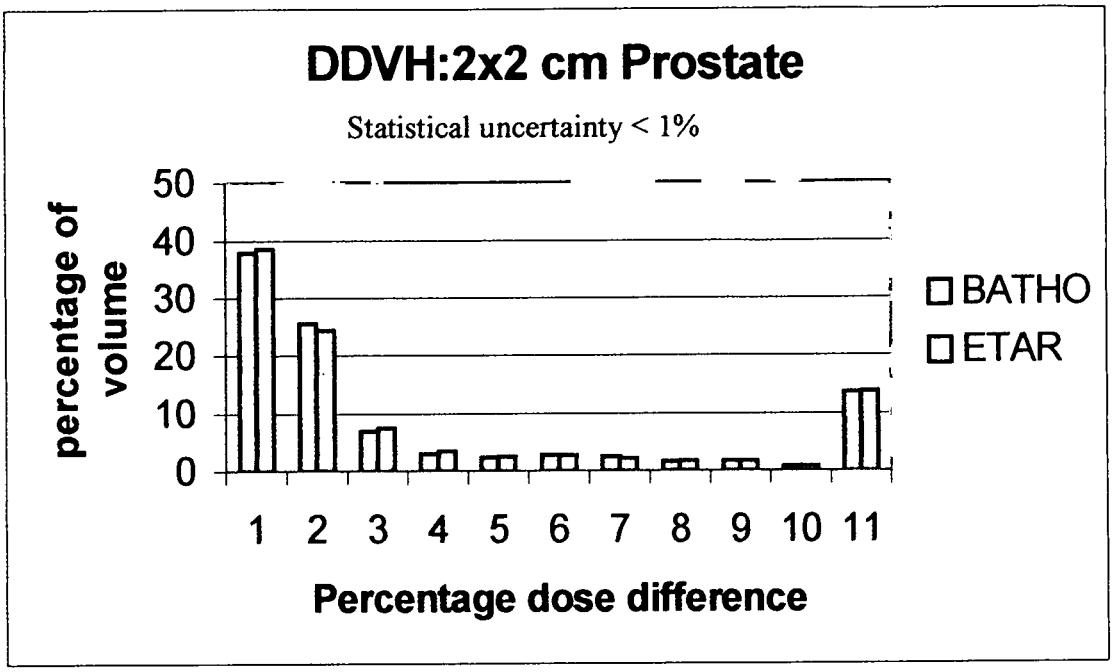

Figure 7.47 Dose difference volume histogram for the 2x2 cm^2 open x-ray field in the prostate patient model.

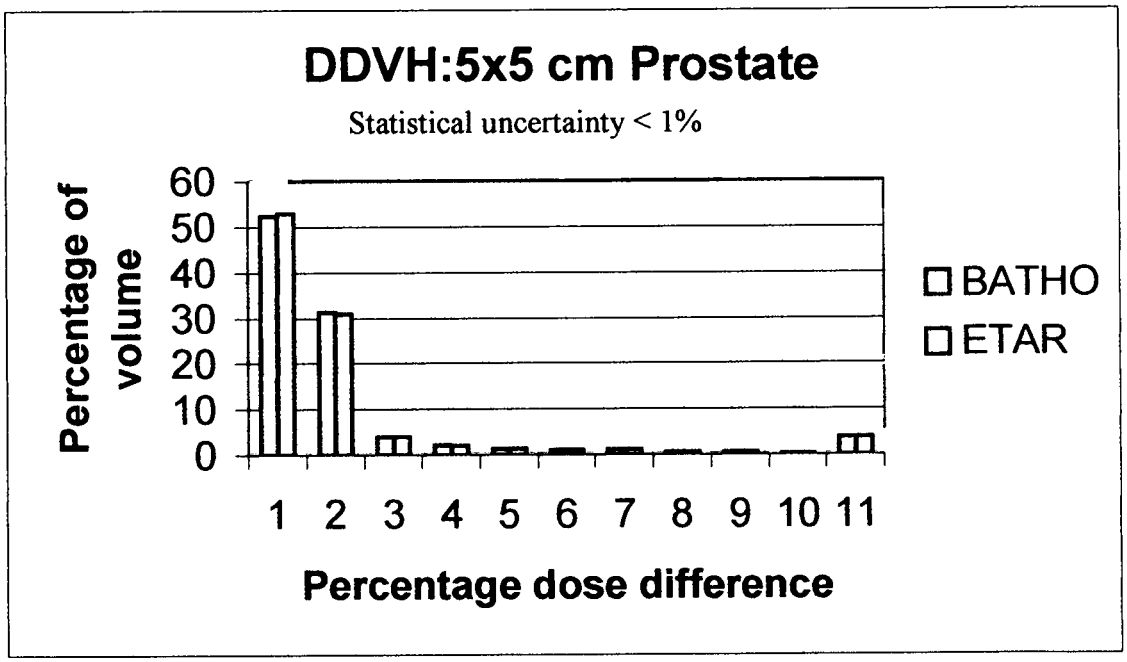

Figure 7.48 Dose difference volume histogram for the 5x5 cm^2 open x-ray field in the prostate patient model.

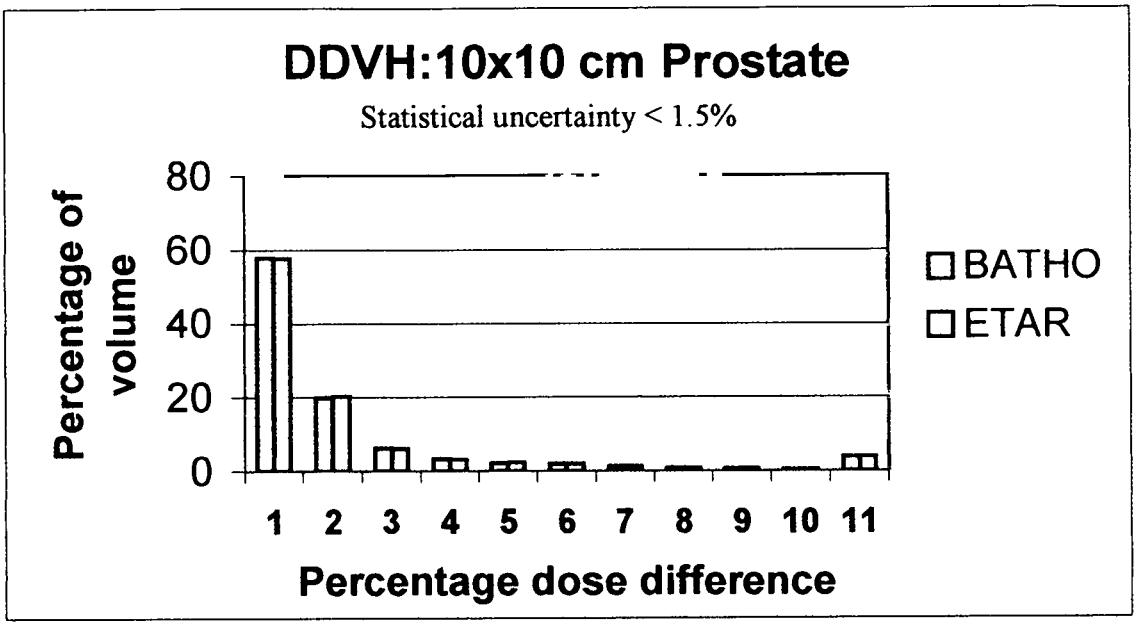

Figure 7.49 Dose difference volume histogram for the 10x10 cm^2 open x-ray field in the prostate patient model.

7.1.5.2 Percentage depth dose curves

Figures 7.50 – 7.58 show central-axis depth dose curve comparisons between the Batho, ETAR and DOSXYZ dose calculation methods.

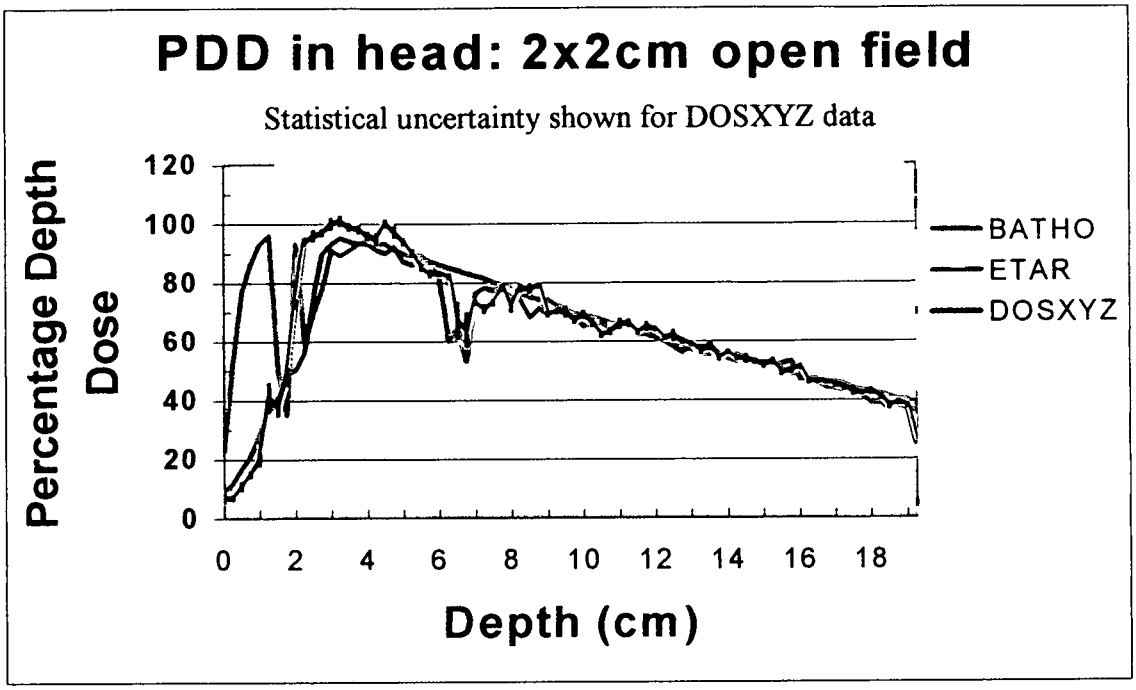

Figure 7.50 Percentage depth dose curves along the central field axis for the 2x2 cm^2 open field in the head patient model. The dose uncertainty for the DOSXYZ calculations are indicated by error bars

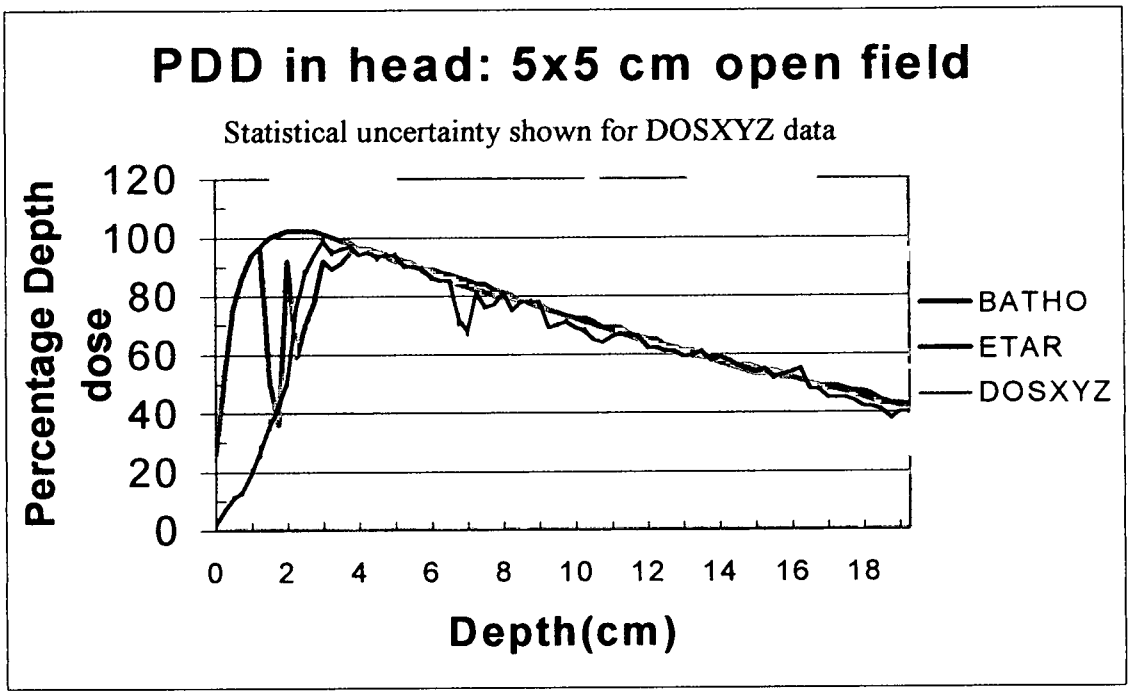

Figure 7.51 Percentage depth dose curves along the central field axis for the 5x5 cm^2 open field in the head patient model. The dose uncertainty for the DOSXYZ calculations are indicated by error bars

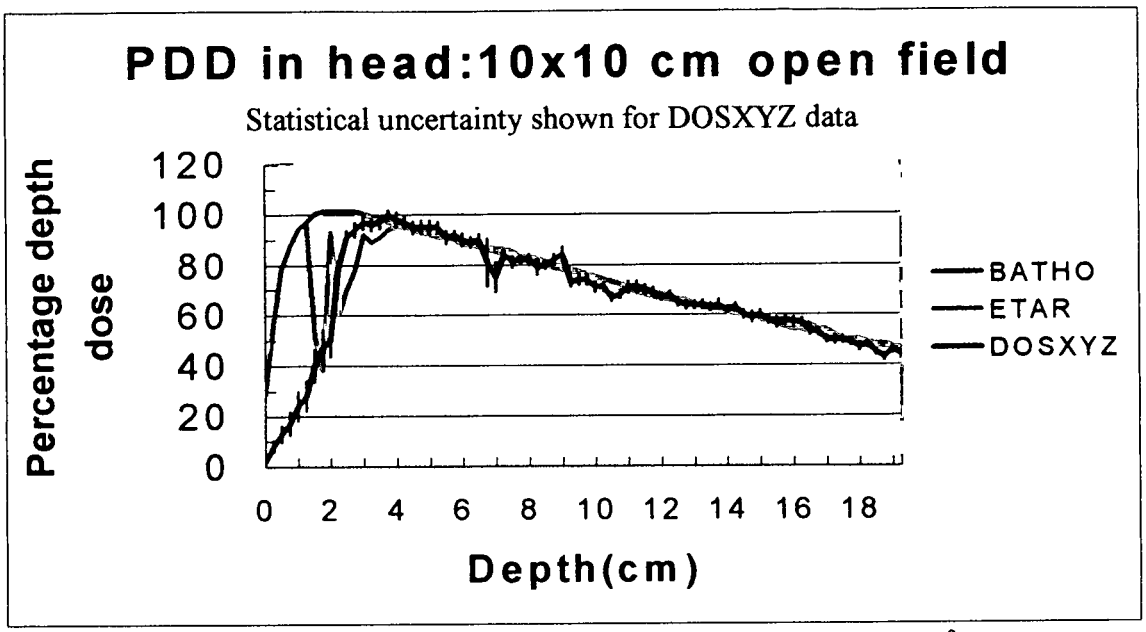

Figure 7.52 Percentage depth dose curves along the central field axis for the 10x10 cm^2 open field in the head patient model. The dose uncertainty for the DOSXYZ calculations are indicated by error bars

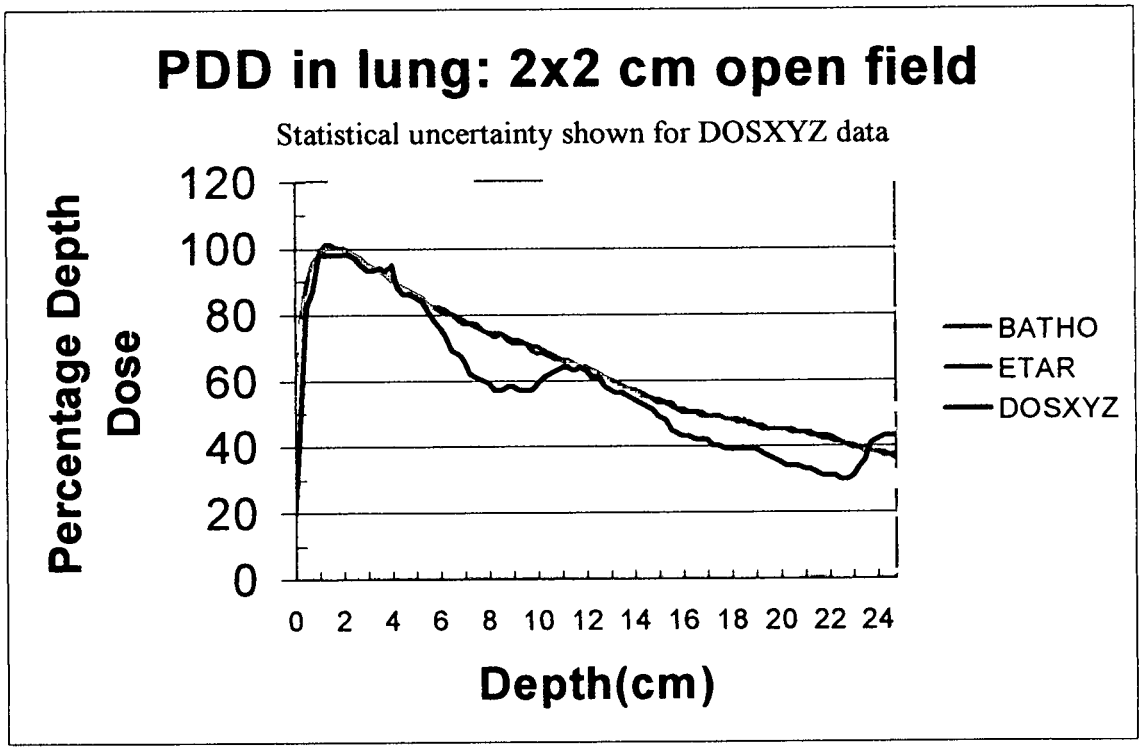

Figure 7.53 Percentage depth dose curves along the central field axis for the 2x2 cm^2 open field in the lung patient model. The dose uncertainty for the DOSXYZ calculations are indicated by error bars

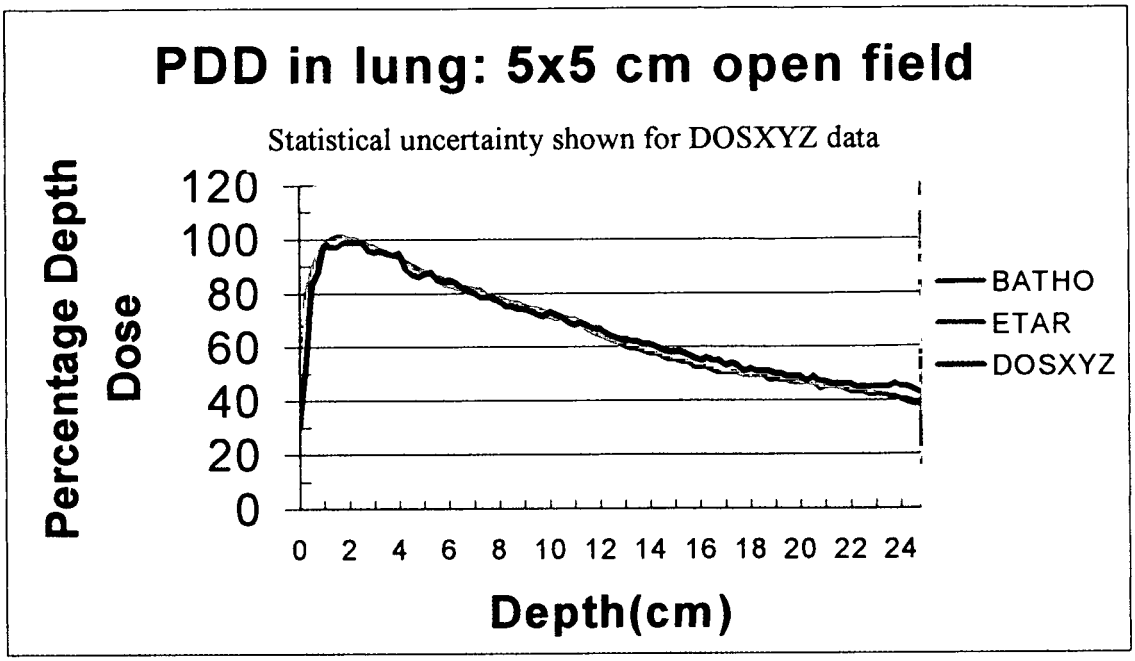

Figure 7.54 Percentage depth dose curves along the central field axis for the 5x5 cm^2 open field in the lung patient model. The dose uncertainty for the DOSXYZ calculations are indicated by error bars

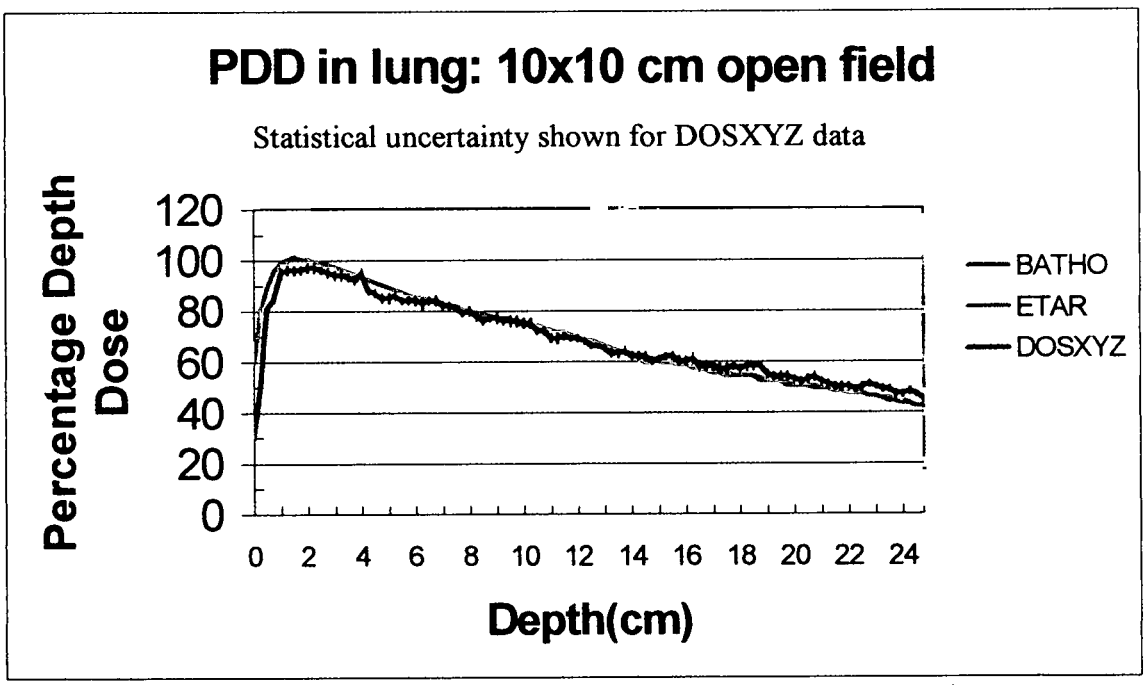

Figure 7.55 Percentage depth dose curves along the central field axis for the 10x10 cm^2 open field in the lung patient model. The dose uncertainty for the DOSXYZ calculations are indicated by error bars

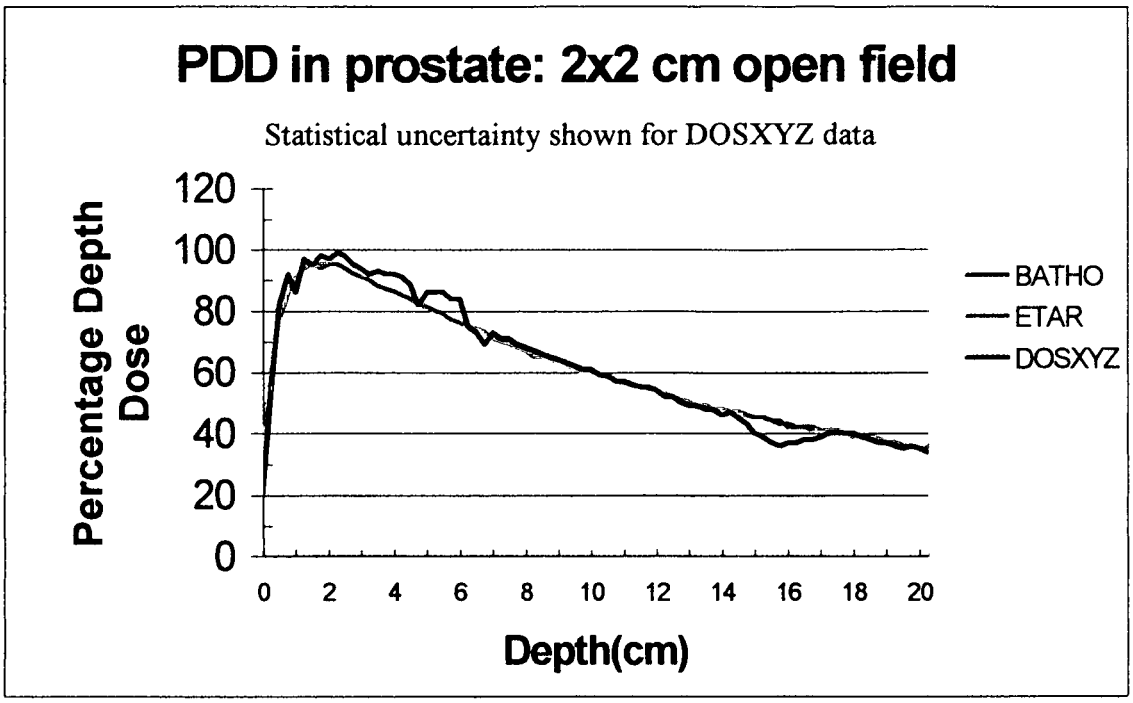

Figure 7.56 Percentage depth dose curves along the central field axis for the 2x2 cm^2 open field in the prostate patient model. The dose uncertainty for the DOSXYZ calculations are indicated by error bars

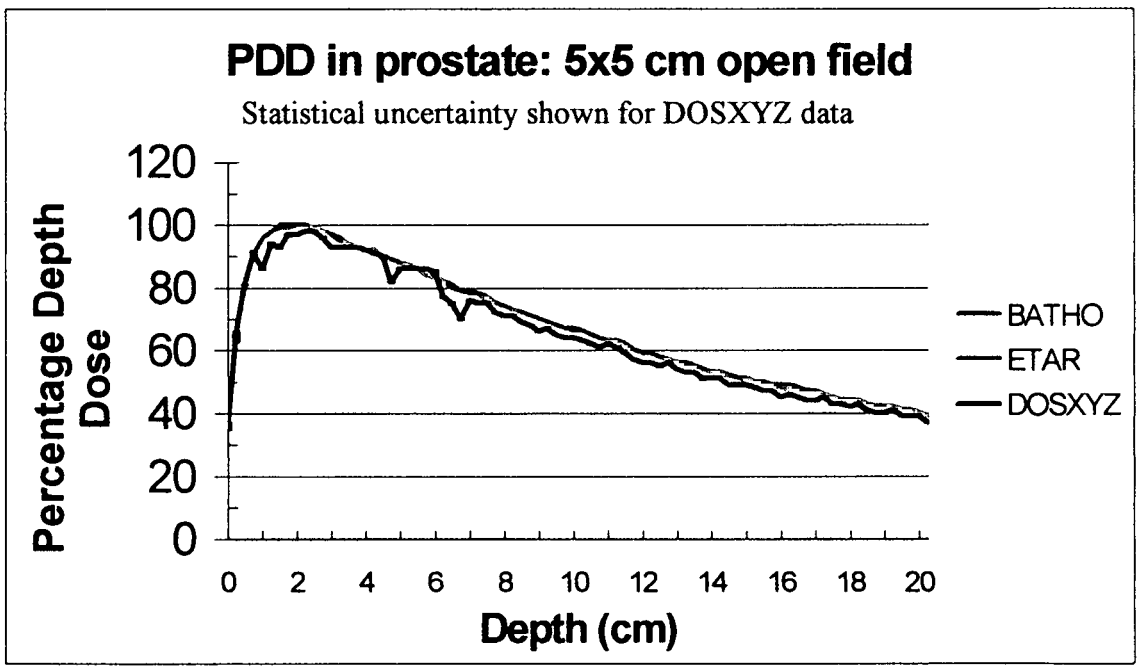

Figure 7.57 Percentage depth dose curves along the central field axis for the 5x5 cm open field in the prostate patient model. The dose uncertainty for the DOSXYZ calculations are indicated by error bars

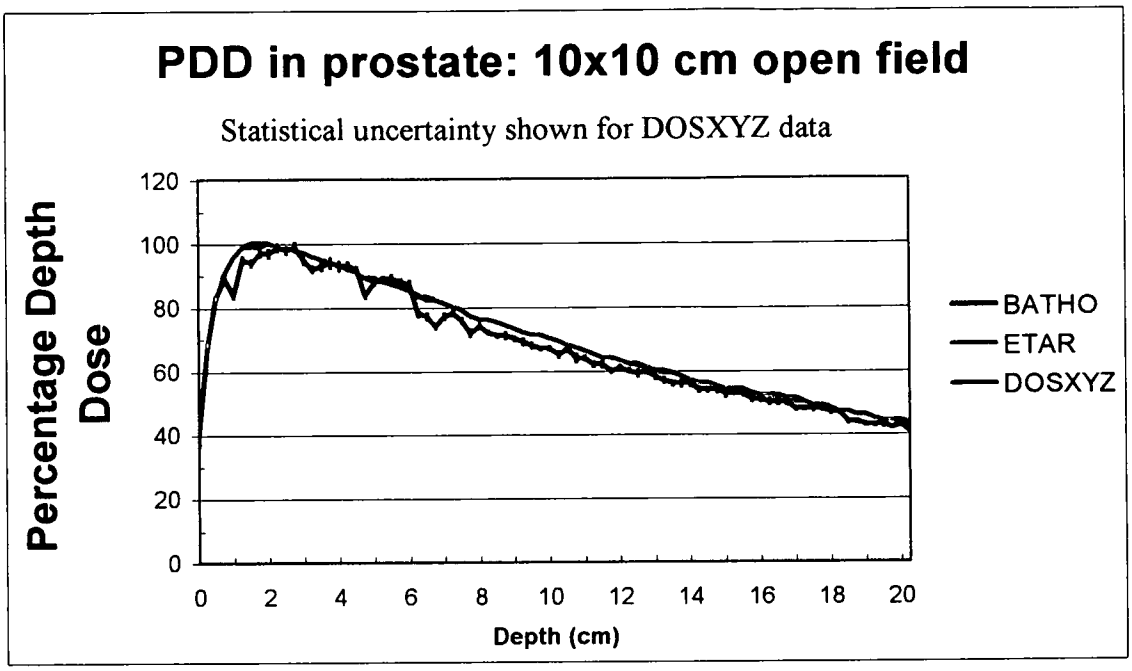

Figure 7.58 Percentage depth dose curves along the central field axis for the 5x5 cm open field in the prostate patient model. The dose uncertainty for the DOSXYZ calculations are indicated by error bars

7.1.5.3 Dose distributions

7.1.5.3.1 Open fields

The results shown here were produced using the IDL image processing code. The absorbed dose distributions were contoured at the 10, 30, 50, 70, 90 and 100 percent dose levels. These contour plots (isodose plots) were superimposed on the particular patient models and were stored in files in a bitmap format. In each set of images the isodose contours are shown in the order of BATHO, ETAR and DOSXYZ dose calculation methods for the head, lung and prostate patient models.

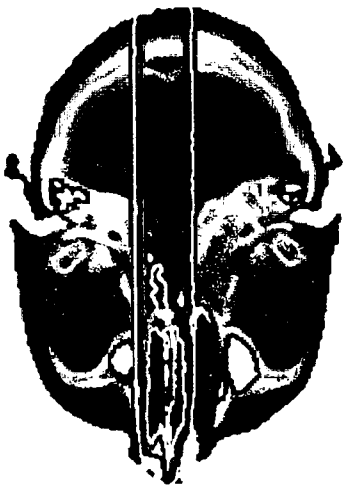

Figure 7.59

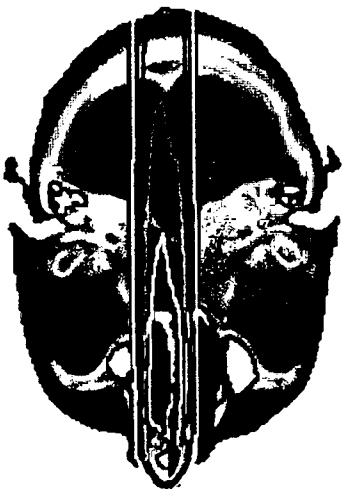

Figure 7.60

The dose distributions calculated with the BATHO algorithm (figure 7.59) and the ETAR algorithm (figure 7.60) for a 2x2 cm^2 open x-ray field in the head model. The isodose curves shown: 10 percent = white, 30 percent = red, 50 percent = light blue, 70 percent = yellow, 90 percent = dark blue and 100 percent = green.

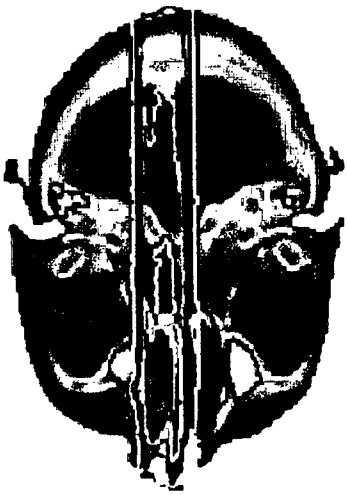

Figure 7.61

Figure 7.61 The dose distribution calculated with the DOSXYZ algorithm for a 2x2 cm^2 open x-ray field in the head model. The isodose curves shown are represented by 10 percent = white, 30 percent = red, 50 percent = light blue, 70 percent = yellow, 90 percent = dark blue and 100 percent = green.

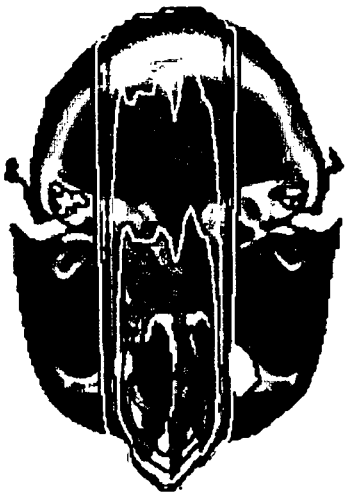

Figure 7.62

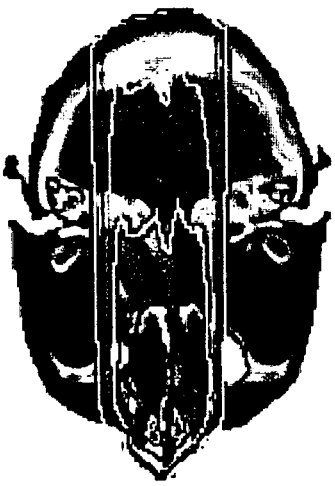

Figure 7.63

The dose distributions calculated with the BATHO algorithm (figure 7.62) and the ETAR algorithm (figure 7.63) for a 5x5 cm^2 open x-ray field in the head model. The isodose curves shown: 10 percent = white, 30 percent = red, 50 percent = light blue, 70 percent = yellow , 90 percent = dark blue and 100 percent = green.

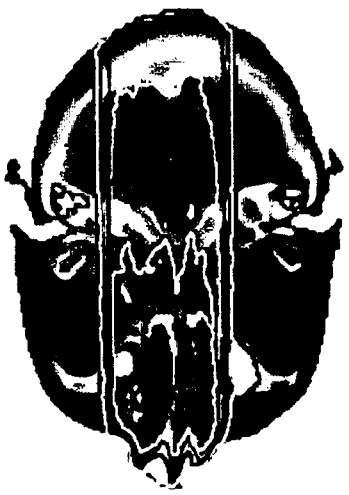

Figure 7.64

Figure 7.64 The dose distribution calculated with the DOSXYZ algorithm for a 5x5 cm^2 open x-ray field in the head model. The isodose curves shown are represented by 10 percent = white, 30 percent = red, 50 percent = light blue, 70 percent = yellow, 90 percent = dark blue and 100 percent = green.

Figure 7.65

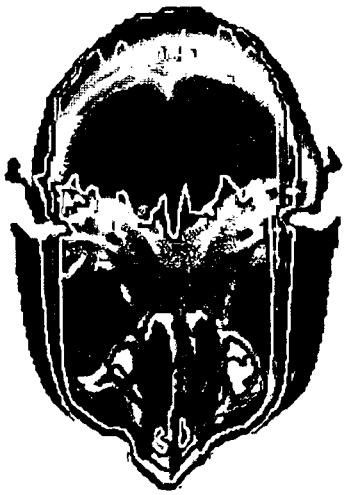

Figure 7.66

The dose distributions calculated with the BATHO algorithm (figure 7.65) and the ETAR algorithm (figure 7.66) for a 10x10 cm^2 open x-ray field in the head model. The isodose curves: 10 percent = white, 30 percent = red, 50 percent = light blue, 70 percent = yellow , 90 percent = dark blue and 100 percent = green.

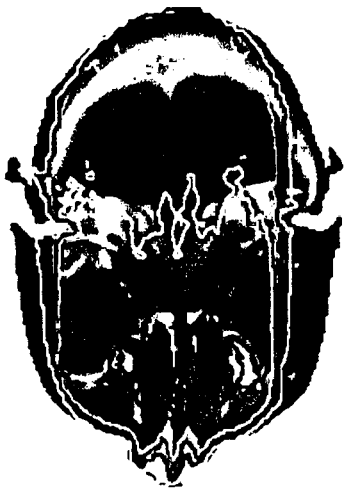

Figure 7.67

Figure 7.67 The dose distribution calculated with the DOSXYZ algorithm for a 10x10 cm^2 open x-ray field in the head model. The isodose curves: 10 percent = white, 30 percent = red, 50 percent = light blue, 70 percent = yellow, 90 percent = dark blue and 100 percent = green.

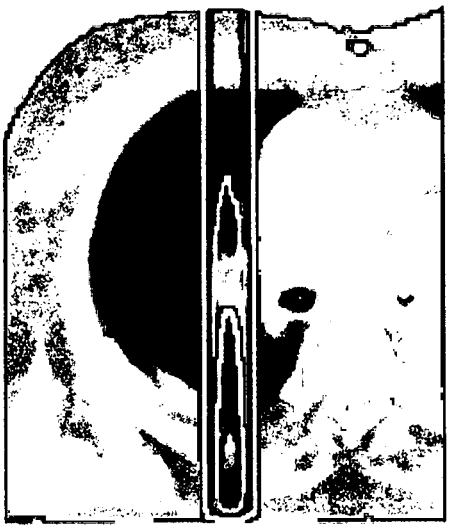

Figure 7.68

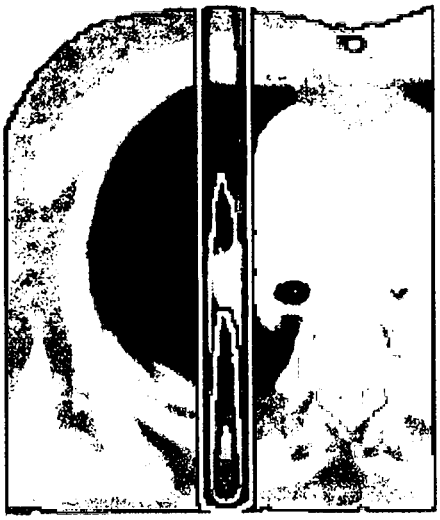

Figure 7.69

The dose distributions calculated with the BATHO algorithm (figure 7.68) and the ETAR algorithm (figure 7.69) for a 5x5 cm^2 open x-ray field in the lung model. The isodose curves: 10 percent = white, 30 percent = red, 50 percent = light blue, 70 percent = yellow, 90 percent = dark blue and 100 percent = green.

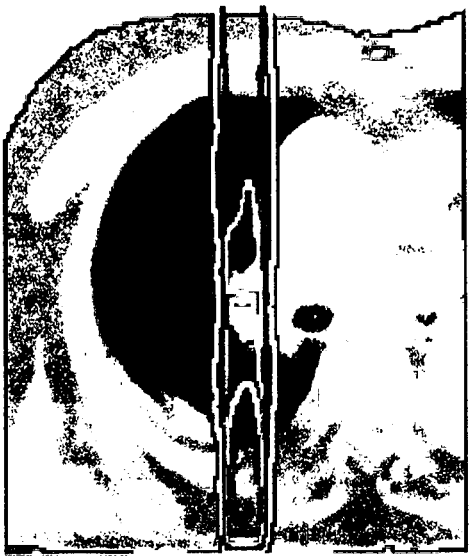

Figure 7.70

Figure 7.70 The dose distribution calculated with the DOSXYZ algorithm for a 2x2 cm^2 open x-ray field in the lung model. The isodose curves shown are represented by 10 percent = white, 30 percent = red, 50 percent = light blue, 70 percent = yellow, 90 percent = dark blue and 100 percent = green.

Figure 7.71

Figure 7.72

The dose distributions calculated with the BATHO algorithm (figure 7.71) and the ETAR algorithm (figure 7.72) for a 5x5 cm^2 open x-ray field in the lung model. The isodose curves: 10 percent = white, 30 percent = red, 50 percent = light blue, 70 percent = yellow, 90 percent = dark blue and 100 pecent = green.

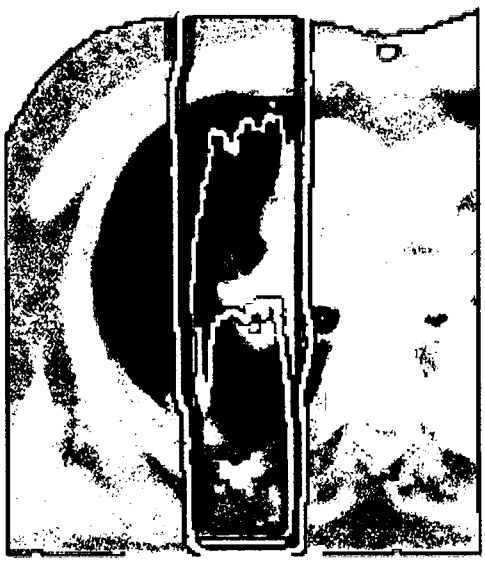

Figure 7.73

Figure 7.73 The dose distribution calculated with the DOSXYZ algorithm for a 5x5 cm^2 open x-ray field in the lung model. The isodose curves shown are represented by 10 percent = white, 30 percent = red, 50 percent = light blue, 70 percent = yellow, 90 percent = dark blue and 100 percent = green.

Figure 7.74

Figure 7.75

The dose distributions calculated with the BATHO algorithm (figure 7.74) and the ETAR algorithm (figure 7.75) for a 10x10 cm^2 open x-ray field in the lung model. The isodose curves: 10 percent = white, 30 percent = red, 50 percent = light blue, 70 percent = yellow, 90 percent = dark blue and 100 pecent = green.

Figure 7.76

Figure 7.76 The dose distribution calculated with the DOSXYZ algorithm for a 10x10 cm^2 open x-ray field in the lung model. The isodose curves shown are represented by 10 percent = white, 30 percent = red, 50 percent = light blue, 70 percent = yellow, 90 percent = dark blue and 100 percent = green.

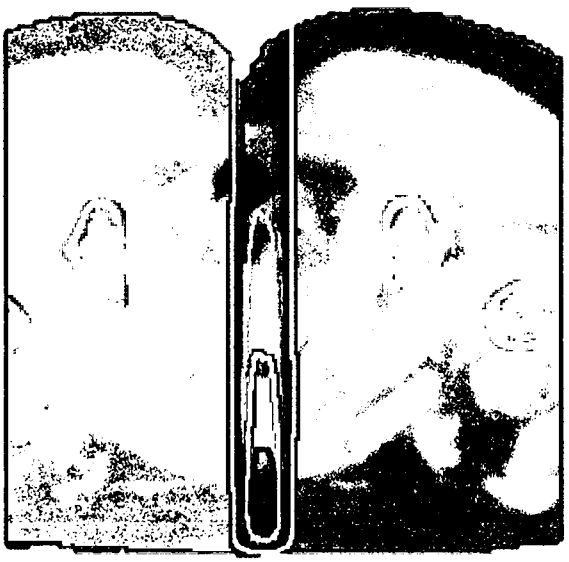

Figure 7.77

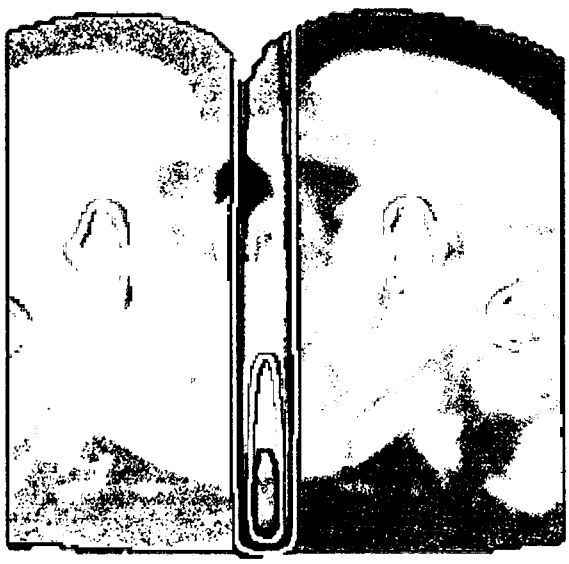

Figure 7.78

The dose distributions calculated with the BATHO algorithm (figure 7.77) and the ETAR algorithm (figure 7.78) for a 2x2 cm^2 open x-ray field in the prostate model. The isodose curves: 10 percent = white, 30 percent = red, 50 percent = light blue, 70 percent = yellow, 90 percent = dark blue and 100 pecent = green.

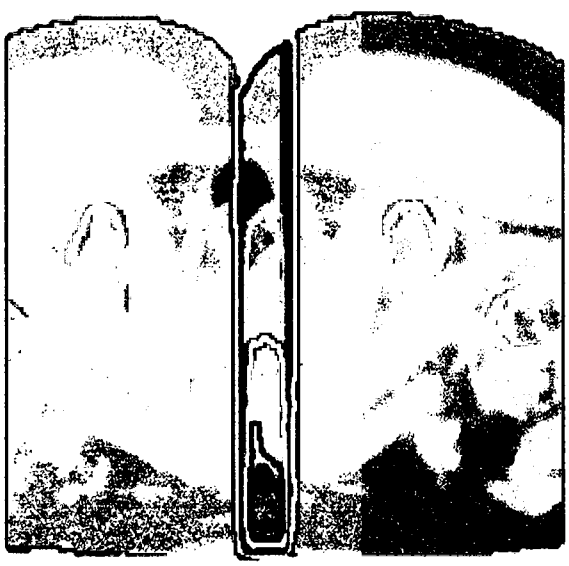

Figure 7.79

Figure 7.79 The dose distribution calculated with the DOSXYZ algorithm for a 2x2 cm^2 open x-ray field in the prostate model. The isodose curves shown are represented by 10 percent = white, 30 percent = red, 50 percent = light blue, 70 percent = yellow, 90 percent = dark blue and 100 percent = green.

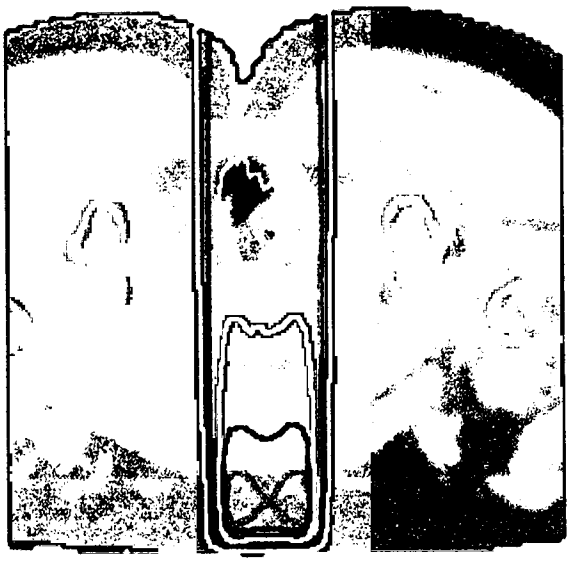

Figure 7.80

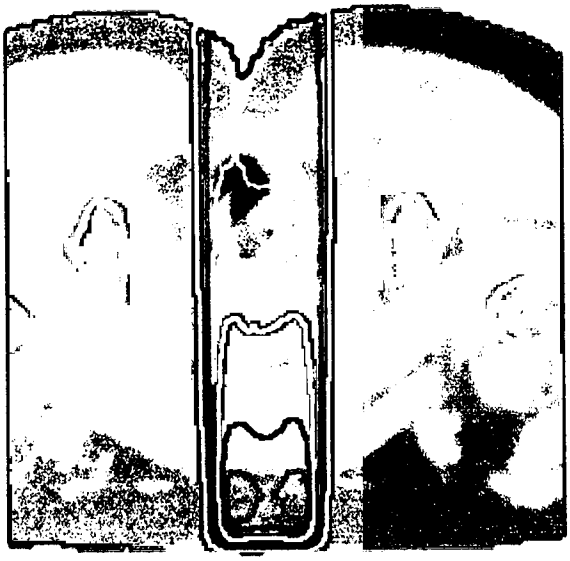

Figure 7.81

The dose distributions calculated with the BATHO algorithm (figure 7.80) and the ETAR algorithm (figure 7.81) for a 5x5 cm^2 open x-ray field in the prostate model. The isodose curves: 10 percent = white, 30 percent = red, 50 percent = light blue, 70 percent = yellow, 90 percent = dark blue and 100 pecent = green.

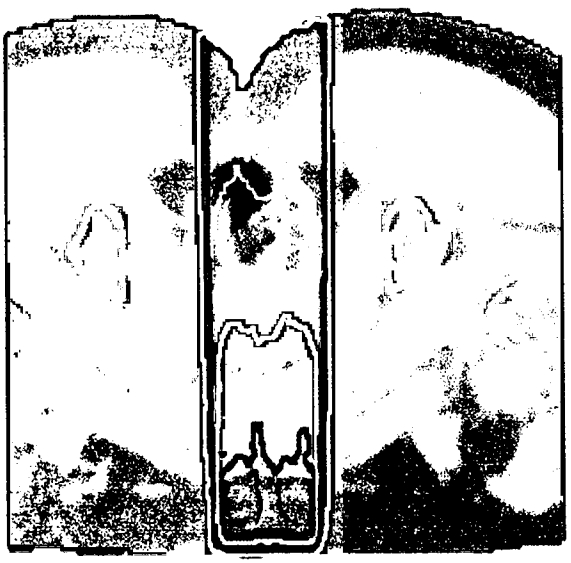

Figure 7.82

Figure 7.82 The dose distribution calculated with the DOSXYZ algorithm for a 5x5 cm^2 open x-ray field in the prostate model. The isodose curves shown are represented by 10 percent = white, 30 percent = red, 50 percent = light blue, 70 percent = yellow, 90 percent = dark blue and 100 percent = green.

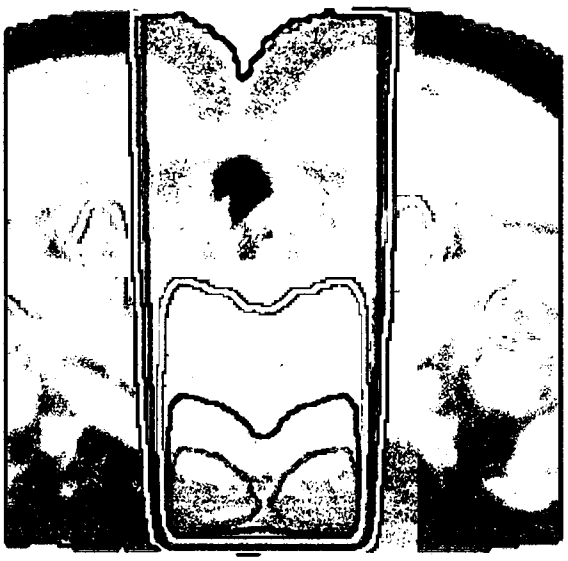

Figure 7.83

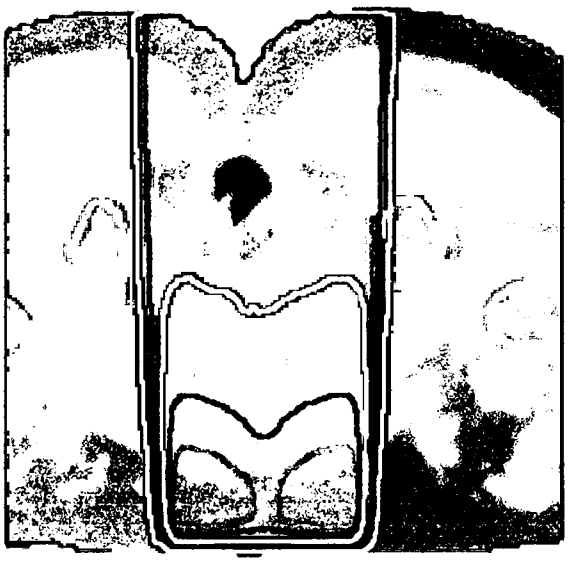

Figure 7.84

The dose distributions calculated with the BATHO algorithm (figure 7.83) and the ETAR algorithm (figure 7.84) for a 10x10 cm^2 open x-ray field in the prostate model. The isodose curves: 10 percent = white, 30 percent = red, 50 percent = light blue, 70 percent = yellow, 90 percent = dark blue and 100 pecent = green.

Figure 7.85

Figure 7.85 The dose distribution calculated with the DOSXYZ algorithm for a 10x10 cm^2 open x-ray field in the prostate model. The isodose curves shown are represented by 10 percent = white, 30 percent = red, 50 percent = light blue, 70 percent = yellow, 90 percent = dark blue and 100 percent = green.

7.1.5.3.2 Wedged fields

In this section the DDVH, PDD curve and a 2D-dose distribution for a 5x5 cm^2 wedged field are presented. This distribution shows an example of the combinations of two wedged beams perpendicular to each other. The 2D dose distribution is shown in figs. 7.88 to 7.90 The distribution in figure 7.90 was calculated in the DOSXYZ code by simulating the each beam's dose distribution separately. The resulting two dose matrices were added to combine these fields. The beam entrance and wedge orientation is shown in this figure. This example shows how actual treatment planning protocols could be recalculated with the DOSXYZ code for a full dose distribution evaluation.

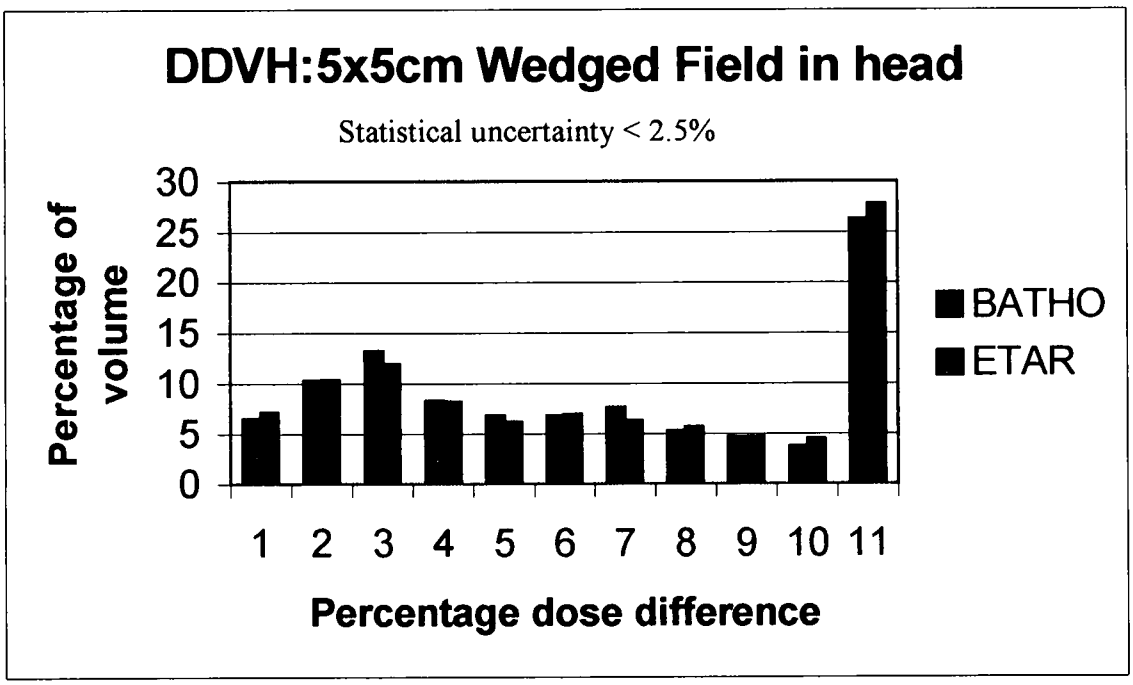

Figure 7.86 The DDVH for the 5x5cm^2 wedged fields in the HEAD phantom.

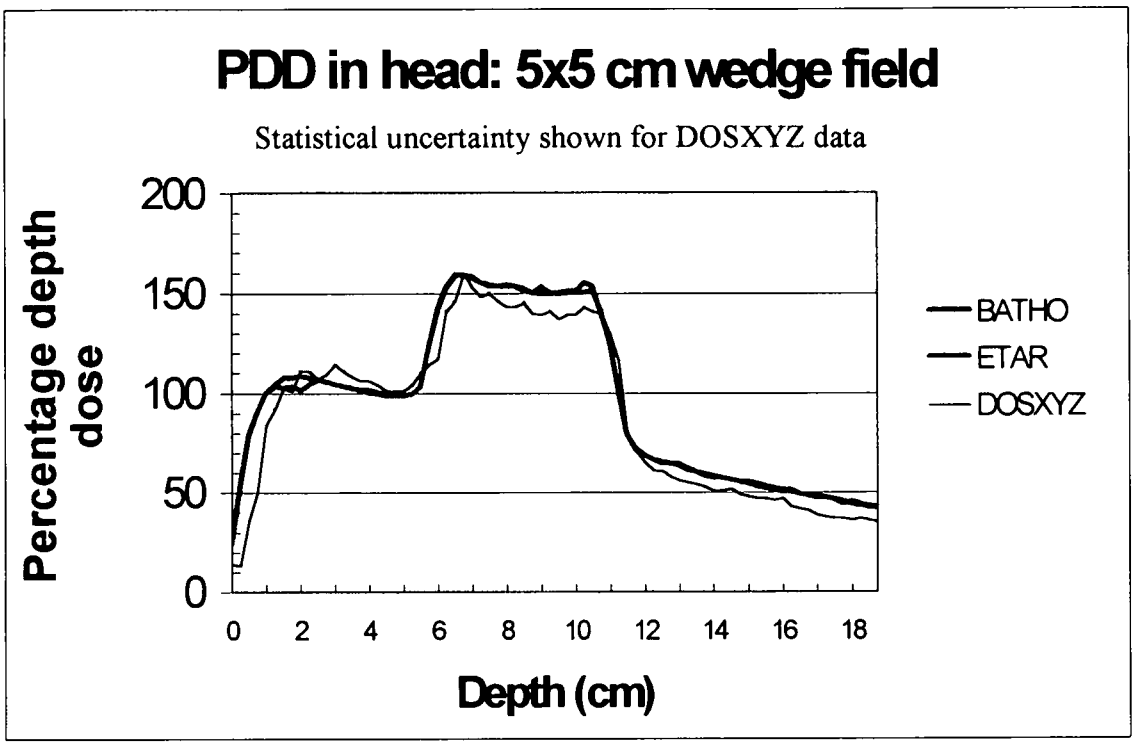

Figure 7.87 The Percentage depth dose curves for the 5x5 cm^2 perpendicular wedged fields in the Head phantom. The depth dose w evaluated along the same central axis for the 5x5 cm^2 open field in the Head phantom.

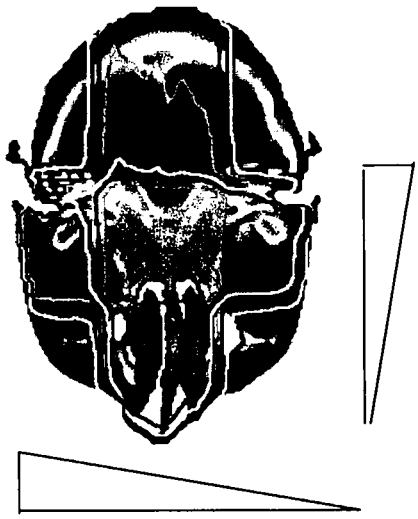

Figure 7.88

Figure 7.89

The dose distributions calculated with the BATHO algorithm (figure 7.88) and the ETAR algorithm (figure 7.89) for two perpendicular 5x5 cm^2 cm wedged x-ray field in the head model. The isodose curves shown are represented by 10 percent = white, 30 percent = red, 50 percent = light blue, 70 percent = yellow, 90 percent = dark blue and 120 percent = green.

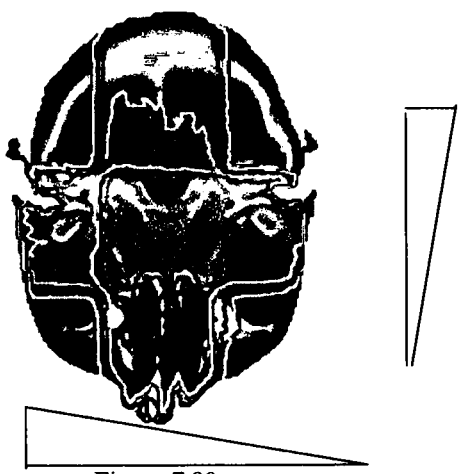

Figure 7.90

Figure 7.90 The dose distribution calculated with the DOSXYZ algorithm for two perpendicular 5x5 cm^2 cm wedged x-ray field in the head model. The isodose curves shown are represented by 10 percent = white, 30 percent = red, 50 percent = light blue, 70 percent = yellow, 90 percent = dark blue and 120 percent = green.

CHAPTER 8

DISCUSSION

In this chapter the results presented in chapter 7 will be discussed.

8.1 Phase space file data

The first step towards obtaining beam data from Monte Carlo simulations is to create a generic accelerator. In this study the accelerator was built and compiled with the BEAM code in two steps. In the first step the fixed accelerator components were modeled as described in the methods of Chapter 6. In this stage a large 'master' PSF was scored in a plane just above the accelerator jaws. The BEAMDP program was used to analyze the PSF. Figure 7.1 shows the energy fluence profile in the x-direction. The bin width was chosen as 2 mm. The statistical uncertainties in this graph are not distinguishable from the graph itself and are well below the one percent level. An important feature of this graph is the fact that the energy fluence increases towards the rapid fall off at the edges, with a local minimum at x = 0, or the PSF origin. The shape of this profile clearly reflects the influence of the flattening filter on the forward peaked brehmstrahlung fluence from the target. This will have an important effect on the dose profiles as obtained with DOSXYZ in phantoms. Figure 7.2 shows the energy spectrum of the photons in the master PSF. The energy bins have a width of 0.5 MeV and range from 0 to 8 MeV. It clearly is a typical 8 MV thick target brehmstrahlung energy spectrum. Figure 7.3 shows the energy fluence profile derived from the 5x5 cm^2 open field PSF at an SSD of 100 cm. A total of 20 bins were chosen with a width of 5 mm. The statistical uncertainties were within one percent. In this graph it is observed that the energy fluence for this field is not symmetric about the central axis. There is a variation of 4 to 5 percent in the energy fluence. Close inspection of figure 7.1 shows that the fluence is not perfectly symmetric at points around the origin (x = 0) of the PSF. This effect is enhanced in the 5x5 cm^2 x-ray beam PSF. This effect is probably caused by the statistical variation in the fluence in

the small area width of 2 mm that was chosen in the 'master' phase space file for the fluence analysis.

This observation does not have an important impact on the objective of this study. Since the PSF is used more than once, the particles in the PSF were redistributed in the DOSXYZ code for the open fields. This would have the effect of symmetrizing the open field dose distributions.

In figure 7.4 the energy fluence of the photons for a 5x5 cm^2 wedged field is shown. This fluence profile was obtained from the wedged field PSF using the BEAMDP program. In this graph the same bin dimensions are used as in figure 7.3. Due to the shape of the energy fluence profile in the master PSF, its effect is to enhance the fluence profile in the negative x-direction. This enhancement counteracts the influence of the attenuation of the fluence by the wedge. The result is a nearly flat energy fluence profile. At the area where the wedge angle tends to become horizontal at the edge of the negative x-direction the increase in fluence is a direct result of the shape of the 'master' PSF energy fluence. There the energy fluence increases resulting in counteracting the attenuation in the wedge. Thus the gradient of the shape of the wedge energy fluence is not a typical wedge energy fluence that one would expect for flat fields where the fluence would monotonically decrease from the thin to the thick side of the wedge. The statistical uncertainty in this PSF was also within a one percent standard deviation.

8.2 Dose profiles for the TPS

8.2.1 Open fields

In order to evaluate the TPS it must be configured first with input beam data based on dose distributions for various square field sizes in water. This is necessary for the treatment planning system to enable it to calculate beam profiles and dose distributions in arbitrary models and field sizes. The set of data shown in figures 7.5 to 7.11 show the dose profiles for various open field dimensions. These dose distribution data were calculated with the DOSXYZ Monte Carlo code. The grid spacing of the data points was

0.5 cm. In each figure dose profiles at depths of 2, 5, 10, 15 and 25 cm are shown. The treatment planning system uses this input data for its x-ray beam model construction. Note the increase in the absorbed dose near the field edges, which is due to the shape of the master PSF energy fluence profile being propagated into the subsequent open beam PSF's at 100 cm SSD. This effect is more pronounced at the larger field sizes. Figure 7.12 shows the normalized percentage depth dose curves for each field size. This data are also required by the TPS to construct its photon beam models. In all cases the statistical uncertainties were less than one percent and are omitted from the graphs to prevent a line marker forest.

8.2.2 Wedged fields

For the wedged beams, beam profiles and percentage depth dose curves were generated with the DOSXYZ code for the same field sizes and depths as for the open beams. These are shown in figures 7.13 – 7.20. The wedge data profiles for the 2x2 and 3x3 cm^2 fields show a close resemblance to what one expects from the shape of the wedge shown in figure 6.2, Chapter 6. It is initially flat and its gradient becomes steeper in a stepwise manner towards its sharp edge. The energy fluence profile of the 'master' PSF is shown in figure 7.1. If this energy fluence were transmitted through the wedge, the dose profile would be expected to increase near the edges. For the wedge fields with dimensions of 4x4 cm^2 and larger the wedged dose profile loses its 45 degree slope, in contrast to what is expected of this type of wedge, because of the shape of the energy fluence profile in the master PSF. This corresponds with what is observed, especially for the larger fields.

8.3 Verification of TPS input beam data

When new beam data are entered into a TPS an important task of quality assurance is to make sure that the entered beam data are correctly and accurately reproduced by the TPS. In this study dose distributions in patient models were calculated for 2x2, 5x5 and 10x10 cm^2 photon fields. Figures 7.21 to 7.32 shows the dose profiles and percentage depth

dose curves calculated by the TPS in a water phantom for 2x2, 5x5 and 10x10 cm^2 open and wedged fields. The broken lines represent the CADPLAN data that are compared to the DOSXYZ dose profile data (solid lines) at depths of 2, 5, 10, 15 and 25 cm. For the open beam data it is clear that the agreement between the TPS (CADPLAN) and the DOSXYZ dose profiles, that is the originally entered beam data, agree well within a margin of about one percent. The reason for these small differences between the entered and calculated dose profiles is that the TPS fits curves to the input data and this smooth the original raw beam data. Similarly accurate reproduction of the input beam data are evident.

Thus, it has been established that the agreement between the photon beam data base in the TPS and the original raw data are accurate at the one percent level and this data base can be used to test the TPS's dose calculation algorithms against more general dose distributions calculated with the DOSXYZ code.

There are however discrepancies in the order of 8 percent in the buildup regions for the percentage depth dose curves in figures 7.28, 7.30 and 7.32. Here the CADPLAN reproduces the percentage depth dose as higher values when compared with the DOSXYZ generated data. This is only significant up to a depth of 3 cm for the wedged beams. At deeper depths the agreement is within one percent. The highest discrepancy is on the surface of the water phantom. The difference between the percentage dose values converges to three percent at a depth of 2 cm. Thus the effect is only significant near the phantom surface.

8.4 The transformation of CT based patient models into a format suitable for DOSXYZ

In chapters 6 and 7 the reason and method for transforming CT data into a format suitable for the DOSXYZ Monte Carlo code were described respectively. The method employed a histogram structure for associating CT numbers in a given interval with certain materials. This is quite valid to do in the context of TPS dose calculation evaluation as long as the

CT images in the TPS are binned correspondingly to discrete CT values before dose calculations are made with the TPS. In figures 7.33 to 7.35 a series of percentage depth dose difference curves are shown. These curves describe the deviation of the depth dose of a certain tissue type from that of water as a function of the phantom thickness. From figure 7.33 it can be observed that certain groups of soft tissues display very similar dose difference characteristics as a function of depth. If all tissues with dose differences within one percent of each other are grouped together, a dosimetrically equivalent tissue subset is formed. These subsets are shown in table 7.1 From this table it is clear that some subsets contain more than one tissue type e.g. subset 4 contains brain, breast, pancreas and red marrow. This means that their depth dose difference curves correspond within one percent.

The above results imply that if a DOSXYZ patient model is constructed from a CT image, then all tissues with CT numbers lying within the interval from 1011 to 1040 could be associated with any one of the four tissue types in group 4. The absorbed dose would be the same within one percent for organs with thickness less than 20 cm. The maximum allowable CT number interval for each group of tissues was determined from the percentage depth dose difference data as follows: In figures 7.36 to 7.38 the graphs of the percentage dose difference against CT number are shown. This data were plotted at different depths namely 5, 10, 15 and 20 cm. Figure 7.39 shows plots of the inverse slopes of these lines against organ thickness. The minimum values of these graphs were used to determine the maximum CT number intervals for discretizing the CT image data into bins. Thus the widths of the CT number intervals were chosen as 30 HU for lung and soft tissue and 100 for bone.

From the percentage dose difference data in figure 7.33 it can be observed that water is in a group of its own, indicating that its electron density differs from other tissues to such an extent that the dose differs by more than one percent. Thus it is seen that for larger organs the cumulative effect of the different electron densities of soft tissues to water on the photon fluence alters the depth dose differences to values larger than one percent. For larger organs it would be incorrect to assume that tissues are water-like when dose

differences at the one percent level were to be detected. On the 3 percent level it would be quite valid to assume water and tissue equivalence in terms of depth dose. From table 7.1 it is observed that tissues in the same group also have calculated CT numbers that lie within a CT number interval. E.g. in group 4 brain, breast, pancreas and red marrow have calculated CT numbers that lie within the interval 1011 to 1041, as calculated from their respective electronic densities with an empirical bilinear function. These tissues display dosimetric equivalence at the one percent level. There is a strong correlation between the electron density of a material and its depth dose. Tissues with similar electron densities have similar depth dose curves. This is attributed to the Compton interaction process that accounts for 97 percent to 98 percent of all photon interactions for a typical 8 MV photon beam. The remainder is mostly pair production interactions. The former interaction depends only on the electron density and the latter more on the effective atomic number of tissue types. In figure 7.36 the effects of differences in pair production on the depth dose difference can be observed as a spread in the dose values around the regression line. Note this for tissues with the same electron density that would thus have the same Compton cross-section but different effective atomic numbers. It can be seen that these effects are within the one percent dose level. Thus by binning the tissues discretely at the one percent level, the effects of pair production can be ignored.

One implication of this method of assigning materials to tissues is that a tissue belonging to a certain group, but having a slightly larger density, will have a higher CT number, which may put it in the next group. It would thus be identified as a different tissue. Since the Compton effect dominates the interactions, the only concern is the effect of the pair production process at these energies, since the new tissue with which the original tissue is associated, may have a different effective atomic number. From figure 7.36 it is seen that in the worst case the dose perturbation would be about 0.5 percent.

Some of the CT number intervals shown in table 7.1 are associated with a group of tissues. In order to use this data in Monte Carlo applications, one tissue out of each group was chosen and is listed in table 7.2 together with its atomic composition and physical density. These tissues were used to set up a PEGS4 data file containing 57 discrete tissue

types. Tissues with CT numbers less than 20 were considered as air with a zero CT number assignment. Twenty-one types of cortical bone were constructed together with 31 types of lung and 5 soft tissue types. The total CT number range was between 0 and 3000 CT number units to conform with the convention used by the CADPLAN TPS. This range is chosen such that air has a CT number of zero and hard bone 3000. The conversion from Hounsfield numbers to CADPLAN numbers was done through the relation:

$$\text{CT number (CADPLAN)} = \text{CT number (Hounsfield units)} + 1000 \qquad 8.1$$

Where the CT number in Hounsfield units for air is –1000 HU and water is 0 HU.

The histogram like manner of material assignment in this study fits in with the fact that CT images have a noise level of about 10 – 15 HU. The CT number intervals have a range of 30 HU for soft tissue and lung and 100 HU for hard bone. The bin widths are thus wider than the noise level, but this is not expected to alter the dose in our patient models by more than one percent. For treatment planning dose calculation purposes this would work well provided, as mentioned earlier, that the CT image used as the TPS patient model is also discretized as was done in this study.

8.4.1 Conversion of electron density to CT number

The conversion of electron density to CT number was performed using a bilinear function. The method of obtaining this function is described in section 6.4.2. This function depends on the type of CT scanner that is used, and should be obtained for each specific CT scanner. Therefore the CT number intervals e.g. 30 HU for soft tissue and 100 HU for bone found in this study could differ for other CT scanners and should not be used indiscriminately.

8.5 Comparison between the dose distributions calculated by DOSXYZ and by the TPS for the BATHO and ETAR dose calculation algorithms

8.5.1 Dose difference volume histograms (DDVH's)

The procedure for the normalization of the DOSXYZ generated dose distributions was explained in section 6.7.1. Figures 7.41 - 7.49 show dose difference volume histogram data in the three patient models for the 2x2, 5x5 and 10x10 cm^2 open fields. These data were calculated by comparing the dose for the BATHO and ETAR algorithms with the corresponding DOSXYZ dose distributions on a voxel by voxel basis. A spectrum of the number of voxels, expressed as a percentage of the dose volume, against its percentage dose difference was calculated. In these graphs the last bin has a value of 11. All voxels that differ in dose with values larger than 10 percent are accumulated in this bin. These data give an overall impression of the performance of the ETAR and BATHO dose calculation methods against the DOSXYZ golden standard.

8.5.1.1 Head model (maxillary sinus)

Figure 7.41 shows that the BATHO method gives more accurate dose calculation results than the ETAR method. This can be observed by the fact that the BATHO spectrum is higher for the 1 to 2 percent dose differences with a lower bin value for dose differences larger than 10 percent (bin no 11). In the range 3 to 10 percent these two algorithms have the same performance. In figure 7.42 the ETAR method gives results more similar to the BATHO method for the 5x5 cm^2 open x-ray field. Figure 7.43 suggests the same but this time it can be seen that the percentage of the volume giving dose differences less than 2 percent is about 50 percent less for the 10x10 cm field. For dose differences larger than 10 percent the values for the 10x10 and 5x5 cm^2 fields are virtually the same. There is also a more gradual drop in the spectrum for higher dose differences. From this analysis it is evident that the BATHO and ETAR dose calculations are more deviated from the DOSXYZ dose values for the large field. This could be attributed to the fact that more air

cavities (shown up as bright white with a dark boundary) and bone like structures are irradiated with the larger field. This can be observed with the aid of figure 7.59 to 7.67. Therefore the absorbed dose and the scatter of radiation become too complicated to calculate from a corresponding dose in water for the TPS algorithms. These methods cannot account for the alteration in electronic equilibrium as well as an alteration in the electron scatter characteristics in such complex geometries where air cavities and bone structures are present.

8.5.1.2 Lung model

Figures 7.44 to 7.46 shows the DDVH's for lung radiation with 2x2, 5x5 and 10x10 cm^2 x-ray fields. The BATHO and ETAR algorithms give similar results in all three cases. An interesting feature of this result is that these algorithms become more accurate with respect to the DOSXYZ dose values as the field size is increased. This can be observed for the spectrum value in bin no. 1 that has values of 19, 38 and 50 percent as the field size increases. The values in bin no. 11, that indicate dose deviations larger than 10 percent, decreases from 13 to 4 percent as the field size is increased. The x-ray fields cover an area that contains mainly soft tissue and lung. The lung itself has a lower density than the surrounding soft tissues in the back and front chest wall. The lung can be described as a large inhomogeneity with a network of various smaller soft tissue like inner inhomogeneities. The density difference between these inhomogeneities (boundaries) is not as large as between air, soft tissue and bone as in the head model. The geometry of the inhomogeneities is also simpler and the lung has a more regular shape. As the field size increases relatively fewer of these boundaries are included in the field e.g. the geometry becomes more regular. This can be observed in figures 7.68 to 7.76. In figure 7.68 it is seen that the 2x2 cm^2 x-ray field encloses a volume with inhomogeneities that have a relative large number of interfaces and as the fields are increased as shown in figures 7.71 and 7.74 this number decreases in relation to the field size.

It is known that the BATHO and ETAR methods fail to calculate the dose accurately in and near such interfaces (Orton, 1982). Therefore the less interfaces in a field the more

accurate these algorithms will calculate dose distributions. This phenomenon is reflected in figures 7.44 to 7.47.

8.5.1.3 Prostate model

Figures 7.47 to 7.49 show the DDVH's for the prostate model. The spectral values in bin no. 1 increases from 39 to 59 percent as the field size increases. There is a corresponding decrease in the spectral values in bin no. 11 from 15 to 4 percent. As in the case for the lung model it can be observed that the TPS dose calculation methods have similar dose calculation accuracy for a particular field size. Here it is also evident that for larger fields the BATHO and ETAR methods converge to the DOSXYZ dose calculations. The evaluation of figures 7.77 to 7.85 indicates that there is relatively more inhomogeneity boundaries in the 2x2 cm^2 field than in the 10x10 cm^2 field. In other words the inhomogeneities fill a larger proportion of the 2x2 cm^2 than the 10x10 cm^2 field. And as in the case for the lung this means that the dose is being calculated more accurately for the large field than the smaller fields.

8.5.2 Percentage depth dose curves.

Figures. 7.50 to 7.58 show percentage depth dose (PDD) curves sampled on the central beam axis from the dose distributions in the three patient models. Each graph shows the PDD calculated by the BATHO, ETAR and DOSXYZ methods. The statistical uncertainties in the depth dose are superimposed on the DOSXYZ depth dose curves.

8.5.2.1 Head model

For the head case it is seen that the buildup dose as calculated with the TPS has a large deviation from that calculated by DOSXYZ. The interesting feature here is that for the 2x2 cm^2 field the BATHO method tends to follow the DOSXYZ dose calculations more closely than the ETAR method as seen in figure 7.50. This can be seen in the entrance region of the field when figures 7.59, 7.60 and 7.61 are inspected. At a depth of 6 cm a small air cavity is present. For the 2x2 cm^2 field the BATHO method calculates the dose

in this region more accurately than the ETAR method. This effect is not present for the 5x5 and 10x10 cm^2 fields. Here the BATHO and ETAR methods give inaccurate results as shown in figures 7.51 and 7.52. The dose buildup region is characterized by large deviations in the calculated dose. It is prominent for the ETAR method in figure 7.50, and for the BATHO and ETAR methods in figures 7.51 and 7.52. The ETAR method tends to follow the DOSXYZ dose in a spiky manner, making it more accurate for the 5x5 and 10x10 cm^2 fields. It seems that for small fields the ETAR method does not include the nose part of the head model in the same manner as the Batho method does. This results in the deviation of the dose for the 2x2 cm field. It seems that the ETAR beam model contoured the dose with the surrounding structures of the head. The deviations from the DOSXYZ dose are as high as 70 percent in the buildup region. The beam entry region is in the nose. This is a region characterized by inhomogeneities that disrupts lateral electronic equilibrium. The inability of the ETAR and BATHO methods to model these effects leads to the large dose discrepancies in the nose. Apart from the buildup region (the nose) the spread in the dose is in the order of 5 percent at depths larger than 10 cm (the brain region). The brain region in the head also has the most homogeneous composition. From figure 7.50 it can be observed that the dose maximum is as a depth of 5 cm. This is because of the air cavity in the beam entrance region that causes a dose buildup beyond the cavity where electronic equilibrium can be achieved.

8.5.2.2 Lung model

The PDD curves in lung are shown in figures 7.53 to 7.55. The BATHO and ETAR curves behave similarly for each field size. For the 2x2 cm^2 field it can be seen that the depth dose values for the BATHO and ETAR dose calculation methods deviate on average by about 15 percent from the DOSXYZ depth dose. These effects diminish for the 5x5 and 10x10 cm^2 fields. The DOSXYZ dose also tends to higher values at the exit region of the beam. This can be explained by the lower attenuation of the photons by the lung compared to water. The result is that more photons reach the exit region of the field. This increases the energy fluence and therefore the dose calculated by DOSXYZ is higher than the water based correction algorithms of the TPS. For the larger fields this

effect is even more pronounced although the dose does not overshoot the TPS calculated dose by the same magnitude as in the 2x2 cm^2 field case. The dose in the buildup region is also marginally lower but this difference becomes greater for the larger fields. This can be ascribed to the lack of back scatter photons from the less dense lung regions further downstream of the photon beam. The larger fields enclose more lung tissue and therefore experiences a relatively larger deficit in back scattered photons. The lung inhomogeneity has the greatest effect for the 2x2 cm^2 field due to a lack of side scatter that is present in the 5x5 and 10x10 cm^2 fields. The discrepancy in the surface dose is because of a lack of electrons in the PSF. This beam model contain few electrons as opposed to the real accelerator case that contain enough electrons to raise the surface dose to levels that are much higher and therefore give larger surface dose values.

8.5.2.3 Prostate model

Figures 7.56 to 7.58 shows the PDD curves for the previously mentioned field sizes in a prostate model. For the 2x2 cm^2 field there is a rise in the DOSXYZ dose between depths of 2 to 7 cm in comparison with the BATHO and ETAR depth dose. At a depth of 16 cm the DOSXYZ dose is lower. Inspection of figure 7.77 shows that at a depth between 2 and 7 cm there is a presence of bone structures and at 16 cm depth a dark region is shown. This indicates a region of low density. Thus from the PDD curve the lower DOSXYZ dose is calculated in the lower density region due to a lack of photon interactions. The bone structure is denser than water and therefore enhances photon interactions with a resulting higher dose in this region. For the 5x5 and 10x10 cm^2 fields this effect is almost nonexistent although strong oscillations in the dose larger than the statistical errors are present. The BATHO and ETAR curves are smooth and identical for these field sizes as well as for the 2x2 cm^2 field. The DOSXYZ dose is a few percent lower down stream due to the stronger photon absorption in the bone structure that cannot be modeled effectively with the BATHO and ETAR methods. At greater depths up to the beam exit region this effect diminishes. The increase in side scatter also masks the dose deviation in the less dense portion that is enclosed in the field at 16 cm depth. This side scatter effect is also present in the lung model study.

8.5.3 2D dose distributions

The 2D dose distributions are shown in figures 7.59 to 7.85. The dose distributions are shown separately on each figure for the head, lung and prostate patient models. The DDVH's analysis in section 8.5.2 give the reader an idea of how the BATHO and ETAR methods perform when compared to the DOSXYZ dose calculations. The PDD data analysis shows the effect of inhomogeneities with respect to the photon absorption characteristics of the photon beam. This has a direct effect on the absorbed dose that is modeled more accurately with DOSXYZ. The evaluation of the 2D dose distributions will show how photon beams are shaped in terms of side scatter in regions where the density of the models deviate substantially from the density of water e.g. lung and bone.

8.5.3.1 The effect of inhomogeneities in lateral scatter of beam particles

The comparison of the 10 percent isodose line for the three field sizes in the head shows the BATHO and ETAR methods do not correct for lateral scattering of photons and electrons. This effect is more prominent for the 10x10 cm^2 field size in the lung phantom. Comparison of figures 7.74, 7.75 and 7.76 show that the TPS dose calculation algorithms do not model the lateral scatter process of the photon beam as effectively as DOSXYZ. This can be seen in the behavior of the 10 percent isodose curve through the lung in figure 7.76. The deviation is outward of the beam. This can be ascribed to lateral scatter and for less dense media the absorption of beam particles is less than in more water like models such as the prostate model. This has the effect that the scattered particles impart their energy further away from the beam central axis. The effect of lateral scatter is less prominent for the smaller fields as illustrated in figures 7.70 and 7.73. The BATHO and ETAR methods do not compensate for electron side scatter in their absorbed dose calculations. This can be seen in figures 7.68 and 7.69 and in figures 7.71 and 7.72. In the case of the prostate model the lateral scatter effects are not as prominent due to the more water like nature of the model. Careful examination of the 10 percent isodose curve for the head model shows that in bone regions there is an inward lateral scatter effect present.

This can be seen in figures 7.60 and 7.61 for the bone region just above the maxillary sinus cavities that reach up to the ear cavities. Here the DOSXYZ method models the lateral scatter more accurately than e.g. the ETAR method. The bone region absorbs more particles and inhibits the electrons in terms of their range. These effects are also shown in figures 7.62 to 7.64. The effect is however not large but will be more pronounced in large bone structures. Of the three models used in this study the prostate model is more homogeneous and has a density closer to that of water than lung and bone. Here it can be seen that the lateral scatter effects are virtually non existent when figures 7.77 to 7.85 are compared for each field size.

8.5.3.2 The effect of inhomogeneities on the depth dose of x-ray beams

In section 8.5.3 these effects were discussed and as a supplement to that the reader is referred to figures 7.74 to 7.76. Here the isodose curves are shown for the 10x10 cm^2 field size in the lung model. The 50 percent isodose line covers a larger area for the DOSXYZ dose calculations when compared to the BATHO and ETAR methods. This effect is due to less attenuation in the large lung inhomogeneity. The dose at the exit region of the beam is higher for DOSXYZ than for the BATHO and ETAR calculations. This effect is not modeled effectively by these two dose calculation algorithms. In actual practice then for say an oesophagus treatment with high energy x-rays the TPS would give exit dose distributions that are lower than expected. This could have an impact on the dose to critical organs.

8.5.4 Statistical uncertainty analysis

The BATHO and ETAR methods calculate dose distributions in patient models by using the dose in water as its basis. For a given patient model and beam parameters these algorithms will calculate the dose distribution in water exactly with a 100 percent precision. The water based reference dose distributions (TPS input beam data) were calculated with the DOSXYZ Monte Carlo code. This data are subjected to statistical variation due to the stochastic nature of coupled photon-electron transport processes. The drawback of these Monte Carlo methods is that they converge slowly to small statistical

uncertainties. The number of histories must be quadrupled to reduce these uncertainties by 50 percent. The statistical uncertainties in these water phantom beam data were less than one percent. This could be accomplished by running enough photon histories. These input TPS data are fitted with functions in the TPS thereby filtering out statistical noise. So it is assumed that these data are noise free or at least has noise that are well below one percent. Thus it is not assumed that the TPS calculated dose distributions contain inherent noise due to the entered beam data.

The DOSXYZ calculated dose distributions in the patient models contain statistical noise. The number of histories was determined to reduce the noise to levels in the order of one percent. The statistical error also depended on the actual voxel size of each patient model, which was determined by the CT scanner. These voxel sizes were 10x1.01x1.01 mm^3 for the head model, 10x1.96x1.96 mm^3 for the lung and 10x1.667x1.667 mm^3 for the prostate model. Smaller voxels required more histories because the voxel area as seen from the beam direction determines to a first order the number of interactions that would take place in the voxel. The energy fluence through the voxel would be proportional to its area. The statistical error would also be dependent on the density of the voxel. If the voxel consisted of air the statistical error would be much larger than if it were composed of water or bone. This is because less dense materials have fewer interactions in them, causing a larger statistical error. This can be observed in figure 7.51 in the buildup region of the depth dose in the head model. The statistical error would also depend on the energy fluence profile. Take for example the energy fluence profile in figure 7.4 for a 5x5 cm^2 field. The energy fluence is much lower in the region outside the field boundary. When the PSF is used in actual simulations, this means that the central region has a higher photon density. This means that more photons are transported through the central voxels than those at or just outside the field boundary. Thus the statistical error in the central part of a field in a patient model with a density that is in the order of that of water could be less than one percent but at the field edge it would probably be more. Time and computing speed coupled with the slow convergence of the Monte Carlo method determine to what extent these uncertainties could be reduced.

The following table shows the average percentage error rounded off for each field and patient model. This was determined only for dose values not less than 20 percent as not to include those dose voxels that lay too far outside the field boundary.

Patient model	**Field size** (cm^2)	**uncertainty (percent)**
Head	2x2	1.5
	5x5	1
	10x10	2
Lung	2x2	1
	5x5	1
	10x10	2
Prostate	2x2	1
	5x5	1
	10x10	1.5

Table 8.1. The average statistical uncertainty expressed as a percentage for the DOSXYZ generated dose distributions. Data shown are for the different patient models and field sizes.

These uncertainties are considered small enough to be able to reach meaningful conclusions about the results reported in this study. The dose differences observed are not associated with statistical uncertainties of a magnitude that would place a large uncertainty on the interpretation of the results.

The DDVH's that show the comparison of the BATHO and ETAR dose calculation methods with the DOSXYZ method can be interpreted with the aid of table 8.1. The percentage of the volume receiving a dose that differs from the DOSXYZ dose by more than 5 + x percent, where x is given in the error column of table 8.1, could then be determined. This would be clinically significant on at least the 5 percent level. Due to other dose administering uncertainties a limit of 3 percent is preferred that is taken to be 3 + x percent when the statistical uncertainties in table 8.1 are taken into consideration.

Table 8.2 shows the percentage of the irradiated volume that differs in dose by more than a prescribed level after the error in the DOSXYZ data are taken into account for a worst case scenario.

		Percentage of volume not meeting uncertainty criterion of 1, 3 or 5 percent					
		Batho			**ETAR**		
Patient model	**field size**	**1**	**3**	**5**	**1**	**3**	**5**
	(cm^2)						
Head	2x2	38	26	18	44	31	24
	5x5	38	23	15	40	25	16
	10x10	48	26	15	48	27	16
Lung	2x2	44	32	24	44	32	23
	5x5	32	19	12	33	19	14
	10x10	20	11	6	22	13	7
Prostate	2x2	11	10	7	11	10	7
	5x5	10	10	8	10	10	8
	10x10	15	10	6	15	9	6

Table 8.2. The percentage of the irradiated volume where the uncertainty in dose would be more than 1,3 and 5 percent for the BATHO and the ETAR methods.

The data in table 8.2 were compensated for the average percentage statistical error in the DOSXYZ dose as shown in table 8.1 The analysis was performed by adding this statistical uncertainty to the desired error criterion in table 8.2. The data shown here is the minimum percentage of the volume that would not meet the error criterion.

From these data it is evident that Monte Carlo dose calculations will play an important role in the reduction of dose administration uncertainties, in which the dose calculation method contributes in addition to various patient set up and radiation errors. This would favor the one percent accuracy in the dose calculation more in order to reduce the total error to less than 5 percent in the administration of the radiation dose to the patient. From

table 8.2 it is clear that Monte Carlo methods could play a role in all types of treatment planning from complex head to simpler prostate radiation treatment since both the BATHO and ETAR methods are unable to give results that could match the performance of the DOSXYZ method.

8.5.5 Combination of two perpendicular wedged beams

In figure 7.86 a DDVH was calculated for the dose differences between the BATHO and ETAR dose calculation algorithms as benched against the DOSXYZ calculated dose distribution. When this result is compared with the result for a single open beam in figure 7.42 it can be observed that the percentage of the irradiated volume that have dose differences larger than 10 percent (bin no.11) is 26 percent compared to 12 to 16 percent for the BATHO and ETAR methods. This indicates that the combination of wedged beams resulted in a less accurate dose calculation by the TPS. A depth dose profile through this dose distribution is shown in figure 7.86. The central axis is the same as that in figure 7.51. The statistical error is below one percent for the DOSXYZ dose calculations. It can be seen that the doses differ in the order of 10 percent, reflecting the result in the DDVH of figure 7.86. A comparison of the 2D dose distributions in figures 7.88 to 7.90 indicates that the DOSXYZ dose distributions are more sensitive to sudden anatomical changes such as the nasal cavities and the irregular nose buildup plane. If the accuracy in a TPS must be better than 3 percent then the Monte Carlo method of dose calculation is the method of choice. Both the BATHO and ETAR methods are not suitable for dose calculations when this accuracy level is desired.

CHAPTER 9

CONCLUSION

The aim of this study was to develop a Monte Carlo simulation method for the evaluation of dose distribution calculations of radiotherapy treatment planning systems. In this study the CADPLAN TPS, which uses the BATHO and ETAR inhomogeneity correction algorithms, was evaluated. From the discussion in Chapter 8 the following can be concluded:

1) The DOSXYZ code, in combination with the BEAM code, can provide the necessary beam data and dose distributions for the evaluation of the TPS. Although the study evaluated the BATHO and ETAR methods in older correction based algorithms, the DOSXYZ dose calculations can be used to evaluate any sophisticated dose calculation algorithm such as convolution and inverse treatment planning algorithms. The method presented in this study would remain essentially the same as far as the Monte Carlo dose simulations are concerned. It is essentially independent of the TPS's absorbed dose calculations and will work for any TPS that uses CT based patient models. The normalization procedure that scales the DOSXYZ generated absorbed dose distributions could differ from that of other TPS algorithms. The method employed here relies on the reproducibility of the TPS with regard to its calculation of the normalized absorbed dose in a water phantom. The methods employed in this study could in principle lead to the development of a data base of benchmark dose distributions as well as input beam data for any TPS, if the required format of input beam data were specified by the TPS manufacturers. This could be a valuable tool for TPS manufacturers to demonstrate the accuracy of their dose calculation algorithms.

2) The transformation of CT based patient data into data containing materials that are directly associated with cross sections leads to realistic patient models. This allows a realistic evaluation of the TPS's dose calculation algorithms.

3) The DOSXYZ generated dose distributions in three common treatment sites cover the main treatment planning geometries ranging from a complex maxillary sinus (head) model to more water-like models such as the prostate model. The lung model provides the TPS with large inhomogeneities that allow the realistic study of the absorbed dose calculations.

4) The DOSXYZ dose distributions showed that for large inhomogeneities and small fields such as the lung model for the 2x2 cm^2 field the absorbed dose could differ by up to 15 percent. In the head model this difference can be as large as 70 percent in the build-up region. Lateral scatter effects are also responsible for the deviation of isodose curves especially in the lung model for the 10x10 cm^2 field. The BATHO and ETAR methods have essentially the same performance with marked differences in the head model in the build-up region. From table 8.2 it is evident that use of these dose calculation algorithms can lead to significant dose differences in from 7 to 48 percent of the volume that is irradiated.

5) The inability of the BATHO and ETAR methods to account for lateral and longitudinal electron transport is also demonstrated in these patient models. These effects are well known but were usually studied in more regular phantoms. This study showed the true effect of these inhomogeneity corrections in realistic patient models.

6) The results obtained in this study indicate that these commonly used algorithms can lead to large uncertainties in special cases such as lung irradiation with small fields. For soft tissue such as found in the treatment of prostate and cervix cancers, they could be adequate. Better tumor control through more accurate planning could be obtained if the Monte Carlo method could be applied on a regular basis for treatment planning. This is not possible yet due to computational hardware restraints, but research in this regard is actively being pursued by several workers.

Abstract

In this study a method is described whereby the dose distributions calculated by any treatment planning system (TPS) could be evaluated using dose distributions calculated with Monte Carlo simulations. The Monte Carlo dose simulations can be regarded as the golden standard. The method developed in this study involved the Monte Carlo simulation of a Philips SL75/14 based generic accelerator with the BEAM code. This was done to obtain beam information stored in phase space files that were characteristic of the generic accelerator. This beam data were then used for the simulation of dose distributions in a mathematical water phantom using the Monte Carlo code, DOSXYZ. The same beam data were used to generate the data base for the TPS that uses it for dose calculations in CT based patient models. The BATHO and ETAR inhomogeneity correction algorithms implemented on a CADPLAN TPS were evaluated.

The CT slices that make up the patient model, on the TPS, were transformed to material data. Each of these materials (57 in total) covered a discrete CT interval in a total CT number range of 3000 CT numbers. Each of the 57 materials was represented in the preprocessor code (PEGS4) to allow dose simulations in realistic patient models with the DOSXYZ code. Dose distributions were calculated in a maxillary sinus (head), lung and prostate patient for photon beams with size 2x2, 5x5 and 10x10 cm^2. These dose distributions were calculated on the TPS using the BATHO and ETAR methods. The DOSXYZ dose distributions were scaled to the TPS calculated dose distributions by normalization to the dose in water at 2 cm depth on the beam central axis.

Dose difference volume histograms, percentage depth dose curves and 2D dose distributions were obtained to evaluate these dose distributions. The BATHO and ETAR methods cannot model lateral and longitudinal electron transport through complex media. These effects were apparent in large inhomogeneities such as in the lung model where the Monte Carlo dose simulation gave a wider beam penumbra for the large field, and in the deviation of the TPS dose distributions in these regions for the small field size.

The method developed in this study could also be applied to any TPS that uses more sophisticated models. Manufacturers of TPS's in particular could use the methods described in this study to evaluate their dose calculation algorithms.

Key words: Monte Carlo, CT based patient model, DOSXYZ, BEAM, Treatment planning, dose distributions, lung, maxillary sinus, water phantom, lateral electron transport, TPS, inhomogeneity.

simulasies het 'n wyer penumbra vir die 10x10 cm^2 bundel grootte aangedui, asook die afwyking van die BPR-berekende dosis vir klein velde.

Die metode wat in hierdie studie ontwikkel is kan ook gebruik word vir die evaluering van enige BPR wat meer gesofistikeerde dosisberekeningsalgoritmes gebruik. Vervaardigers van BPR's kan hierdie metode gebruik om hulle dosisberekeningsalgoritmes mee te evalueer.

Sleutelwoorde: Monte Carlo, RT pasiënt modelle, DOSXYZ, BEAM, behandelingsbeplanning, dosisdistribusies, long, maxillêre sinus, waterfantoom, laterale elektron transport, beplanningstelsel, nie-homogeniteit.

References

Ahnesjö, A., Andreo, P. and Brahme, A.' Calculation and application of point spread functions for treatment planning with high-energy photon beams.', Acta Oncologica (26), 1987, pp 49 - 51

Attix, F.H. Introduction to Radiological Physics and Radiation Dosimetry, John Wiley, New York (1986)

Attix, F.H., Owolabi, S. and Paliwal, B.R., ' Electron contamination in ^{60}Co gamma-ray beams.', Med. Phys. 10(3), 1983, pp 301 - 306

Ballester, F., Hernández, C. and Pérez-Calatayud, J. et al., ' Monte Carlo calculation of dose rate distributions around ^{192}Ir wires.', Med. Phys. 24(8), 1997, pp 1221 - 1228

Bedford, J.L., Oldham, M., Hoess, A., Evans, P.M., Shentall, G.S. and Webb, S. ' Methods for transferring patient and plan data between radiotherapy treatment planning systems.', B J Rad (70), 1997, pp 740 - 746

Berger, M.J. and Spencer, L.V. ' Some Radiological Applications of Gamma-Ray Transport Theory.', Radiation Research (10), 1959, pp 552 - 570

Bielajew, A.F. and Rogers, D.W.O. ' PRESTA- The parameter reduced electron-step algorithm for electron Monte Carlo.', PIRS No. 042 (National Research Council of Canada, Ottawa 1986),

Bielajew, A.F., Rogers, D.W.O. and Nahum, A.E., ' The Monte Carlo simulation of ion chamber response to ^{60}Co-resolution of anomalies associated with interfaces.', Phys. Med. Biol. 30(5), 1985, 419 - 427

Bjärngard, B.E. and Shackford, H. ' Attenuation in high-energy x-ray beams.', Med. Phys. 21(7), 1994, pp 195 - 200

Boyer, A., Xing, L. and Ma, C-M et al. ' Theoretical considerations of monitor unit calculations for intensity modulated beam treatment planning.', Med. Phys. 26(2), 1999, pp 187 - 195

Brahme, A.' Dosimetric precision requirements in radiation therapy.', Acta Radiologica Oncology (23), 1984, pp 379 - 391

Brahme, A, Ågren, A.-K.' Optimal dose distribution for eradication of heterogeneous tumours.', Acta Oncologica (26), 1987, pp 377 - 385

CADPLAN REFERENCE MANUAL:, Chapter 3, Calculation models. Version 2.6 1995

CADPLAN Treatment Modeling Workstation Reference Manual 1995

Chan, H. and Doi, K., ' Physical characteristics of scattered radiation in diagnostic radiology: Monte Carlo simulation studies.', Med. Phys. 12(2), 1985, pp 152 - 165

Chaney, E.L., Cullip, T.J. and Babriel, T.A.,' A Monte Carlo study of accelerator head scatter.', Med. Phys. 21(9), 1994, pp 1383 - 1390

Cheung, Y.C., Yu, P.K.N. and Young, E.M.C. et al., ' The dose distribution to an ^{192}Ir wire source: EGS4 Monte Carlo calculations.', Phys. Med. Biol. (42), 1997, 401 - 406

Convery, D.J. and Rosenbloom, M.E. ' Treatment delivery accuracy in intensity-modulated conformal radiotherapy.', Phys. Med. Biol. (40), 1995, pp 979 - 999

Cunningham, J.R.' Scatter-Air Ratios.' Phys.Med.Biol. 1972(17), pp 42 - 51

Dahlin, H., Lamm, I.-L., Landberg, T., Levernes, S. and Ulsø, N.' User requirements on CT-based computed dose planning systems in radiation therapy.', Acta Oncologica, 1983, pp 398 - 415

DeMarco, J.J., Solberg, T.D. and Smathers, J.B. ' A CT-based Monte Carlo simulation tool for dosimetry planning and analysis.', Med. Phys. 25(1), 1998, pp 1 - 11

DeMarco, J.J., Solberg, T.D., Wallace, R.E., and Smathers, J.B. ' A verification of the Monte Carlo code MCNP for thick target brehmstrahlung calculations.', Med. Phys. 22(1), 1995, pp 11 - 30

Ding, X., Rogers, D.W.O. and Mackie, T.R. ' Calculation of stopping-power ratios using realistic clinical electron beams.', Med. Phys. 22(5), 1995, pp 489 - 502

Du Plessis, F.C.P., Willemse, C.A., Lötter, M.G. and Goedhals, L. ' The indirect use of CT numbers to establish material properties needed for Monte Carlo calculation of dose distributions in patients.', Med. Phys. (25), 1998, pp 1195 - 1201

Ebert, M.A. and Hoban, P.W., ' A Monte Carlo investigation of electron-beam applicator scatter.', Med. Phys. 22(9), 1995, pp 1431 - 1435

El-Khatib, E. and Battista, J.J.,' Improved lung dose calculation using tissue-maximum ratios in the Batho correction.', Med.Phys. (11), 1984, pp 279 - 286

Goitein, M.,' Calculation of the uncertainty in the dose delivered during radiation therapy.',. Med.Phys. (12), 1985, pp 580 - 586

Hannalah, D., Zhu, T.C. and Bjärngard, E.B.,' Electron disequilibrium in high-energy x-ray beams.', Med.Phys. (23), 1996, pp 1867 - 1871

Haider, J.A.,'A general cavity theory.', Phys. Med. Biol. (42), 1997, pp 491 - 500

Halbleib, J.A. and Melhorn, T.A.,' ITS: The Integrated TIGER Series of Coupled Electron/Photon Monte Carlo Transport Codes.', Sandia Report SAN84-0073, Sandia National Laboratories, Albuquerque, New Mexico.

Hartmann-Siantar, C.L., Chandler, W.P., Rathkopf, J.A., Svatos, M.M. and White, R.M. ' PEREGRINE: An All-particle Monte Carlo code for radiation therapy.', Proceedings of the International Conference on Mathematics and Computations, Reactor physics, and Environmental Analysis, (American Nuclear society, LaGrange Park, 1995), pp 857 - 865

Higgins, P.D., Sibata, C.H. and Paliwal, B.R. ' Determination of contamination-free build-up for ^{60}Co.', Phys. Med. Biol. 30(2), 1985, pp 153 - 162

Holmes, T. and Mackie, T.R. ' A comparison of three inverse treatment planning algorithms.',. Phys. Med. Biol. 39, 1994, pp 91 - 106

Horowitz, Y.S. et al.,' Modified general cavity theory applied to the calculation of gamma dose in ^{60}Co thermoluminescence dosimetry.', Phys. Med. Biol. (28), 1983, pp 829 - 840

Hubbell, J.H. ' Photon Mass Attenuation and Energy-absorption Coefficients from 1 keV to 20 MeV.', Int. J. Appl. Radiat. Isot. (33), 1982, pp 1269 - 1290

Hubbell, J.H., Gimm, H.A. and Øverbø, I. ' Pair, Triplet, and Total Atomic Cross Sections (and Mass Attenuation Coefficients) for 1 MeV-100GeV Photons in Elements Z = 1 to 100.', J. Phys. Chem. Ref. Data, Vol. 9, No. 4, 1980, pp 1023 - 1149

Hubbell, J.H. and Seltzer, S.M. ' Table of X-ray Mass Attenuation Coefficients and Mass Energy-Absorption coefficients 1 keV to 20 MeV for elements Z = 1 to 92 and 48

Additional Substances of Dosimetric Interest.', NISTIR 5632, U.S. Dept. of Commerce, 1995

ICRU, International Commission On Radiation Units and Measurements. Report No. 44, Bethesda, MD. CRU, 1989

Jette, D and Walker, S. ' Electron dose calculation using multiple-scattering theory: Energy distribution due to multiple scattering', Med. Phys. 24(3), 1997, pp 383 - 400

Johns, H.E and Cunningham, J.R. The physics of radiology, Charles C Thomas, Springfield, Illinois, 1983

Kaell, P. and Hoban, P.' Accounting for primary electron scatter in x-ray beam convolution calculations.', Med. Phys. 22(1995), pp 1413 - 1418

Kawrakow, I., Fippel, M. and Friedrich, K. ' 3D electron dose calculation using a Voxel based Monte Carlo algorithm (VMC).', Med. Phys. 23(4), 1996, pp 445 - 457

Kearsley, E. ' A new general cavity theory.', Phys. Med. Biol. (29), 1994, pp 1179 - 1187

Kirkby, D.R. and Delpy, D.T. ' Parallel operation of Monte Carlo simulations on a diverse network of computers.', Phys. Med. Biol. (42), 1997, pp 1203 - 1208

Knoös, T., Ahnesjö, A., Nilsson, P and Weber, L.' Limitations of a pencilbeam approach to photon dose calculations in lung tissue.', Phys.Med.Biol. (40), 1995, pp 1411 - 1420

Krane, S.K. Introductory Nuclear Physics, John Wiley and sons, New York 1988

Larson, K.B. and Prasad, S.C.' Absorbed dose computations for inhomogeneous media in radiation treatment planning using differential scatter-air ratios.' Proceedings of the

Second Annual Symposium on Computer Applications in Medical Care, Washington, D.C., U.S.A., 5 - 9 November 1978, pp. 93 - 99, IEEE, New York, 1978

Lewis, R.D., Ryde, S.J.S., Hancock, D.A. and Evans, C.J. ' An MCNP-based model of a linear accelerator x-ray beam.', Phys. Med. Biol. (44), 1999, pp 1219 - 1230

Li, X.A. and Rogers, D.W.O. ' Electron mass scattering powers: Monte Carlo and analytical calculations.', Med. Phys. 22(5), 1995, pp 531 - 541

Liu, S, Lind, K.B. and Brahme, A. ' Two accurate algorithms for calculating the energy fluence profile in inverse radiation therapy planning.', Phys. Med. Biol. 38, 1993, pp 1809 - 1824

Liu, Y., Yin, F. and Gao, Q. ' Variation method for inverse treatment planning.', Med. Phys. 26(3), 1999, pp 356 - 363

Lovelock, D.M.J., Chui, C.S. and Mohan, R. ' A Monte Carlo model of photon beams used in radiation therapy.', Med. Phys. 22(9), 1995, pp 1387 - 1394

Low, D.A. and Hogstrom, K.R. ' Determination of the relative linear collision stopping power and linear scattering power of electron bolus material.', Phys. Med. Biol. 39, 1994, pp 1063 - 1068

Ma, C.-M., Reckwerdt, P., Holmes, M., Rogers, D.W.O., and Geiser, B.' DOSXYZ Users Manual', National Research Council of Canada (NRC, Ottawa), 1995

Ma, C.-M. and Rogers, D.W.O. 'BEAMDP Users Manual', National Research Council of Canada Report PIRS-0509B (NRC, Ottawa), 1995

Mackie, T.R., Bielajew, A.F., Rogers, D.W.O. and Battista, J.J.' Generation of photon energy deposition kernels using the EGS Monte Carlo code.', Phys. Med. Biol 33(1988), pp 1 - 20

Mackie, T.R., El-Khatib, E., Batista, J. and Scrimger, J.' Lung dose corrections for 6- and 15 MV x-rays.', Med.Phys. (4), 1985, pp 327 - 332

Mah, K. and Van Dyk, J.' On the impact of tissue inhomogeneity corrections in clinical thoraic radiation therapy.' Int. J. Rad. Oncology Biol. Phys. (21), 1991, pp 1257 - 1276

Manfredotti, C., Nastasi, U. Marchisio, R. Ongaro, C. and Gervino, G. ' Monte Carlo simulation of dose distribution in electron beam radiotherapy treatment planning.', Nucl. Instr. Meths. (A291), 1990, pp 646 – 654

Maughan, R.L., Chuba, P., Porter, A.T. and Ben-Josef, E. ' Mass energy-absorption coefficients and mass collision stopping powers for electrons in tumours of various histologies.', Med. Phys. 26(3), 1999, pp 1 - 20

Miljanic, S. Et al., ' Application of cavity theory to the response of various TLD's to C0-60 gammas degraded in water.', Phys. Med. Biol. (42), 1997, pp 1335 - 1349

Mobit, P.N., Nahum, A.E and Mayles, P., ' An EGS4 Monte Carlo examination of general cavity theory.', Phys. Med. Biol. (42), 1997, pp 1319 - 1334

Mohan, R. and Chui, C., ' Energy and angular distributions of photons from medical linear accelerators.', Med. Phys. 12(5), 1985, pp 592 - 597

Nelson, W.R., Hirayama, H. and Rogers, D.W.O., The EGS4 Code System SLAC-Report-265, Stanford Linear Accelerator Center (1985)

Nelson, W.R. Jenkins, M. and Rindi, A. ' Monte Carlo Transport of Electrons and Photons.', Plenum press, New York, 1988

Neuenschwander, H. Mackie, T.R. and Reckwerdt, P.J.' MMC- a high-performance Monte Carlo code for electron beam planning.', Phys.Med.Biol. (40), 1995, pp 543 - 574

Nizin, P.S. 'Electronic equilibrium and primary dose in collimated photon beams.', Med. Phys. 20(6), 1993, pp 1721 - 1729

Ogunleye, O.T., ' A comparison of the Burlin and Kearsley general cavity theories with LiF TLD measurements for 10 MV x-rays.', Phys. Med. Biol. (32), 1987, 901 - 904

Ogunleye, O.T. et al, 'Comparison of Burlin cavity theory with LiF TLD measurements for cobalt-60 gamma rays.', Phys. Med. Biol. (25), 1980, pp 203 - 213

Orton, C.: Progress in Medical Radiation Physics, chapter 2 'Tissue Inhomogeneity Corrections in Photon-Beam Treatment Planning', Plenum press. New York.1982, p 103 – 130

Ostiapak, O.Z., Zhu, Y. and Van Dyk, J.' Refinements of the finite-size pencil beam model of three-dimensional photon dose calculation.', Med. Phys. 24(1997), pp 743 - 750

Papiez, L., McLellan, J. Sandison, G.A. et al. ' Inclusion of energy straggling in a numerical method for electron dose calculation.', Med. Phys. 21(10), 1994, pp 1591 - 1598

Perry, D., Wollin, M., and Olch, A. ' Range spectra in electron penetration problems.', Med. Phys 25(1), 1998, pp 43 – 55

Pérez-Calatayud, J., Lliso, F. and Carmona, V. ' Monte Carlo calculation of dose rate distributions around 0.5 and 0.6 mm in diameter ^{192}Ir wires.', Med. Phys. 26(3), 1999, pp 395 - 401

Persliden, J. ' A Monte Carlo program for photon transport using analogue sampling of scattering angle in coherent and incoherent scattering processes.', Computer Programs in Biomedicine. (17), 1983, pp 115 - 128

Pla, C., Podgorsak, E.B. and El-Khatib, E. ' Calculation of dose in homogeneous phantoms for irregular, partially attenuated, photon beams.', Med.Phys. 15(1988), pp 511 - 516

Raeside, D.E. ' Monte Carlo principles and Applications.', Phys. Med. Biol, 21(2), 1976, pp 181 - 197

Rogers, D.W.O. and Bielajew, A.F. ' Calculated buildup curves for photons with energies up to ^{60}Co.', Med. Phys. 12(6), 1985, pp 738 - 744

Rogers, D.W.O., Faddegon, B.A., Ding, G.X., Ma, C.-M. and We, et al.' BEAM: A Monte Carlo code to simulate radiotherapy treatment units. Med.Phys. 22(5): 1995, pp 503 - 524

Rogers, D.W.O., Bielajew, A.F. and Nahum, A.E.' Ion chamber response and A_{wall} correction factors in a ^{60}Co beam by Monte Carlo simulation.', Phys. Med. Biol. 30(5), 1985, pp 429 - 443

Sandborg, M., Dance, D.R., Persliden, J., and Carlsson, G.A. ' A Monte Carlo program for the calculation of contrast, noise and absorbed dose in diagnostic radiology.', Computer methods and programs in biomedicine. (42), 1994, pp 167 - 180

Sauer, O.A.' Calculation of dose distributions in the vicinity of high-Z interfaces for photon beams.', Med.Phys. (22), 1995 , pp 1685 - 1693

Seltzer, S.M., ' Calculation of Photon Mass Energy-Transfer and Mass Energy-Absorption Coefficients.', Radiation Research. (136), 1993, 1959 - 1968 pp 147 - 170

Seuntjens, J. Van der Plaetsen, A. and Thierens, H.' Comparison of measured and calculated dose distributions in lung after electron beam treatment of the chest wall.', Med.Phys. (21), 1994, pp 1959 - 1968

Sharpe, M.B. and Battista, J.J.' Dose calculations using convolution and superposition principles: The orientation of dose spread kernels in divergent x-ray beams.', Med. Phys. (20), 1993, pp 1685 - 1694

Sherouse, G.W. ' A mathematical basis for wedge angle and orientation.', Med.Phys. (20), 1993, pp 1211 - 1218

Siddon, R.L. ' Calculation of the radiological depth.', Med.Phys. (12), 1985, pp 84 – 87

Simpkin, D.J. and Mackie, T.R. ' EGS4 Monte Carlo determination of the beta dose kernel in water.', Med. Phys. 17(2), 1990, pp 179 - 186

Sixel, K.E. and Faddegon, B.A., ' Calculation of x-ray spectra for radiosurgical beams.', Med. Phys. 22(10), 1995, pp 1657 - 1661

Sontag, M.R., Battista, J.J., Bronskill, M.J. and Cunningham, J.R.' Implications of computed tomography for inhomogeneity corrections in photon beam dose calculations.', Radiology 124, 1977, pp 143 - 149

Sontag, R.M. and Cunningham, J.R.' Corrections to absorbed dose calculations for tissue inhomogeneities.', Med.Phys. (4), 1977, pp 431 - 436

Sontag, M.R. and Cunningham, J.R. ' The equivalent tissue-air ratio method for making absorbed dose calculations in a heterogeneous medium.', Radiology 129(1978), pp 787 - 794

Storchi, P. and Woudstra, E. ' Calculation models for determining the absorbed dose in water phantoms in off-axis planes of rectangular fields of open and wedged photon beams.', Phys. Med. Biol. 40, 1995, pp 511 - 527

Thames, H.D. ' First scatter to off-axis points and the Clarkson method.', Phys.Med.Biol. (18), 1973, pp 444 - 451

Udale-Smith, M., ' Monte Carlo calculations of electron beam parameters for three Philips linear accelerators.', Phys. Med. Biol. 37(1), 1992, pp 85 - 105

Upton, A.C. ' Cancer induction and non-stochastic effects.', Proceedings of a one-day seminar held at the BIR 44th annual Congress, Bristol, April 11, 1986. B J Rad. (60), 1987

Valicenti, R.K., Kirov, A.S., and Meigooni, A.S., et al., ' Experimental validation of Monte Carlo dose calculations about a high intensity Ir-192 source for pulsed dose-rate brachytherapy.' Med. Phys. 22(6), 1995, pp 821 - 829

Van't Riet, A., Stam, H.C., Mak, A.C.A. and van Slooten, F.H.S. ' Implications of lung corrections for dose specification in radiotherapy.', Int.J.Radiation Oncology Biol. Phys. 11(1985), pp 621 - 625

Wallace, S.A., Allen, B.J. and Mathur, J.N. ' Monte Carlo calculations of epithermal boron neutron capture with heavy water.', Phys. Med. Biol. (40), 1995, pp 1599 - 1608

Wang, R. and Sloboda, R.S. ' EGS4 dosimetry calculations for cylindrical symmetric brachytherapy sources.', Med. Phys. 23(8), 1996, pp 1459 – 1465

Webb, S. ' A Monte Carlo Study of the Interaction of External Beam X-radiation with Inhomogeneous Media', Phys. Med. Biol. 23(6), 1978, pp 1043 - 1059

Werner, L.B. ' Choosing $FUDGEMS in EGS4 Monte Carlo.' Phys. Med. Biol. (42), 1997, pp 735 - 743

Williamson, J.F. and Li, Z., ' Monte Carlo aided dosimetry of the microselectron pulsed and high dose-rate ^{192}Ir sources.', Med. Phys. 22(6), 1995, pp 809 - 819

Wong, E., Zhu, Y. and Van Dyk, J. ' Theoretical developments on fast Fourier transform convolution dose calculations in inhomogeneous media.', Med. Phys. (23), 1996, pp 1511 - 1521

Yarnold, J. ' Molecular aspects of cellular responses to radiotherapy.', Radiotherapy & Oncology. (44), 1997, pp 1 - 7

Young, M.E.J. and Gaylord, J.D. ' Experimental tests of corrections for tissue inhomogeneities in radiotherapy.', Br.J.Radiol., 43(1970), pp 349 – 355

Yu, M.K, Murray, B and Sloboda, R. ' Parametrization of head-scatter factors for rectangular photon fields using an equivalent square formalism', Med. Phys 22(8), 1995, pp 1329 - 1332

Acknowledgements

The author would like to thank the following people:

My promotor Dr. C.A. Willemse for all the time he devoted in numerous discussions and solutions to make the realization of this work possible.

My co-promotor Prof. Dr. M.G. Lötter for his valuable suggestions and his funding of the computer hardware and other essential elements to keep it all going.

To the chief of the radiation oncology department Prof. L. Goedhals for giving his approval for using the apparatus in the department.

My wife for her understanding and support.

Everyone else that made that essential contribution, big or small, for making this possible.